DEVELOPMENT OF POINT-OF-CARE DEVICES FOR RAPID DIAGNOSTICS AND PREVENTIVE CARE

A Dissertation

Presented to the Faculty of the Graduate School

of Cornell University

in Partial Fulfillment of the Requirements for the Degree of

Doctor in Philosophy

by

Vlad-Victor Oncescu

January 2014

DEVELOPMENT OF POINT-OF-CARE DEVICES FOR RAPID DIAGNOSTICS AND PREVENTIVE CARE

Vlad-Victor Oncescu, Ph.D.

Cornell University 2014

With the cost of healthcare in the U.S. predicted to reach 30% of the GDP by 2040, medical technology needs to help reduce the stress on physicians and facilitate personalized preventive care. The two most promising ways of achieving this are through developments in implantable devices for monitoring and treating patients outside of clinical settings and through better point-of-care diagnostics tools.

The first part of this dissertation focuses on the development of a potentially implantable autonomous device for the prevention of late-phase hemorrhagic shock (HS), the leading cause of death for people with traumatic injuries. We demonstrate that such a device can continuously monitor vasopressin levels, an indicator of late-phase HS, and release vasopressin automatically when levels drop below a certain threshold in order to help stabilize the situation. We also discuss the possibility of using a non-enzymatic glucose fuel cell unit, instead of a lithium battery, in order to increase the implantable device's lifetime. Novel power sources are important in the development of low-power long-term implantable devices, and we propose several non-enzymatic fuel cells that can be used as coating layers on current implantable devices or as stand-alone power sources. We show that such glucose fuel cell can produce 16μW cm^{-3} of power

and can be integrated in implantable devices such as the one for preventing late-phase HS.

In the second part of the dissertation, we discuss the development of a platform for colorimetric biomarker detection on a smartphone. This platform consists of a smartphone accessory that allows uniform and repeatable image acquisition of a colorimetric test strip and an app that analyzes parameters such as hue, saturation and luminosity of the test area, quantifies the biomarker levels and displays the value on the screen. We demonstrate its use in monitoring electrolyte loss, enamel decalcification, cholesterol and vitamin D. We envision this as the first step toward the development of the NutriPhone, a platform for vitamin and micronutrient testing on a smartphone.

BIOGRAPHICAL SKETCH

Vlad-Victor Oncescu was born in Craiova, Romania and grew up in Montreal where he graduated from McGill University in May 2009 with a Bachelor of Engineering degree. He completed the Honors program in Mechanical Engineering with emphasis on aerospace and fluid dynamics and his honors thesis, under the supervision of Professor Evgeny Timofeev, was focused on the numerical analysis of Busseman inlets in supersonic flow. During his final year of studies, he worked at the Canadian Space Agency developing numerical simulation for the study of wrinkle formation in membranes structures with possible application in artificial satellites.

His interest in nanotechnology brought him to Cornell University where he worked in Professor David Erickson's Lab, first on the development of biofuel cells and after on smartphone diagnostics. While at Cornell he also pursued many diverse interests such as the study of the Chinese language, computer science and finance.

To my parents for their love and support

ACKNOWLEDGMENTS

I would like to thank my advisor David Erickson for allowing me to pursue my interests in and out of the lab. I have learned much more from my time at Cornell than what is included in this dissertation and this is largely due to him.

I would like to acknowledge the people who have collaborated on the work presented here, namely Seoho Lee, Dakota O'Dell, Matthew Mancuso and Peng He. I would also like to thank former labmates Bernardo Cordovez, Aram Chung and Mekala Krishnan for being great role models. During my years at Cornell I have met numerous people who have inspired me and supported me and I would like to acknowledge Li Jiang, Natasha Udpa, Frank He, Hera Li and Yin He above all.

Finally, I would first like to acknowledge the financial support that I received during my graduate studies through scholarships from the Canadian funding agencies: FQRNT and NSERC.

TABLE OF CONTENTS

LIST OF FIGURES

Chapter 1

Opportunities in point of care diagnostics[1]

This thesis focuses on the development of two alternative technologies for point of care diagnostics and preventive care. With health care cost in the U.S. projected to reach 30% of GDP by 2040, it is clear that technology needs to play a major role in the future. In this section we will discuss briefly some of the ways through which the reliance on physicians and hospital care can be reduced as well as analyze some of the areas where medical technology can play a major role in the near future.

---

[1]Section 1.2 of this chapter was published as Chen,Y.-F., Jiang, L.[*], Mancuso, M.[*], Jain, A.[*], **Oncescu, V**[*], Erickson, D. "Optofluidic Opportunities in Global Heath, Food, Water and Energy" *Nanoscale* 4, 4839-4857 (2012)
[*] These authors have contributed equally to this paper

1.1 Autonomous Implantable Devices for Preventive Care

Over the past decade, implantable autonomous microsystems have been developed to counter life-threatening medical conditions and to improve patient care by replacing cumbersome treatment procedures. (Receveur et al., 2007)As such, a growing number of patients now depend on implantable cardioverter defibrillators (Adler et al., 2013), gastric stimulators (Arriagada et al., 2011), cardiac pacemakers (Liu et al., 2013) and artificial organs (Cebotari et al., 2010; Krabatsch et al., 2011; Ricotti et al., 2012) for survival. In such cases, the severity and urgency of the medical condition override the high cost and risk of the invasive surgery that is required. On the other hand, some situations call naturally for implantable medical devices to continuously monitor physiological changes in patients or to deliver treatment through pre-determined and repeated drug delivery. For instance, continuous glucose monitoring devices have found their market by increasing the efficacy of diabetes treatment and by helping patients monitor real-time variations in their blood glucose levels due to insulin and food intake, exercise, and other factors. Recently, Farra *et al.* demonstrated an implantable drug delivery microchip that operates for up to 3 weeks and eliminates the need for daily physician-assisted injections for patients with osteoporosis (Farra et al., 2012). While these developments have been successful at independently performing sensing (Fojtik et al., 2013) and drug delivery (Chung et al., 2009), developing

implantable medical devices capable of achieving both of those functions simultaneously would be suitable for a number of applications (Esquivel et al., 2012). One such case is the detection and treatment of traumatic injuries such as hemorrhagic shock (HS).

In Chapter 2 we discuss in detail the development of a autonomous device for application in late-phase HS prevention that consists of a nanowire biosensor for detecting changes in vasopressin levels, an on-board electrochemically driven drug delivery system for administration of vasopressin, and a non-enzymatic glucose fuel cell for powering the system.

1.1.1 Glucose Fuel Cells for Implantable Devices

For over three decades, low-power implantable devices have been powered using non-rechargeable lithium batteries (Vincent, 2000) that have a lifespan of 5 to 10 years for low-power drain devices such as pacemakers but can only operate for up to a year at power-densities above 45μW/cm^3 (Roundy et al., 2003). Therefore alternative power sources are required for the long-term operation of the implantable devices currently being developed (Chung et al., 2008; Ebel et al., 1996; Federspil and Plinkert, 2004; Jalilian et al., 2007; Salam et al., 2010; Vaddiraju et al., 2010; Zafar Razzacki, 2004). Although remote powering of implantable devices is in theory possible using transcutaneous energy transmission systems (Joun and Cho, 1998; Miura et al., 2006), in

many situations it is desirable to develop autonomous implantable devices that do not require any external power input. Alternative approaches considered for internally powering autonomous implantable devices include: microbial and enzymatic bio fuel cells (Bullen et al., 2006; Davis and Higson, 2007; Logan and Regan, 2006; Minteer et al., 2007), abiotic fuel cells (Kerzenmacher et al., 2008a), thermal power sources (Yang et al., 2007) and vibrational energy convertors (Cook-Chennault et al., 2008; Gao et al., 2007; Wang, 2006). Abiotic glucose fuel cells (Drake et al., 1970; Kerzenmacher and Sumbharaju, 2007; Rao and Richter, 1974) are promising because they offer reasonable performance and higher stability than enzymatic (Barton et al., 2004; Mano et al., 2003) and microbical glucose fuel cells (Chaudhuri and Lovley, 2003; Rabaey and Verstraete, 2005). Although they offer better stability, thermal power sources and vibration energy convertors have a theoretical power limit that is too low for many implantable devices currently under development.

In Chapter 3, we present a novel abiotic glucose fuel cell that uses a stacked electrode design in order to achieve glucose and oxygen separation. An important characteristic of the fuel cell is that it has no membrane separating the electrodes, which results in low ohmic losses and small fuel cell volume. For reason further described in Chapter 3, this fuel cell has a lot of potential as a coating layer for existing implantable devices, however it is not suitable for low volume applications where.

In Chapter 4, present single-layer fuel cell with good performance (2μW cm^{-2}) and stability that can be stacked to obtain a high volumetric power density (over 16μW cm^{-3}). This represents the first demonstration of a low volume non-enzymatic fuel cell stack with high power density, greatly increasing the range of applications for non-enzymatic glucose fuel cells.

1.2 Nutrition and Health Monitoring

With the increase in obesity and cardiovascular problems in the developed world, nutrition monitoring has become a major concern. In addition, studies have shown that nutritional status affects a patient's response to illness and is even related to a reduced functional capacity of elderly people (Oliveira et al., 2009).

Despite the increase in public awareness, there have been few changes in the methods of nutritional assessments. Typically, a brief nutritional screening, including a physical examination, is used to identify patients in need of in-depth analysis. Despite their importance, nutritional assessments are not common among the general populations, and consequently, deficiencies in calories, proteins, essential fatty acids, vitamins, and minerals often go unnoticed.

There are few methods for *in-vivo* nutritional monitoring since food analysis methods are either too invasive for continuous monitoring or too difficult to miniaturize for on

chip applications. However, a few methods, mainly optical, have been adapted for monitoring living tissues. The advantage of optical methods for *in-vivo* applications lies in the fact they are potentially less invasive than mechanical or electrical methods for nutrient detection. Some groups have demonstrated the potential of optical methods for monitoring the evolution of nutrients on the skin, which is possible because infrared light can travel through tissues and interact with the various components of the skin. (Stamatas and Kollias, 2011) These interactions can alter the intensity, spectral composition and direction of the reflected light that can be collected and analyzed. The information that can be obtained using purely optical methods on the skin, however, is limited because primary nutrients are quickly broken down to their constituents during digestion prior to entering the bloodstream. Consequently, several groups have developed optofluidic methods for analyzing body fluids such as blood and sweat on chips. (Curto et al., 2011) Methods for collecting body fluids including micro-needles (Zahn et al., 2005) and sweat-patches(Kintz et al., 1996) have been developed in parallel. The lab-on-a-chip approach is more versatile because it allows both optical and non-optical sensing methods to be integrated in a common device.

There is a real need for nutritional assessment devices that can evaluate nutritional deficiencies in patients more rapidly and regularly without relying heavily on physicians. In the following sections we review the advances in *in-vivo* optofluidic monitoring in the areas that will likely see rapid innovations in the coming years.

1.2.1 Continuous glucose monitoring for diabetes

Accurate carbohydrate detection, in particular glucose detection, has been a priority for several decades because of the prevalence of diabetes in the world. (Mohan et al., 2007) While this has led to the development of fingerpick tests, accurate and reliable continuous glucose monitoring devices are still not well established. Continuous monitoring of glucose is important because it could prevent issues associated with long periods of hyper- and hypoglycemia. (Ricci et al., 2005) Current FDA-approved needle-type amperometric enzyme electrode devices that monitor glucose continuously such as the ones commercialized by Medtronic require frequent replacement of the enzyme needle. (Hussain et al., 2005) Thus, there is an opportunity for the development of minimally invasive optical sensors that can last much longer without the need for replacing parts.

Yuen *et al.* demonstrated that SERS can be used for monitoring glucose levels *in vivo*. (Yuen et al., 2010) In this case, a sensor chip was functionalized and implanted subcutaneously in a rat, and glucose concentrations in the interstitial fluid were monitored by measuring the surface-enhanced Raman spectra through the skin using spatially offset Raman spectroscopy (SORS). The authors suggested that the combination of SERS and SORS is a powerful technique that can be applied to *in vivo* sensing of other biological targets. Currently, the disadvantage of this approach is the

high cost required for the optical components in such a device.

In vivo glucose detection has also been demonstrated using a functionalized hydrogel-optical fiber, where the detection is based on the glucose-induced contraction of the hydrogel. (Tierney et al., 2009) The hydrogel was fabricated on the end of an optical fiber, and the optical length was measured using an interferometric technique. Another promising method for *in vivo* glucose monitoring is single wall carbon nanotubes (SWNT) fluorescence because the photostability and near IR characteristics of SWNT fluorescence avoid *in-vivo* transmission and sensor lifetime issues. Barone *et al.* has developed two SWNT-based sensors: an enzyme based sensor and an affinity based sensor.(Barone et al., 2004) The Liepmann group at the University of California at Berkeley has developed an electrochemical device that allows for continuous monitoring of glucose. (Zimmermann et al., 2003) The device incorporates a micro-needle patch that draws interstitial fluid onto a chip with incorporated electrochemical sensors.

1.2.2 Identifying deficiencies in protein and essential fatty acids

The importance of a balanced diet containing adequate amounts of proteins and essential fatty acids is well known, however due to the lack of continuous nutritional monitoring methods deficiencies often go unnoticed. Studies have shown low levels or imbalance of essential fatty acids can lead to increases in blood viscosity, vasospasm,

and vasoconstriction and can result in increased risk of several illnesses including osteoporosis. (Kruger and Horrobin, 1997; Simopoulos, 1999) Protein deficiencies, common in both developing and developed countries, can cause a variety of health issues including mental retardation.(Latham, 1997)

Several groups have developed methods for *in vivo* monitoring of essential amino acids. Most methods make use of microdialysis and capillary electrophoresis (CE) techniques.(Sandlin et al., 2005; Zuo et al., 1995) Microdialysis is a popular method because it allows for good temporal resolution. It has been used to investigate neurotransmitters in the brain extracellular fluid and drug delivery.(Kennedy et al., 2002) Following microdialysis, the sample is investigated using either liquid chromatography(LC) or CE, which has been shown to require smaller sample volume and therefore offer better temporal resolution than LC. Zhou *et al.* was one of the first to develop a separation based biosensor capable of near real-time analysis of aspartate and glutamate.(Zuo et al., 1995) Following microdialysis sampling, the primary amine analytes were derivatized before traveling to a microinjection valve and reaching the CE column. Using this system, sample amino acids from brain dialysate were analyzed with a temporal resolution of less than 2 minutes and a detection limit of 0.1μM. More recently, microchip devices for amino acid monitoring with improved temporal resolution, miniaturization, and fluid handling capabilities have been demonstrated. (Nandi et al., 2010; Wang et al., 2010) Dialysis based techniques in conjunction with CE

are useful in the detection of analytes that cannot be detected using conventional biosensors.

Measuring fatty-acid levels in tissue usually involves time consuming processes for extraction and analysis such as gas chromatography.(Liu, 1994) Yoshida *et al.* developed a direct method for measuring dietary fatty acids on human lips using Fourier transform infrared spectroscopy (FTIR) with attenuated total reflection (ATR).(Yoshida et al., 2009) The lips were chosen since they are unaffected by sebaceous activity that could mask changes in lipid composition following ingestion of fatty acids. The transport of docosahexaenoic acid (DHA) from blood vessels to the lips is very rapid and can be detected less than 2 hours after the intake of foods containing DHA. It is noted that, because the lip surface in humans is unique, with less barrier functions than normal skin and blood vessels in the dermis, the transport of biomaterials from blood vessels to the lip surface is more rapid than to other skin surfaces, thus being ideal for the optical detection of a variety of nutrients.

1.2.3 Salts, minerals and vitamin monitoring

Measuring ion concentrations directly in bodily fluids such as sweat can be correlated to electrolyte concentrations in plasma. The Diamond group at Dublin City University has developed a textile based patch with integrated optical detection system for sweat monitoring.(Morris et al., 2009) The device consists of a fluid handling system that

collects the sweat inside a narrow channel that flows over an area with an immobilized pH sensitive dye. A paired emitter-detector dual LED is used to provide continuous quantitative measurements of pH. This approach has several potential applications, including measuring sweat rate during exercise.(Coyle et al., 2010) In addition, the sweat contains other biomarkers that can be used to estimate nutrients levels in the interstitial fluid.

Sweat monitoring has already found commercial applications for drug (Bush, 2008) and cystic fibrosis testing. (LeGrys et al., 2007) Developing microfluidic devices for continuous monitoring of potassium, sodium, and chloride ion concentration could be the next step.

Vitamins are essential compounds that cannot be synthesized in high enough quantity by the body and need to be obtained through diet. Kokaislova *et al.* recently demonstrated the application of Fourier transform SERS spectroscopy for the detection of B-group vitamins riboflavin, nicotinic acid, pyridoxine, and folic acid on both gold and silver surfaces.(Kokaislová and Matějka, 2012) In addition, there are few methods for simultaneous determination of several kinds of fat-soluble vitamins in biological fluids. However, these methods, such as HPLC analysis using diode array detection, usually involve time consuming steps that are not suitable for i*n vivo* applications.(Klejdus et al., 2004) Mata-Granados *et al.* proposed a fully automated method for determining fat soluble vitamins and vitamin D metabolites in serum.(Mata-

Granados and Gómez, 2009) After a multistep separation process, ultraviolet detection was performed at several wavelengths for each target.

1.3 Smartphone Diagnostics

As discussed in section 1.2, there are numerous scientific developments in the areas of personal nutrition and health monitoring, which is not surprising given high commercial potential of such technologies. However in many cases, those technologies require time-consuming protocols, advanced laboratory infrastructure and trained personnel that is hard to translate to the consumer market.[9] In many cases the biggest challenge is the need for low-cost readers to quantify the colorimetric reactions of such immunoassays. Smartphones have the potential of solving this issue. The immunoassay colorimetric reactions could be imaged directly on a smartphone and the processed data can be stored for tracking or sent via e-mail directly to a physician. Increasingly sophisticated camera technology on smartphones can also improve the accuracy of quantifying such colorimetric reactions.

A high-impact area for mobile health, that has not yet taken off commercially, is in the development of biochemical portable diagnostics tools[3]. Smartphone accessories for the detection of biomarkers in bodily fluids could greatly reduce the cost of medical testing and increase global access to healthcare. Several academic groups are currently

developing smartphone platforms for biomarker detection. Recently, Coskun *et al.* [4] have developed a testing platform that can be used at home to test foods for peanut traces and other common allergens. Several other groups are working on smartphone-based image processing for quantifying colorimetric changes on paper-based immunoassays[5].

In chapter 5, we demonstrate an integrated smartphone accessory for monitoring changes in sweat and salivary pH.

In chapter 6, we show that we can use such a system for the quantification of cholesterol levels in blood. Through a series of human trials we demonstrate that the system can accurately quantify total cholesterol levels in blood within 60 sec by imaging standard test strips.

In the Conclusion and Future Work chapter, we discuss the development of the NutriPhone, a platform for vitamin and micronutrient analysis on the smartphone. As a first application, we perform a vitamin D measurements by evaluating serum samples with unknown 25(OH)D concentration and comparing the results to those obtained using a commercial ELISA method.

Chapter 2

Autonomous device for application in late-phase hemorrhagic shock prevention[1]

2.1 Abstract

Hemorrhagic shock (HS) is the leading cause of death for people with traumatic injuries. The onset of HS is correlated with marked changes in the plasma vasopressin levels and some studies indicate that administrating vasopressin in the bloodstream can help stabilize the situation. This situation calls naturally for the use of implantable devices for both the monitoring and treatment of HS. In this work, we present a self-powered hemorrhagic-shock autonomous integrated device (hemoAID) that continuously monitors vasopressin levels and releases vasopressin automatically when levels drop below a certain threshold. We demonstrate that the device can operate at physiological concentrations of vasopressin, in sheep serum, thus paving the way towards the development of an autonomous implantable device for HS prevention.

---

[1] This chapter was published as: Vlad Oncescu*, Seoho Lee*, Abdurrahman Gumus, Kolbeinn Karlsson, David Erickson "Autonomous device for application in late-phase hemorrhagic shock prevention". Under review in PLOS ONE

* These authors have contributed equally to this paper

2.2 Introduction

Studies have correlated the onset of HS with marked changes in the plasma vasopressin levels (Morales et al., 1999; Voelckel et al., 2010). Morales *et al.* have conducted a set of canine experiments where vasopressin levels showed a marked increase at the onset of hemorrhage (to as much as 319pg/mL) followed by a fall to well below the normal physiological level (29pg/mL) as hemorrhage progressed (Morales et al., 1999). In addition, evidence suggests that replenishment of vasopressin at this stage can reverse hypotension in patients (Anand and Skinner, 2012; Wenzel et al., 2008). Krismer *et al.* have reported case studies where dosages of 100 – 160 IU vasopressin led to hemodynamic stability with sinus rhythm in HS patients within 2min and patient survival without additional treatment of up to 90min (Krismer et al., 2005). Therefore, vasopressin can serve as both a biomarker indicative of a critical injury state and a therapeutic agent for treating it. Developing an implantable autonomous device that can provide initial medical treatment when physician care is not readily available is highly suitable in this case.

In this chapter, we present a self-powered hemorrhagic-shock prevention autonomous integrated device (hemoAID) that continuously monitors vasopressin levels in solution and releases vasopressin automatically when vasopressin levels drop below a certain threshold. We demonstrate that the device works at physiological concentrations of

vasopressin in sheep serum. This represents the first steps towards the development of an implantable, self-powered microfluidic device for late-phase HS prevention. In the next sections, we introduce the hemoAID and discuss the fabrication and integration of its major components. We then demonstrate the operation of the device during rapid changes in vasopressin concentration and proceed by discussing the characteristics of the sensing, drug delivery and power units. Finally in the "Conclusion and Future Prospective" section, we discuss some of the issues that need to be addressed in order to move toward a fully integrated autonomous implantable hemoAID.

2.3 Materials and Methods

2.3.1 System Design and Assembly

The hemoAID device shown in Fig. 2.1a consists of a nanowire biosensor for detecting changes in vasopressin levels, an on-board electrochemically driven drug delivery system for administration of vasopressin, and a non-enzymatic glucose fuel cell for powering the system. Those three main functional components are integrated inside a $3cm^3$ package. In this prototype version, the electronic control system is external to the system and uses the circuit shown in Fig. 2.1b. External housing of the circuitry was done to facilitate prototype development and could be integrated into the system in the future. The non-enzymatic glucose fuel cell is used to continuously charge a small

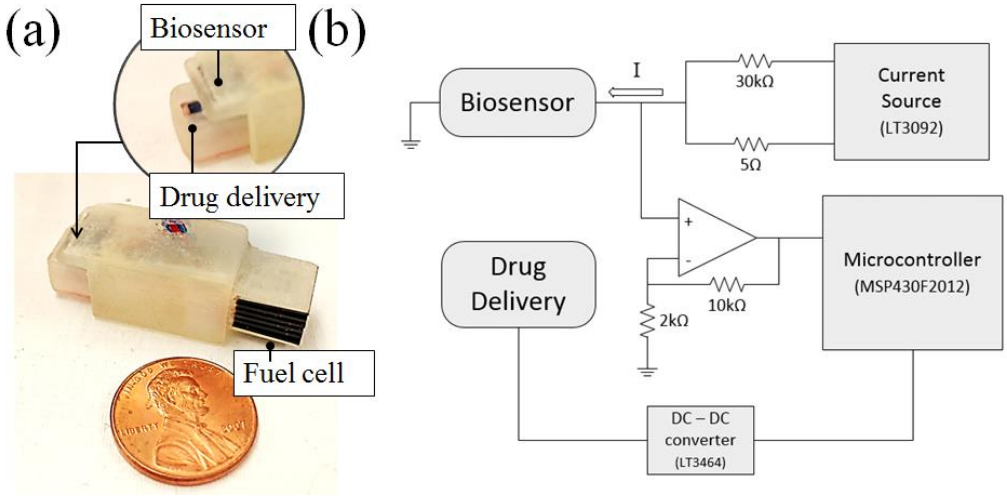

Figure 2.1 hemoAID device for late-phase HS prevention a) Integrated device consisting of a biosensor, drug delivery and fuel cell unit b) schematic of the electrical connections between the different components of the hemoAID

rechargeable battery (Thinergy MEC225) that is then used to power a low power microcontroller (MSP430F2012, Texas Instruments, TX, USA). This set-up allows the device to operate steadily even with significant fluctuations in the power output of the fuel cell unit. During device operation, the sensor is driven by an adjustable 2-terminal current source (LT3092, Linear Technology, Milpitas, CA, USA) at 60mA. The resistance of the sensor changes with the amount of vasopressin in solution, which results in detectable voltage change over the biosensor. In order to improve sensitivity, the voltage is amplified using a non-inverting amplifier (Maxim Integrated, CA) before being detected using a low power microcontroller's analog to digital converter (ADC). If the voltage is lower than the pre-determined threshold, the microcontroller enables the corresponding output pin to activate the drug delivery system. In order to increase the discharge rate of vasopressin in the drug delivery device, the base voltage (3V) is converted to 35V with a micropower step-up DC/DC converter (LT3464, Linear Technology, Milpitas, CA, USA).

2.3.2 Biosensor fabrication

The biosensor consists of gold electrodes and a carbon nanotube (CNT) based detection region on which aptamer molecules are immobilized (He et al., 2013). The detection region of the sensor was patterned on a 4-inch silicon wafer using general photolithography and surface-treated with (3-aminopropyl)trimethoxysilane (APTMS)

using Molecular Vapor Deposition Tool (MVD 100). The aminosilanes from the surface treatment were covalently linked with COOH-functionalized multiwalled CNT (Cheap Tubes Inc.) to serve as carriers of aptamer receptors. The scanning electron microscope (SEM) images of immobilized CNT have been reported in our previous work (He et al., 2013). Electrodes to the detection zone were lithographically patterned, followed by 5nm chromium/60nm gold deposition using a CHA Mark 50 e-Beam Evaporator. The wafer was diced into 0.8cm x 0.5cm pieces which represents significant size reduction from the previous design that measures 5cm x 5cm.

To immobilize the aptamer molecules on the CNT surface, an activation layer was first created by pipetting a mixture of 0.4M 1-ethyl-3-(3-dimethylaminopropyl) carbodiimide (Geno Technology) and 0.1M N-hydroxysuccinimide (MP Biomedicals LLC) in 1:1 volume ratio. The droplet was maintained for 3h at room temperature and cleaned with DI H_2O wash and N_2 dry. Subsequently, 0.1μM aptamer solution was pipetted on the surface-treated CNT and maintained for 24h at room temperature. The premature drying of the droplets for surface modifications was prevented by placing the sensors in a humidified chamber.

2.3.3 Drug delivery device fabrication

The drug delivery consists of three subcomponents: a top layer with a patterned gold electrode and suspended capping membrane, a bottom layer with a patterned gold

counter-electrode and custom packaging to hold the two layers and define a micro-reservoir for vasopressin storage. Fabrication procedures for the top silicon structure are described in details in a previous publication (Chung et al., 2009). Briefly, silicon nitride was deposited on both sides of a silicon wafer using low pressure chemical vapor deposition (LPCVD) followed by gold deposition on the top and patterning for reservoir location on the bottom. The wafer was later immersed in potassium hydroxide (KOH) overnight and reactive ion etching was used to remove the silicon nitride in the patterned reservoir location, leaving a 100μm x 100μm gold capping membrane. Modifications in our new architecture regard the other two components of the device and serve to facilitate subcomponent fabrication and assembly. The replacement of a gold deposited Pyrex layer with a single gold electrode eliminates the standard lift-off processing before the gold deposition. Furthermore, the custom packaging is used in place of PDMS in order to facilitate assembly protocol and reduce leakage of vasopressin through the PDMS. The assembled components were sealed with epoxy adhesive.

2.3.4 Power unit integration

A non-enzymatic glucose fuel cell unit, connected to a rechargeable battery, is used to power the microcontroller and other electrical components of the hemoAID. Lithium batteries were not used here since their short life-time makes them unsuitable for long term autonomous implantable devices with power requirements superior to that of pacemakers (Vincent, 2000). Non-enzymatic glucose fuel cells are promising power sources in such devices due to good long-term stability and adequate power density. Here, we are using the stacked single layer configuration that we have presented previously (Oncescu and Erickson, 2013) to demonstrate integration within the hemoAID. The $1cm^2$ single layer fuel cells are patterned directly on 500μm thick fused silica substrates. A Raney-type Pt/Ni alloy was used as anode for glucose oxidation and a Pt/Al alloy as cathode for oxygen reduction because of increased selectivity as discussed elsewhere (Kerzenmacher et al., 2008a; Oncescu and Erickson, 2011). The fuel cell unit is composed of 12 single layer fuel cells that are connected externally in parallel to form a fuel cell stack and integrated inside of custom holder with a volume of approximately $1cm^3$.

2.4 Results and Discussion

2.4.1 Integrated device operation in flow network

In order to demonstrate its operation, the hemoAID device was placed inside a closed chamber within a fluid network designed to simulate the physiological vasopressin states of late-phase HS patients. According to a clinical study by Jochberger *et al.* vasopressin concentration for patients with hemorrhagic shock rises from the normal 6±3pM range to 52±30pM as the body tries to reverse hypotension by releasing vasopressin (Jochberger et al., 2006). Following this initial increase, the level of vasopressin starts decreasing, which indicates the onset of late phase hemorrhagic shock. At that point, administering a high dose of vasopressin can temporarily stabilize the situation. Here, we demonstrate the operation of the hemoAID at those physiologically relevant vasopressin concentrations. The test chamber housing the integrated device (Fig. 2.2a) is initially filled with 100pM vasopressin solution, which corresponds to the high initial value (52±30pM) of blood vasopressin for patients prior to late-phase HS onset. The vasopressin concentration is then progressively lowered by introducing 10pM solution into the chamber using a VWR Mini-Pump at a flow-rate of 0.115ml/s. The decrease in vasopressin concentration, indicating late-phase HS, causes a decrease in resistance resulting in a voltage output drop across the nanowire sensor at constant current. This resistance drop across the sensor can be correlated to the vasopressin concentration. As shown in Fig. 2.2b, the sensor's resistance decreased over 14min in response to the decrease in

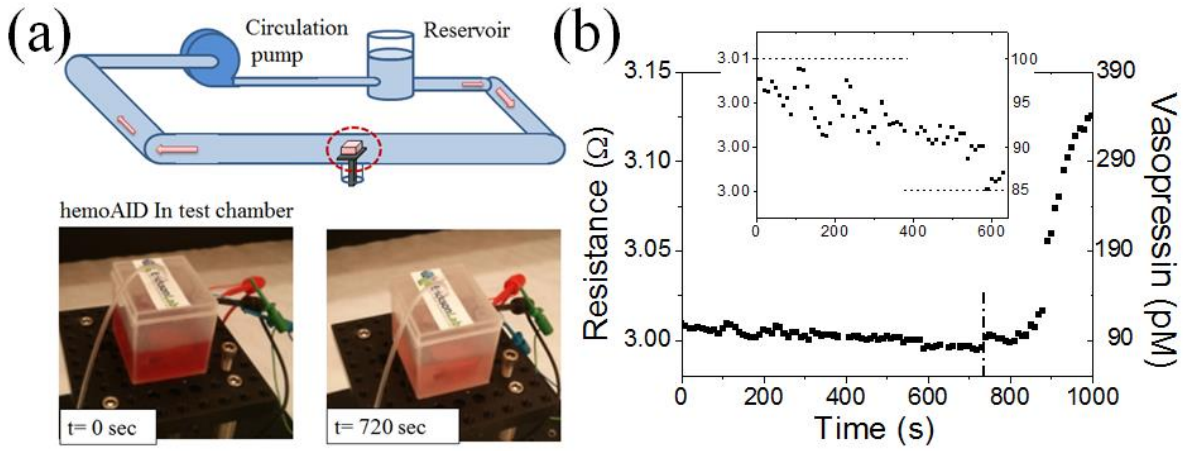

Figure 2.2 Setup and experiment simulating vasopressin concentration changes in late-phase HS a) Setup for integrated device testing simulating late-phase HS b) resistance change, and associated vasopressin concentration change, detected by the biosensor during integrated experiment simulating late phase HS changes in vasopressin concentration. For the first 720s the vasopressin concentration is gradually lowered until the drug delivery is autonomously activated to counteract the drop in vasopressin (at 15% drop). The line at 720s shows the point at which drug delivery is activated. The inset shows the vasopressin drop before the drug delivery is activated (simulating the onset of late-phase HS)

vasopressin levels. Upon reaching a pre-determined 15% decrease in vasopressin concentration, corresponding to 0.25% resistance decrease ratio, the drug delivery is activated autonomously by the application of 35V between the top and bottom electrodes which results in the release of 16μL of highly concentrated (200μM) vasopressin. The localized vasopressin release was detected successfully by the sensor as can be seen in Fig. 2.2b. This temporary increase in vasopressin would allow a patient to survive until further medical assistance can be provided. The data obtained from the sensor is in the form of a voltage at the supplied current of 60mA. This can be transformed into a resistance change that is related to the vasopressin concentration change in solution via the following experimentally derived equation:

$$\Delta[VP] = 57.64\ \Delta R + 102.68 \qquad (2.1)$$

In the above equation $\Delta[VP]$ is in pM and ΔR is a % change in resistance. The relationship between changes in resistance and concentration is further discussed in the next section and is based on experiments presented elsewhere[20].

2.4.2 Biosensing ability of integrated device

The nanowire biosensor we have developed and integrated in the hemoAID allows for the detection of pM changes in vasopressin concentration. Immobilized aptamer molecules on the nanowire biosensor act as electrical

bioreceptors for the surrounding vasopressin. Reversible vasopressin binding leads to changes in conductivity through the CNT detection zone. The sensor is based on a device developed previously with a limit of detection of 43pM in standard solution (He et al., 2013). In this section, we demonstrate the sensing ability of the hemoAID for gradual changes in vasopressin levels by performing several characterization experiments. First, we show the reversibility of our sensor's detection mechanism by monitoring the sensor response to alternating vasopressin concentrations in a single experiment. The biosensor was placed into a custom packaging with micro-channels as shown in Fig. 2.3a and 0.01M Phosphate Buffer Saline (PBS) solution was introduced through one inlet until the output current was stabilized. The flow of 0.01M PBS was stopped after 20s and 10μM vasopressin was allowed to flow through the other inlet, which was again replaced by a PBS injection after another 30s. As shown in Fig. 2.3b, the initial introduction of a high-concentration 10μM vasopressin solution results in a current decrease, and resistance increase, through the sensor almost instantaneously which is a consequence of depletion of charge carriers on the CNTs due to vasopressin to aptamer binding. The recovery of current upon 0.01M PBS injection at t=50s is due to the release of vasopressin molecules from the immobilized aptamer which demonstrates the reversible nature of the binding events. The slower rate of current change during the dilution is due to

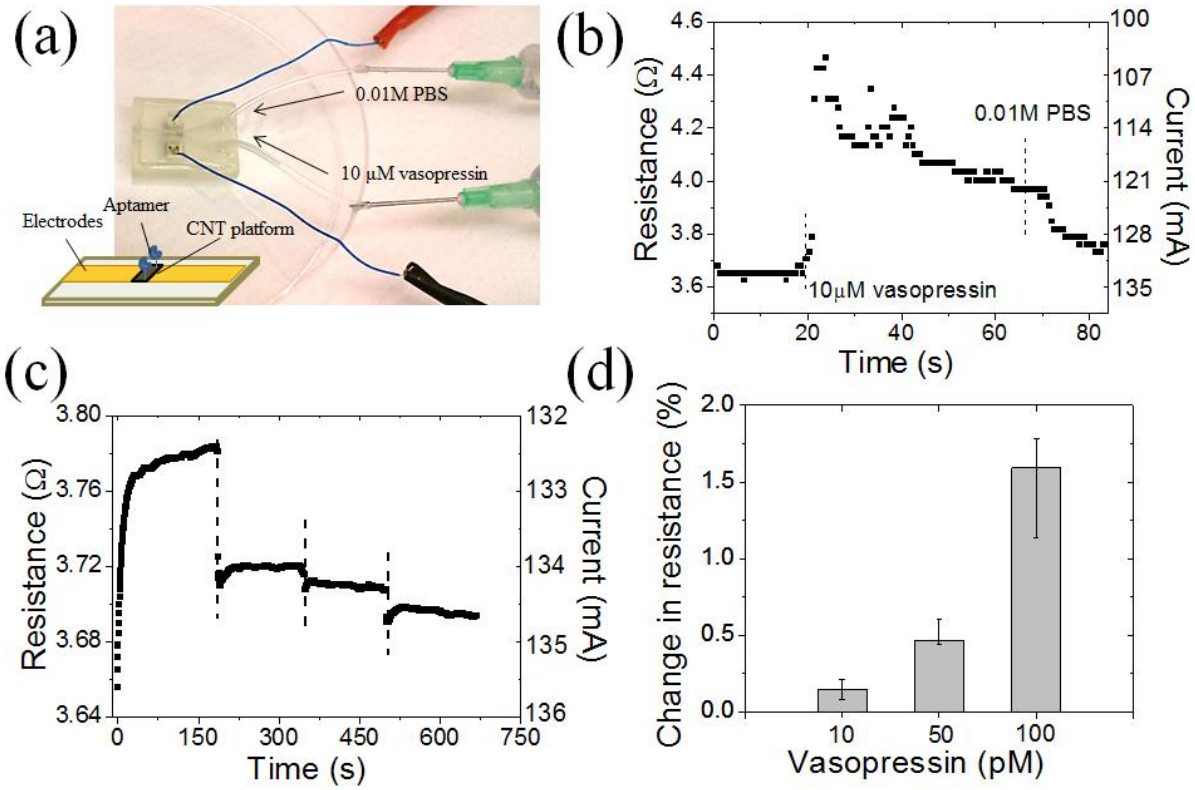

Figure 2.3 Biosensor characterization a) Schematic of the nanowire biosensor and picture of the flow through system b) demonstration of sensor reversibility c) resistance, and associated current, change due to continuous decrease in vasopressin concentration in sheep serum. At t=0 sheep serum with 100pM vasopressin is introduced, followed by 50pM, 10pM and with no additional vasopressin d) Percentage change in resistance from the initial no vasopressin case caused by the flow of sheep serum with different vasopressin concentrations (average of 5 experiments with the error bars representing the highest and lowest reading)

the low dissociation constant of aptamer-vasopressin complex, confirming the high affinity of aptamer molecules to vasopressin.(Maehashi et al., 2009) This experiment demonstrates the biosensor's rapid reversibility even when a high vasopressin concentration causes large changes in resistance, uncommon under normal physiological conditions. In addition, we show that the sensor can be used to monitor physiologically relevant changes in serum vasopressin concentration. In Fig. 2.3c, the biosensor is subjected to continuous variations in vasopressin by flowing sheep serum (Valley Biomedical Inc.) with 100pM, 50pM, 10pM and 0pM of added vasopressin in the respective order for a period of 150s at each concentration. With each dilution, the current through the sensor increases as expected due to the release of vasopressin from the immobilized aptamers. In Fig. 2.3d we show the percentage change in current from the initial no vasopressin case due to the addition of 10pM, 50pM and 100pM vasopressin. The bar graph represents the average of 5 experiments that were performed by continuously varying the concentration of vasopressin as shown in Fig. 2.3c, with the error bar representing the range between the highest and lowest reading. These experiments demonstrate that the sensor can detect physiologically relevant changes in vasopressin in serum.

The high current used to increase the sensitivity of the sensor in the previous section can be decreased by changing the design of the sensor to increase its

resistance either by decreasing the thickness of the nanowire sensing area on which APTMS is immobilized or by integrating several such nanowires in series. With these improvements, the sensor can be used for detection of vasopressin in interstitial fluid where changes in vasopressin are gradual and not affected by pressure changes in the bloodstream.

2.4.3 Stabilizing vasopressin levels through drug delivery

In this section we demonstrate the integrated device's mechanism to stabilize vasopressin levels through the in-parallel operation of the drug delivery system (Fig. 2.4a) with the biosensor. Time-controlled ejection of vasopressin based on electrochemical principles as shown in Fig. 2.4b has been demonstrated in previous publications (Chung et al., 2009; Cordovez et al., 2010). To release vasopressin, electrical potential is applied between the top and bottom electrodes which results in two distinct reactions. The first is the electrolytic reaction in the reservoir that causes gas bubble formation and pressure build-up as a result. The second is the reaction between the chlorine ions in the buffer solution and the gold capping membrane to form a water soluble complex that gradually dissolves until it ruptures with increasing pressure of the reservoir. In the experiment presented in Fig. 2.4c, the sensor and the capping membrane of the drug delivery system were aligned 50mm apart using a custom holder and

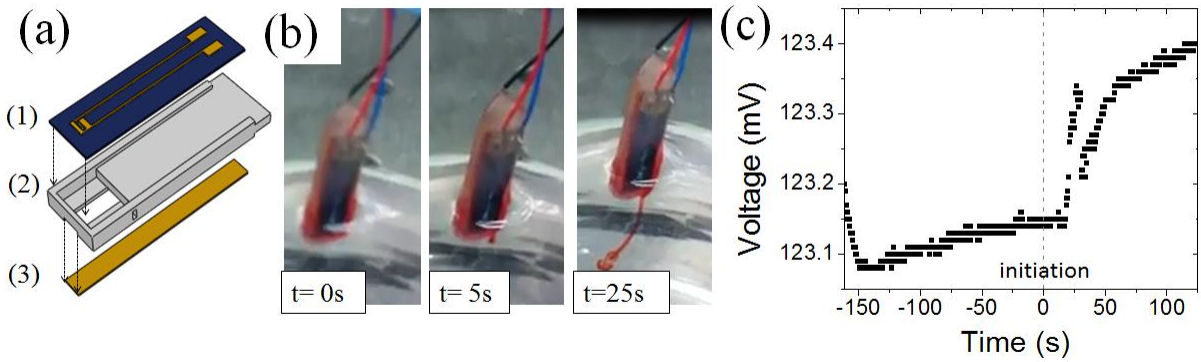

Figure 2.4 Electrochemical drug delivery device a) Assembly of the drug delivery unit b) vasopressin ejection over 25s of applied voltage c) increase in biosensor voltage due to drug delivery. The vertical dotted line indicates when the potential was applied (at t=0s) and the a sustained spike in voltage occurs after 25s

immersed in a 0.01M PBS solution. After approximately 162s, the voltage output has stabilized (at t=0s on the graph), and the drug delivery was initiated by the application of a 35V potential between the top and bottom electrodes of the drug delivery system. The electrochemical ejection procedure has been imaged to suggests the onset of gold membrane rupture 5s after the potential application (Cordovez et al., 2010) and a sustained spike in voltage is first observed after 25s. The small magnitude of this signal (0.25mV) and the slow response of the sensor are due to large distance between the sensor and the drug delivery device. In the integrated hemoAID device, and the experiment in Fig. 2.4b the sensor is placed 5mm in front of the sensor and the release of 16μL vasopressin solution at 200μM causes a much more rapid and larger voltage increase of 3.7%. This experiment demonstrates the ability of the sensor to monitor sudden changes in vasopressin concentration due to drug delivery by measuring the increase in voltage even when the two components are not in direct proximity.

2.4.4 Powering of integrated device

Instead of using the fuel cell unit directly to power the device, a small rechargeable battery shown in Fig. 2.5a is used as an intermediate in order to decrease power supply fluctuations. In addition this also allows excess energy to be stored and used for the one-time operation of the drug delivery device.

The power consumption for the integrated device with the sensor operated continuously is around 60mA at 3V. This is well above what can be supplied by a 1cm^3 fuel cell unit (20μA at 0.15V) however most of the power is required by the biosensor since the change in resistance across the detection area is directly proportional to the current applied. Although decreasing the current supply is in theory possible, this results in lower detection sensitivity. However, the microcontroller only requires 60 to 70μA at 3V to operate and we can operate the sensor at discrete time intervals, thus greatly reducing the power consumption of the system and making it possible to operate the system using a 1cm^3 fuel cell unit. In Fig. 2.5b we show the chronoamperometric response of the fuel cell unit (composed of 12 stacked single layers) at 0.1V in 0.01M PBS solution (pH 7.4) and physiological levels of glucose and oxygen (5mM glucose, 8% oxygen saturation) over a period of 10h. In Fig. 2.5c we show the discharge profile of the Thinergy MEC225 with an operating current of 100μA. By continuously charging the Thinergy battery the system can operate continuously over a long period of time and avoid the power fluctuations typical of glucose fuel cell units (±4% as can be seen in Fig. 2.5b).

2.5 Conclusion

In this chapter, we have introduced the hemoAID, a device that can be used to detect a gradual drop in vasopressin concentration, corresponding to the onset of late-phase hemorrhagic shock, and deliver a highly concentrated dose of vasopressin to help stabilize the situation. We have demonstrated its operation in a controlled fluidic environment in which a 15% drop in vasopressin concentration was sensed and automatically triggered the activation of the drug delivery system. We discussed the sensor's mechanism and ability to operate in a complex medium such as sheep serum thus opening the door to the development of an implantable device for late phase hemorrhagic shock prevention.

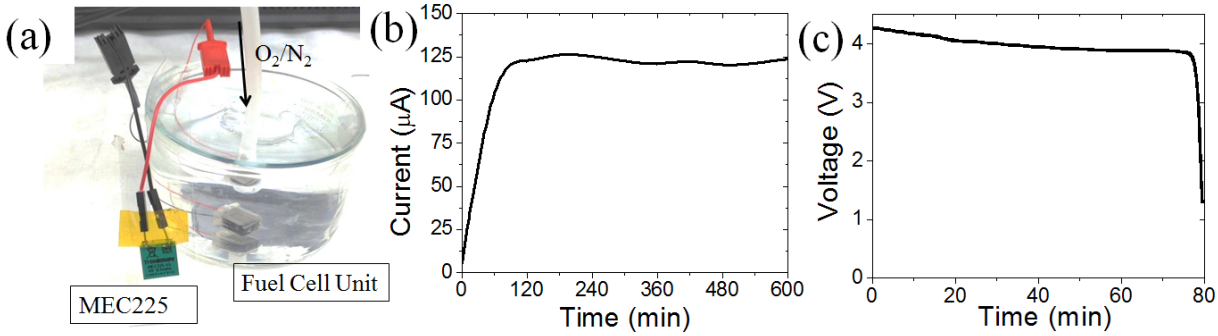

Figure 2.5 Power unit characterization a) Power unit consisting of a 1cm^3 fuel cell unit in 5mmol glucose solution at 8% O_2 saturation and an external rechargeable battery b) chronoamperometric response of the fuel cell unit at 0.1 V in 0.01 M PBS solution and 5mmol/L glucose solution over a period of 10h c) discharge profile for the rechargeable battery at an operating current of 100μA

Chapter 3

Microfabricated Enzyme-Free Glucose Fuel Cell for Powering Low-Power Implantable Devices[1]

3.1 Abstract

In the past decade the scientific community has showed considerable interest in the development of implantable medical devices such as muscle stimulators, neuroprosthetic devices, and biosensors. Those devices have low power requirements and can potentially be operated through fuel cells using reactants present in the body such as glucose and oxygen instead of non-rechargeable lithium batteries. In this chapter, we present a thin, enzyme-free fuel cell with high current density and good stability at a current density of 10 μA cm^{-2}. A non-enzymatic approach is preferred because of higher long term stability. The fuel cell uses a stacked electrode design in order to achieve glucose and oxygen separation. An important characteristic of the fuel cell is that it has no membrane separating the electrodes, which results in low ohmic losses and small fuel cell

[1] **Oncescu, V**., Erickson, D. "A Microfabricated Low Cost Enzyme-Free Glucose Fuel Cell for Powering Low-Power Implantable Devices" *Journal of Power Sources* 196, 9169-9175 (2011)

volume. In addition, it uses a porous carbon paper support for the anodic catalyst layer which reduces the amount of platinum or other noble metal catalysts required for fabricating high surface area electrodes with good reactivity. The peak power output of the fuel cell is approximately 2μW cm^{-2} and has a sustainable power density of 1.5 μW cm^{-2} at 10 μA cm^{-2}. An analysis on the effects of electrode thickness and inter electrode gap on the maximum power output of the fuel cell is also performed.

3.2 Introduction

The ability of different abiotic catalysts to catalyze oxygen and glucose reactions has been extensively studied. It was demonstrated that several catalysts such as silver and activated carbon can selectively catalyze oxygen reduction in the presence of glucose while platinum alloys such as platinum-bismuth can catalyze glucose oxidation in deaerated solutions. To date, no abiotic catalyst material has been found to selectively catalyze glucose oxidation in the presence of oxygen (Kerzenmacher et al., 2008a). In order to get around the catalyst selectivity issue, a stacked electrode approach has been used to achieve reactant separation (Kerzenmacher et al., 2011; Rao and Richter, 1974). In this approach, a permeable cathode that selectively catalyzes oxygen reduction is placed in front of the anode, thus removing some of the oxygen from the solution before it defuses to the anode allowing glucose oxidation to proceed at low oxygen concentrations. Porous cathodes have been fabricated either by suspending the cathode catalyst

material in a hydro-gel and spreading the mixture onto a current conducting platinum mesh (Kerzenmacher et al., 2011) or by etching holes through a silicon cathode support before depositing the catalyst layer. Since the last approach doesn't require a conducting platinum mesh, it is more suited for fabricating highly compact electrodes. In order to increase the surface area of the electrodes, several methods such as Raney type alloying and coating of the silicon wafers with carbon nanotubes have been used (Rao et al., 1976).

In this chapter we demonstrate the advantage of fabricating the cathode using a thin platinum catalyst layer deposited on a carbon paper membrane. Since the carbon paper is conductive, porous, and has a high surface area, the platinum catalyst layer can be deposited directly on the membrane thus requiring less platinum catalyst and less intermediate steps in order to obtain a high surface area electrode. Section 3.3 gives an overview of the theory behind abiotic glucose fuel cells and some important characteristics affecting performance for the stacked electrode design. Section 3.4 goes over the fabrication of the fuel cell presented in this chapter, section 3.5 describes the experimental setup and section 3.6 presents the experimental results.

3.3 Abiotic glucose fuel cell theory and operation

Glucose fuel cells produce electrical current through a proton coupled electron transfer (PCET) reaction where oxygen is reduced at the cathode and glucose is oxidized at the anode. Assuming glucose is oxidized to gluconic acid, the

theoretical cell voltage of a fuel cell is 1.3V (Kerzenmacher et al., 2008a). The open circuit voltage is however much lower than that due to fuel and oxidant cross-over resulting in mixed potentials at both electrodes. Cross-over occurs when both fuel and oxidant react at the same electrode, a situation that is unavoidable in glucose fuel cells operating *in-vivo* where glucose and oxygen are hard to effectively separate before reaching the electrodes.

The stacked electrode design takes advantage of the fact that the physiological concentration of glucose is two orders of magnitude higher than that of dissolved oxygen (Kerzenmacher et al., 2008a). Consequently most of the oxygen is reduced before crossing the porous cathode while only a small fraction of the glucose is oxidized. The glucose oxidation reaction can therefore proceed at the anode under low-oxygen conditions. In this manner, stacked electrode fuel cells can achieve good power output despite poor electrode selectivity. In order to reduce the amount of oxygen reaching the anode and competing with the glucose oxidation reaction, it is possible to increase the thickness of the cathode. However, we will show experimentally in section 3.6.4 that this also reduces the maximum power output of the full cell by decreasing glucose diffusion to the anode.

When a small current is drawn from a fuel cell, the actual voltage is lower than the theoretical voltage due to activation losses. Activation losses depend on the nature of the catalyst and are significant in abiotic glucose fuel cells due to slow reaction kinetics at the electrodes. As the current is increased the cell voltage

drops linearly due to ohmic losses in the fuel cell caused by the relatively poor conductivity of the electrolyte. The resistance of the electrolyte is given by:

$$R = L/(\sigma A) \tag{3.1}$$

where L is the distance between electrodes, σ is the electrical conductivity and A is the cross-sectional area of the electrolyte. From Eq. 3.1 it can be seen that increasing the gap between the electrodes increases the ohmic losses in the fuel cell. In addition, separating the electrodes by a porous filter membrane, as is commonly done, greatly decreases the electrolyte cross-sectional area and increases ohmic resistance (Kerzenmacher et al., 2011). In this chapter, we have assembled the fuel cell without a filter membrane in order to avoid this problem. Decreasing the inter-electrode gap also produces a higher glucose concentration gradient at the anode. The relationship between current density and the concentration gradient is given by:

$$i/A = (Co - Cb)/\delta \tag{3.2}$$

where i/A is the faradaic current density, n is the number of electrons transferred, F is the Faraday constant, D is the diffusion coefficient and (C_o-C_b) is the difference between the concentration at the electrode surface and the bulk concentration over the Nernst diffusion layer thickness δ. Fig. 3.1 shows the main sources of voltage losses that occur in glucose fuel cells as well as the change in glucose concentration through the inter-electrode gap.

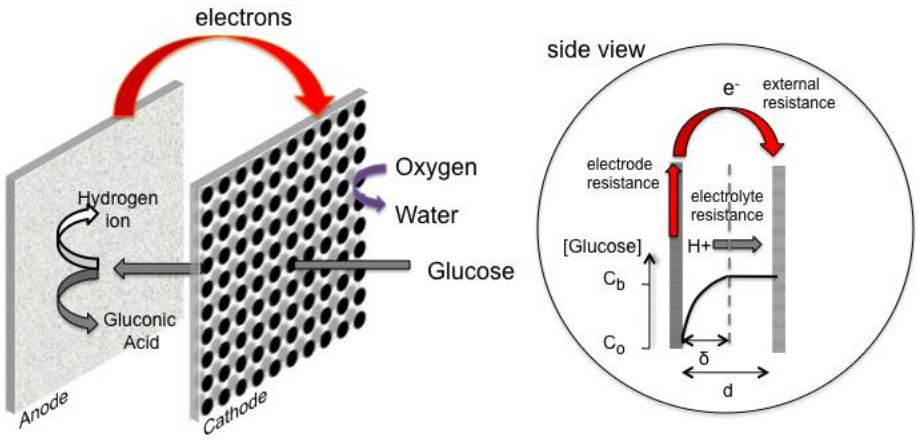

Figure 3.1 Stacked glucose fuel cell principle of operation. Stacked glucose fuel cell structure with cell resistance losses and glucose concentration profile in the inter-electrode gap

Despite the positive effects of reducing the distance between electrodes, it is shown experimentally in section 3.6.4 that the maximum power density actually decreases as the distance between electrodes decreases below a certain critical length. This occurs when inter-electrode gap length approaches the Nernst diffusion layer thickness and starts affecting the concentration gradient at the anode. Other issues affecting performance at small inter-electrode gaps include hydrogen bubble formation in the inter-electrode gap (Nagai, 2003) and accumulation of reaction products, such as gluconic acid and hydrogen ions, at the anode surface due to poor diffusivity through the membrane. The latter also affects the pH in the inter-electrode gap and has a large effect on the reaction rates at the electrodes.

3.4 Fabrication

3.4.1 Anode fabrication

The steps for the anode microfabrication are shown in Fig. 3.2. A four inch silicon wafer was used as substrate for the catalyst layer deposition. High surface area Raney type anodes for glucose oxidation are obtained by alloying platinum with nickel and subsequently extracting the unalloyed nickel. It was demonstrated (Rao et al., 1976) that depending on the initial nickel to platinum ratio, such catalysts exhibit up to nine times higher current densities in deaerated phosphate

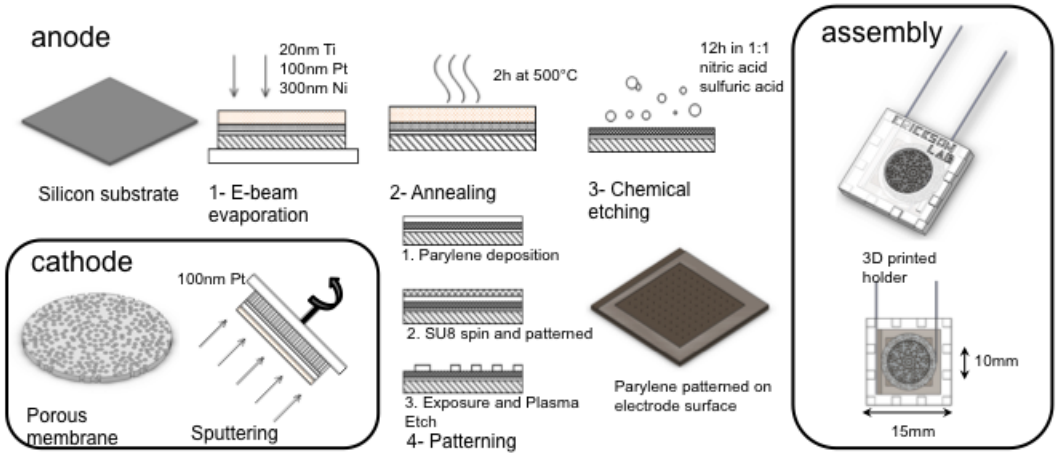

Figure 3.2 Anode and Cathode fabrication. Fabrication and assembly steps of the stacked electrode glucose fuel cell

buffer than conventional platinum black electrodes. E-beam evaporation (CHA Evaporator) was used to deposit 20nm of titanium in order to promote adhesion followed by 100nm of platinum and 300nm of nickel. The wafer was subsequently annealed for 2 hours in nitrogen gas at 500°C (MRL Industries Furnace). In order to avoid oxide formation when opening and closing the furnace door, the stand-by temperature of the furnace was kept below 300°C. The sheet conductivity of the wafer after each process step was measured using a CDE ResMap Resistivity 4 point Probe to ensure that no oxide layer would form at the surface and reduce the surface conductivity of the electrode. The wafers were then kept in 1:1 solution of sulfuric acid and nitric acid for 12 hours in order to ensure that all the unalloyed nickel has been removed. Upon removal, X-ray photoelectron spectroscopy (XPS) analysis on the wafer was performed and it showed no traces of unalloyed nickel. The inter-electrode gap was patterned directly on the cathode using parylene for electrical insulation and SU-8 photo resist for setting the desired inter-electrode gap size. Approximately 2μm of parylene was deposited using a Parylene Coating System. The SU-8 photoresist was then spun and patterned directly on top of the parylene. The patterned wafer was later diced in 15mm by 15mm squares using a K&S 7100 Dicing Saw. The parylene was then etched in oxygen plasma through the SU-8 mask using a

Oxford PlasmaLab 80+ RIE System and the depth of the pattern was measured using a P-10 Profilometer tool.

3.4.2 Cathode fabrication

The cathode for oxygen reduction was fabricated by sputtering platinum directly onto a porous substrate. The porosity and structure of the support membrane has a strong effect on the amount of glucose and oxygen that passes through the cathode. Consequently several types of membranes were considered and two chamber diffusion experiments, not shown in this chapter, were performed in order to characterize the diffusion through those membranes. Based on these experiments, Teflon coated carbon paper (Toray TGP-H-090) and anodized aluminum oxide membranes (Whatman AAO) were selected. Scanning electron microscope (SEM) images of the two membranes are presented in Fig. 3.3. The carbon paper membrane is 300μm thick and has the advantage of being conductive and having a high surface area. The AAO membrane is non-conductive and has a relatively small surface area but has the advantage of being only 60μm thick, which in principle allows for the fabrication of smaller more compact fuel cells with better glucose diffusion to the anode. The catalyst layer was obtained by directly sputtering 100nm of platinum onto each side of the porous membranes. Better platinum coverage inside the pores was obtained when the porous membranes were rotated during deposition. Sections 3.6.1 to 3.6.3 present experimental results for fuel cells assembled using a carbon paper

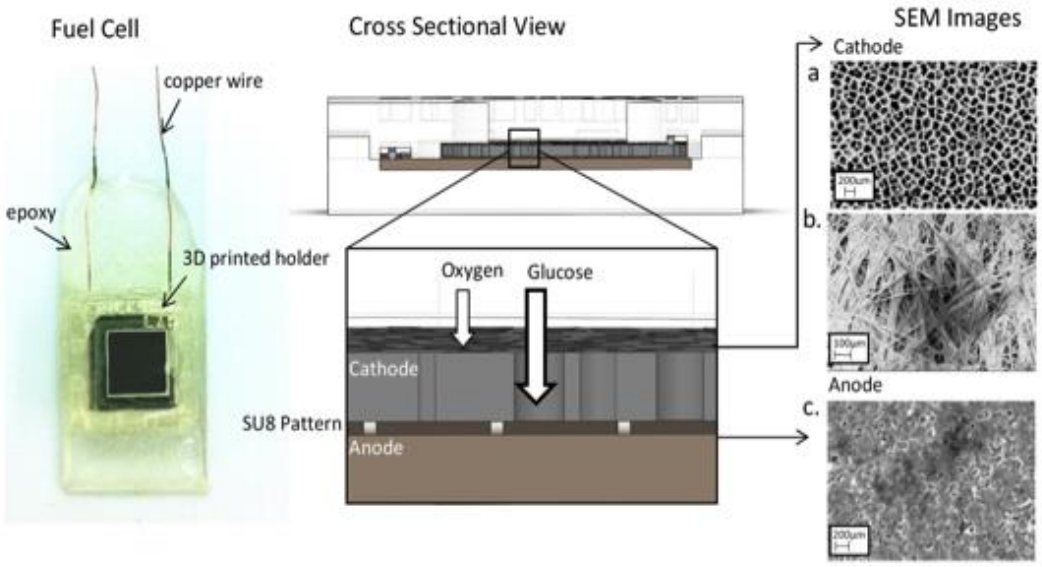

Figure 3.3 Assembled fuel cell. Assembled fuel cell and SEM images of (a) AAO membrane cathode, (b) carbon paper porous cathode and (c) platinum-nickel alloyed anode

supported cathode, while section 3.6.4 presents performance comparisons between fuel cells with carbon paper and AAO membrane supported cathodes.

3.4.3 Fuel cell assembly

Copper wires (28 Gauge L.J Leahy) were bonded to the electrodes using silver epoxy (M.G. Chemicals). The electrodes were then held together in a specially designed 3D printed holder and epoxy (Hardman Double Bubble Epoxy) was used to seal the two parts of the holder together. Fig. 3.3 shows an assembled fuel cell mounted on a glass slide as well as scanning electron microscope SEM images of the anode and cathode surfaces.

3.5 Experimental setup and procedure

3.5.1 Fuel cell testing environment

All experiments were carried out under controlled conditions at physiological levels of glucose (5.0 mmol L^{-1}) and dissolved oxygen (7% saturation) in 0.01M phosphate buffer saline (pH 7.4) at 37^{o}C using a setup similar to the one described by Kerzenmacher *et al* (Kerzenmacher et al., 2011) and presented here in Fig. 3.4a. Two flow meters (VWR 20–200 SCFM) were used to adjust the ratio of air and nitrogen (Airgas NI-200) flowing in the solution. In order to have a more stable environment and to minimize rapid changes in oxygen concentrations, the testing chamber was divided in two parts: one where the fuel

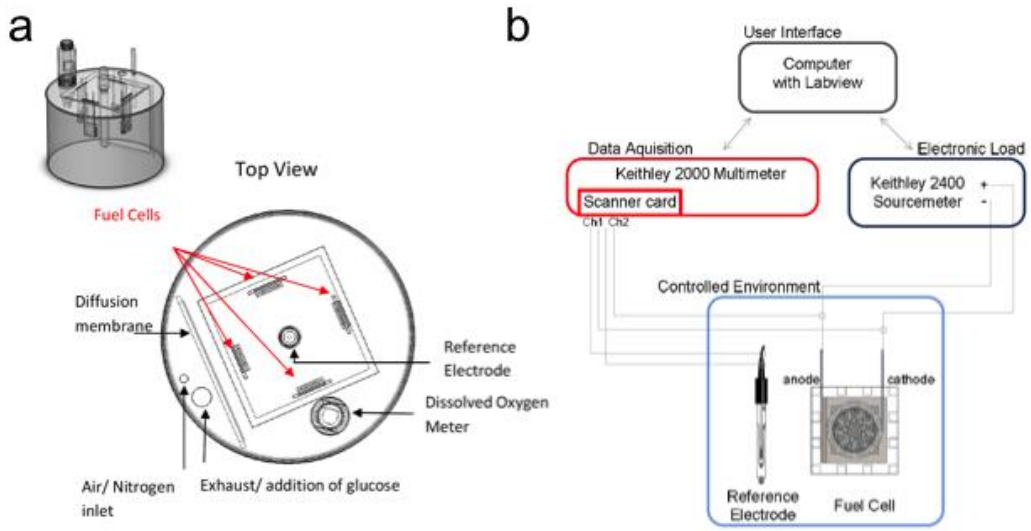

Figure 3.4 Experimental setup (a) Controlled experiment set-up for fuel cell testing (b) Electrical testing set-up

cells are kept and one where the nitrogen and glucose are introduced. A porous membrane separated the two compartments of the testing chamber. Up to four different fuel cells were tested simultaneously using this setup. A dissolved oxygen meter was used to continuously monitor the oxygen levels and temperature. A Silver-Silver chloride reference (Aldrich Double junction Ag/AgCl reference) electrode was used as the reference against which electrode potentials were measured.

3.5.2 Electrical testing setup

As illustrated in Fig. 3.4b, a Keithley 2400 Source-meter was used to apply a current sweep across the fuel cells and a Keithley 2000 Multi-meter equipped with a scanner card was used to take the voltage measurements of individual electrode potentials versus the reference electrode. The current sweep and channel switching was remotely controlled using a LABVIEW program. All current- potential characterization experiments were performed at a low sweep rate of 9 $\mu A\ h^{-1}$ in order to ensure that the readings were taken at a stable potential.

3.6 Experimental results

3.6.1 Electrode characterization experiments

Characterizing the individual performance of the cathode prior to integration in the fuel cell was carried out using a 3 electrode setup with a silver-silver chloride reference electrode and a carbon-paper auxiliary electrode. The potential versus current curves are shown in Fig. 3.5a for both the platinum on carbon paper electrode and the carbon paper electrode. A positive potential indicates that there is a cathodic current and that the oxygen reduction occurs as expected at the working electrode. It can be seen that the platinum on carbon paper electrode shows much better oxygen reduction potential than the carbon paper alone. The platinum on carbon paper electrode was prepared as described in section 3.2 by sputtering 100nm of Pt on both sides of the carbon paper. Preliminary experiments, not shown in this chapter, with a higher amount of sputtered platinum on the carbon paper did not result in higher cathodic current, indicating that 100nm is enough to fully coat the carbon paper with a catalyst layer. In addition, the open circuit voltage (OCV) of the electrode Platinum-Nickel electrodes against the Ag-AgCl reference electrode at different oxygen partial pressures is presented in Fig. 3.5b. It can be seen that due to the high reactivity of oxygen at the platinum surface, the OCV increases rapidly between 0% and 1% oxygen saturation. This demonstrates the necessity of fabricating the cathode in a way that minimizes the access of the oxygen to the anode.

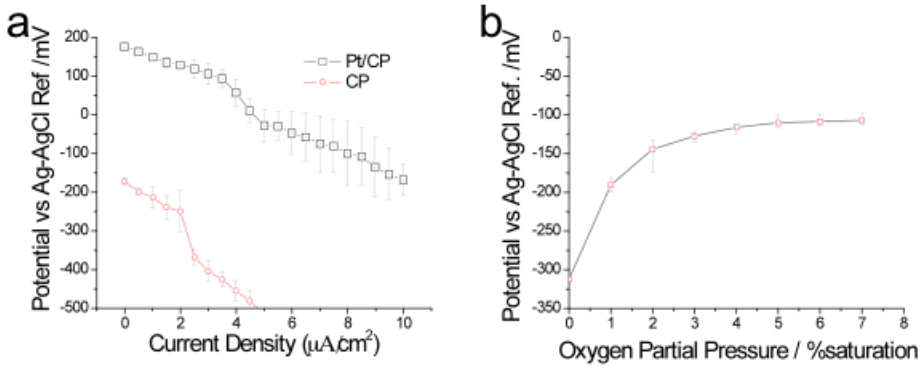

Figure 3.5 Electrode characterization (a) Potential versus current density plot for carbon paper (CP) and platinum on carbon paper (Pt/CP) cathodes (b) Effect of oxygen partial pressure on Pt/Ni electrode potential

3.6.2 Overall fuel cell performance

The overall performance of the glucose fuel cell with carbon paper supported cathode was characterized using the setup described in section 3.4.4. Fig. 3.6a shows the cell potential and power density versus current density. The median value of three different experiments is indicated by the symbol and the error bars indicate the maximum and minimum experimental value. The peak power output for the cell is just under 2 $\mu W cm^{-2}$ and occurs at a current density of 15 $\mu A\ cm^{-2}$. Although the peak power output is lower than what has been reported elsewhere for mesh-free stacked fuel cells, the current density is much higher indicating better electrode kinetics. In addition, the fuel cell presented in this chapter uses only 300nm of platinum catalyst, over 100 times less than previous mesh-free designs, making it a relatively low-cost power source with a power density high enough for powering implantable sensor devices. Fig. 3.6b shows the power density of a fuel cell at a constant current density of 10 $\mu A\ cm^{-2}$ over a period of 4 hours. A large initial drop in power density is observed due to the slow load change response of the fuel cell, however after a few minutes a stable power density of about 1.5 $\mu W\ cm^{-2}$ is reached. A power drop of less than 0.2 $\mu W\ cm^{-2}$ is observed over the next 4 hours demonstrating that the carbon paper supported fuel cell is relatively stable at large current densities. The stable power density of 1.5 $\mu W\ cm^{-2}$ at 10 $\mu A\ cm^{-2}$ is consistent with the data presented for the

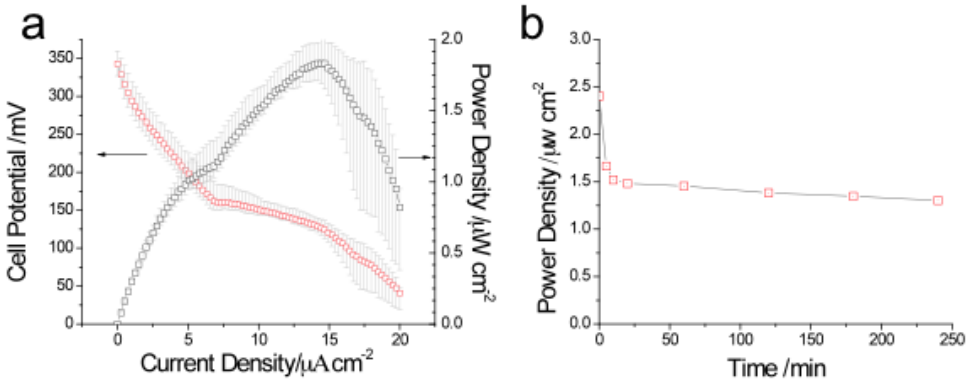

Figure 3.6 Overall fuel cell performance (a) Dependence of cell voltage and power density on current density (b) Cell Voltage versus time at 10μW over a period of 4h

polarization curve in Fig. 3.6a demonstrating that a sweep rate of 9 μA h^{-1} did not lead to an overestimation of the performance.

3.6.3 Effect of inter-electrode gap and cathode thickness

The fuel cell presented in the previous sections had an inter-electrode gap size of 160 μm and a cathode thickness of 300 μm. As described in section 2, it is expected that the gap between the electrodes to be an important factor determining fuel cell performance. In order to see the effect of the inter electrode gap on the maximum power output of the fuel cell, different gap thicknesses (50μm, 100μm, 160μm and 260μm) were patterned directly on the anode using SU-8 photoresist. The gap pattern was fabricated using standard photolithography techniques as described in section 3 and the height of the pattern was measured using a P-10 Profilometer tool. Three fuel cells of each gap size were assembled and tested and the results are presented in Fig 3.7a. It can be seen that the 160μm gap electrode gave the maximum power density of 2 μWcm^{-2}. As mentioned is section 2, the decrease in performance can be attributed to the change in concentration gradient at the anode as the gap size approaches the Nernst diffusion layer thickness. However, other effects such as hydrogen bubble formation at the anode and accumulation of reaction products at the electrode surface due to poor diffusivity through the membrane can also contribute to these observations.

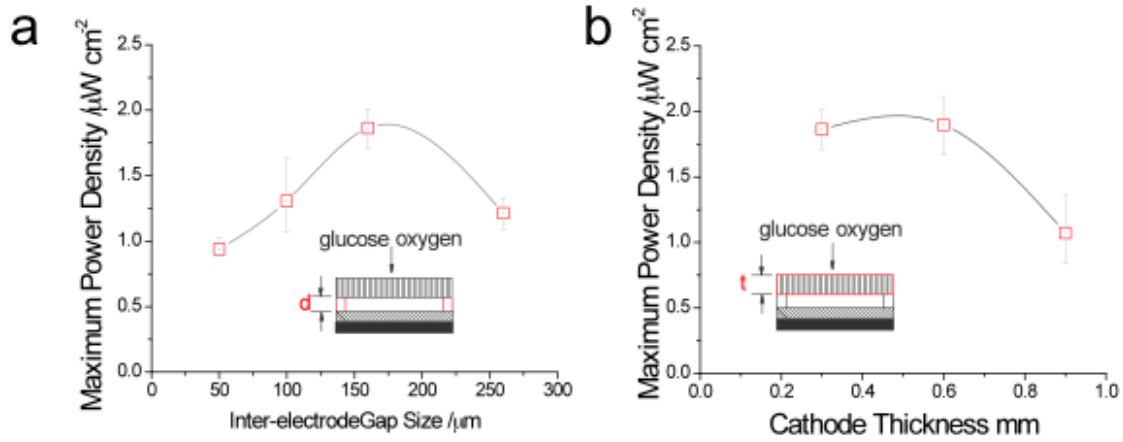

Figure 3.7 Fuel cell optimization (a) Effect of inter-electrode gap and (b) effect of electrode thickness on maximum power density

The effect on cathode thickness on maximum power output is presented in Fig. 3.7b. The carbon paper used as a support for the platinum catalyst is 0.3mm thick. Different cathode thicknesses were obtained by stacking 2 and 3 platinum on carbon paper electrodes and binding them with silver epoxy. Results indicate that a double stacked cathode performs better than the single electrode one but a sharp decrease in performance occurs for the triple stacked cathode. Although more oxygen reacts at the cathode when the thickness is increased, the diffusion of glucose to the anode appears to become the limiting factor.

3.6.4 Comparison between different cathode supports

The performance of fuel cells with the cathode fabricated by sputtering platinum directly on a anodize aluminum oxide membrane was also measured. Fig. 3.8 shows the difference in power output between the two. It shows that everything else being identical during the fabrication, the carbon paper support gives a much better performance. The large difference in performance between the two can be explained by the much smaller cathode surface area obtained when a AAO membrane is used as cathode support. In addition, given that the membrane has a thickness of only 60μm, compared to 300μm for the carbon paper, it allows a larger amount of oxygen to diffuse through resulting in mixed-potential at the anode.

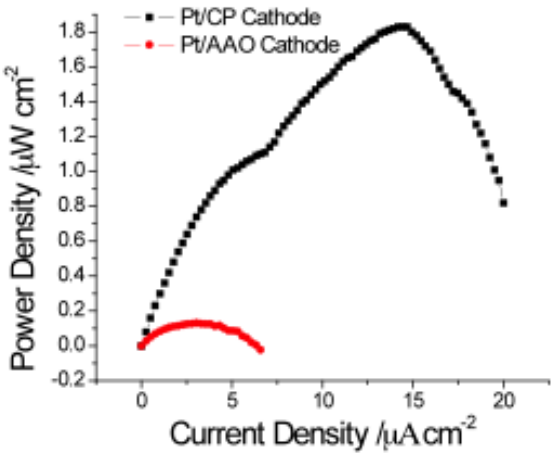

Figure 3.8 Effect of different cathode support layers. Comparison between carbon paper (CP) and anodized aluminum oxide (AAO) cathode supports on fuel cell power output

3.7 Conclusions

In this chapter we have demonstrated the possibility of micro- manufacturing enzyme-free glucose fuel cells without a filter membrane between the electrodes. This results in stacked fuel cells with lower ohmic resistance and better glucose diffusion to the anode. Compared to other designs the current fuel cell achieves much higher current densities. We also demonstrate the advantage of using a conductive support such as carbon paper since it reduces the amount of platinum required for producing high surface area electrodes. The performance of platinum on carbon paper supported electrodes is much better than that of electrodes produced in a similar manner on anodized aluminum oxide membranes because of the higher surface area of the carbon paper. In previous studies, in order to fabricate the cathode, either a hydrogel was used to support the catalyst materials (Kerzenmacher and Sumbharaju, 2007) or a silicon wafer with etched holes was used as a substrate for the deposition of the cathodic layer(Kerzenmacher et al., 2011). The first method has the drawback of producing thick electrodes and having limited stability against hydrolytic and oxidative attack while the latter approach requires numerous fabrication steps and a thick platinum catalyst layer for the formation of a high surface area Raney type catalyst layer. The carbon paper support allows for the fabrication of thinner and more stable electrodes which results in better glucose diffusivity through the cathode as indicated by the higher power density. It was shown that a peak

power density of 2 μW cm^{-2} occurs when the inter-electrode spacing is about 160μm. At large inter-elecrode spacing the peak power density is lower due to higher ohmic losses, while at smaller inter-electrode spacing the decrease in performance can be attributed to the change in concentration gradient at the anode as the gap size approaches the Nernst diffusion layer thickness. A small increase in performance was observed as the cathode thickness was increased from 300μm to 600μm but a sharp decrease was observed as the thickness was further increased. This shows that although a thicker electrode allows for better oxygen-glucose separation, the decrease in diffusivity of glucose to the anode becomes the limiting factor.

Chapter 4

High volumetric power density, non-enzymatic, glucose fuel cells[1]

4.1 Abstract

The development of new implantable medical devices has been limited in the past by slow advances in lithium battery technology. Non-enzymatic glucose fuel cells are promising replacement candidates for lithium batteries because of good long-term stability and adequate power density. The devices developed to date however use an "oxygen depletion design" whereby the electrodes are stacked on top of each other leading to low volumetric power density and complicated fabrication protocols. Here we have developed a novel single-layer fuel cell with good performance (2μW cm^{-2}) and stability that can be integrated directly as a coating layer on large implantable devices, or stacked to obtain a high volumetric power density (over 16μW cm^{-3}). This represents the first demonstration of a low volume non-enzymatic fuel cell stack with high power density, greatly increasing the range of applications for non-enzymatic glucose fuel cells.

[1] **Oncescu, V.**, Erickson D. "High volumetric power density, non-enzymatic, glucose fuel cells." *Scientific Reports* 3 (2013)

4.2 Introduction

Non-rechargeable lithium batteries have been successfully used in implantable medical devices for over 40 years, however their life cycle is often much shorter than the desired period of implantation for such devices (Vincent, 2000). For example, over 20% of the 200,000 annual pacemaker implants in the United States are performed in order to replace depleted batteries, whose lifetimes are limited to 5 to 7 years (Kurtz et al., 2010). This results in unnecessary infection risks, inconvenience to patients, and billions of dollars in costs to the health care system. In addition, due to advances in biosensors and low-power electronics, a host of new implantable systems such as pacing devices to prevent congestive heart failure, cochlear implants to treat profound deafness, and deep brain simulators to treat symptoms of Parkinson's disease have been proposed (Schmidt and Skarstad, 2001). Because such devices have higher power requirements than pacemakers and have a very short lifetimes when powered by current batteries (Wei and Grill, 2009), researchers are developing new implantable power sources that can harvest chemical, thermal and mechanical energy from the human body as an alternative to lithium batteries (Heller, 2006; Wei and Liu, 2008). These include piezoelectric (Khaligh et al., 2010; Qi and McAlpine, 2010) and thermal generators (Stark, 2006) and bio-fuel cells(Heller,

2004; Schröder, 2012). Glucose fuel cells are particularly interesting because of the abundance of oxygen and glucose in body tissue and the possibility to generate a stable high continuous power output through the coupling of the glucose oxidation and oxygen reduction reaction (Kerzenmacher et al., 2008a). In the past few decades most research in the field has been focused on immobilization methods for enzymatic catalysts in an effort to increase the lifetime of glucose fuel cells (Moehlenbrock and Minteer, 2008). Enzymatic catalysts for glucose/O_2 fuel cells have excellent selectivity and can produce power densities of the order of several $mWcm^{-2}$ however they have very short lifetime, typically less than 30 days, due to the fragile nature of the enzymes and poor immobilization techniques (Cinquin et al., 2010; Rengaraj et al., 2011). This makes them generally unsuitable for long-term implantable applications (Kim et al., 2006) despite having been successfully tested *in-vivo* (Halámková et al., 2012; Szczupak et al., 2012; Zebda et al., 2011).

Recently, there has been renewed interest in non-enzymatic fuel cells that use platinum alloys or activated carbon as catalysts (Kerzenmacher et al., 2008a). Such fuel cells have shown good time stability and have been successfully tested *in-vivo* (Drake et al., 1970; Sharma et al., 2011). The biggest challenge however remains the poor anode selectivity towards glucose oxidation in the presence of oxygen. Due to the lack of abiotic catalysts to selectively catalyze glucose

oxidation, several groups have developed fuel cell designs that reduce the access of oxygen to the anode. An oxygen depletion design that has been commonly used involves placing a porous cathode in front of the anode such that most of the oxygen gets reduced prior to reaching the anode allowing glucose oxidation to proceed at low oxygen concentrations. The design first presented by Rao *et al*. in the 1970s made used of hydrogels to separate the porous anode and cathode (Rao et al., 1976). Kerzenmacher *et al* also used hydrogels as binder for the catalytic materials at the anode and cathode (Kerzenmacher et al., 2008b). More recent designs however have avoided the use of hydrogels and instead used porous membranes such as carbon paper or anodized aluminum membranes, as supports for the cathode catalyst. In a previous paper, we demonstrated that such fuel cells can be assembled without a separation membrane in order to improve glucose diffusion to the anode and reduce the thickness of the fuel cell (Oncescu and Erickson, 2011). Although a promising approach, such oxygen depletion designs still require a large volume due to the thickness of each stacked electrode and the inter-electrode space, in addition to complicated fabrication and assembly protocols. The power density for such fuel cells is commonly reported in terms of electrode surface area exposed to interstitial fluid instead of volume as is often the case for other power sources. For example, most depletion design fuel cells described in literature have *in-vitro* power densities

ranging from 2μWcm^{-2} to 4.4 μWcm^{-2}, however the assembled devices require volumes of over 2 cm^3 because of the need to hold the stacked electrodes together (Kerzenmacher et al., 2011). This results in volumetric power fuel cell densities of less than 2 μWcm^{-3}, which makes them inefficient compared to piezoelectric and thermal generators that have fundamental power density limits of 30 μWcm^{-3} and10 μWcm^{-3} (Mitcheson, 2010) respectively. In order to address the issue, Kloke *et al*. has recently investigated a single layer design for glucose fuel cells by placing the anode and cathode side by side (Kloke et al., 2011). As noted there, a single layer design is desirable because of simplified fabrication, reduced thickness and facilitated implementation of the fuel cell in implantable devices. Although it was demonstrated that such single layer fuel cells can produce excellent power output (2.2 μW cm^{-2}), their fabrication required over 50μm platinum sheets and no attempt was made at integrating them in high power density fuel cell units.

Here we demonstrate how the single layer design can be manufactured cost-efficiently on single wafers using standard fabrication protocols and integrated in both high surface area and low volume implantable devices. We start by presenting the fabrication protocol for the low-platinum single layer fuel cell (SLFC), followed by polarization curves for both electrodes in order to understand the limiting reactions and the effect of changes in reactant

concentration on fuel cell performance. We then demonstrate how SLFCs can be designed to reduce mixed potential effects when used as coating layers for implantable devices. Finally we show how we can stack SLFCs to produce high power density fuel cell units.

4.3 Results

4.3.1 SLFC fabrication and characterization

The single-layer fuel cells (SLFCs) developed here are patterned directly on 500µm thick fused silica substrates (Fig. 4.1a) and subsequently diced to obtain 1cm^2 fuel cell layers. A concentric design where the anode is surrounded by the cathode was selected because, as will become apparent in the next sections, it increases the interface area between the electrodes and it helps increase glucose-oxygen separation when the layers are stacked. In order to achieve high effective surface area, a Raney-type alloy process is used for both the anode and the cathode. This process, first demonstrated by Gebhardt *et al.*, involves the annealing of a thin layer of platinum with a non-noble metal followed by the chemical etching of the non-alloyed outer metal layer. In this chapter nickel is used as the non-noble metal at the anode and aluminum at the cathode (Rao et al., 1976). We use a Ni/Pt alloy as anode for glucose oxidation because it has been shown elsewhere to exhibit greater selectivity towards glucose than other abiotic

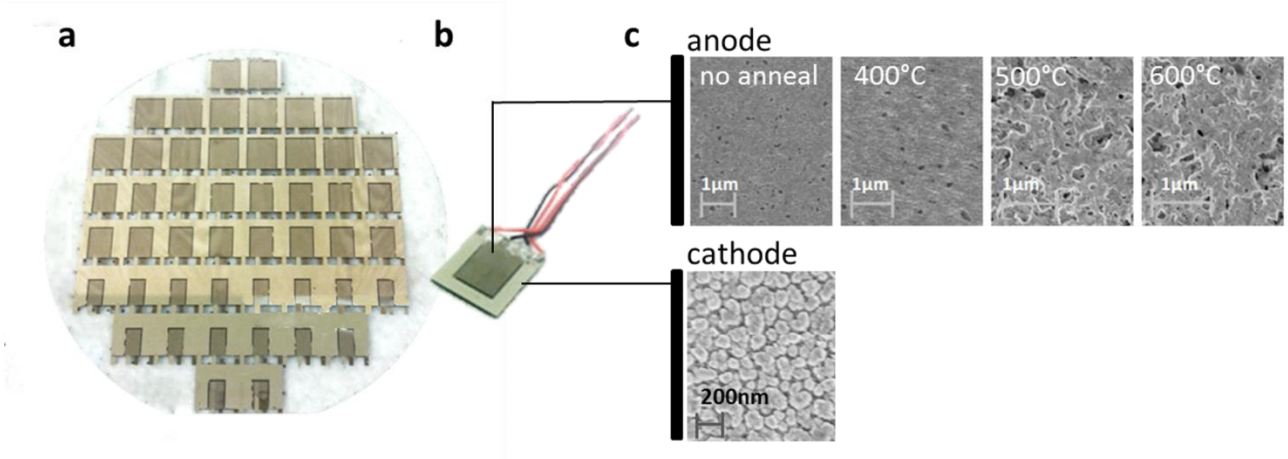

Figure 4.1 Single layer fuel cell devices. (a) fused silica substrate before dicing with single layer fuel cells (SLFC) patterned on both sides (b) a typical device used in this work with leads attached (c) scanning electron microscopic (SEM) images showing the high surface area Raney-alloy structure of the anode at different alloying temperatures and at the cathode.

catalysts (Kerzenmacher et al., 2008a). The electrodes in the SLFCs presented here use only 100nm of platinum, significantly less than in other works where metals such as zinc or nickel were electroplated on 50μm thick platinum foils (Kerzenmacher et al., 2010b; Kloke et al., 2011). The main issue with using such thin layers of platinum is that the electrode roughness that can be obtained using a Raney process is significantly lower resulting is smaller electrode surface area. Experiments with several anneal temperatures in the range 400°C -600°C have demonstrated that the roughness that can be obtained using a Raney-type process in the case of 100nm Pt / 300nm Ni peaks when the annealing temperature reaches 500°C. For the cathode, a high surface area platinum surface was obtained by annealing 100nm Pt/ 100nm Al at a low-temperature of 300°C and subsequently etching the aluminum with NaOH. X-ray photoelectron spectroscopy (XPS) analysis was used to determine the metal composition at the anode surface before and after etching to ensure that no un-alloyed nickel was left behind. The roughness of the electrodes is apparent from scanning electrode microscopic (SEM) images (Fig. 4.1c) and has been quantified using a cyclic voltammetry method. By estimating the charge under the hydrogen adsorption peaks in the cyclic voltammograms during cleaning of the samples, the roughness factor (RF) of the Raney-type Ni/Pt anode annealed at 500°C was determined to be 238±15. This is significantly higher than the RF of commercially

available platinum foils (30±4) but an order of magnitude lower than the RF values reported by Gebhardt *et al.* for 50μm thick Ni/Pt Raney films (RF~2000)[30].

4.3.2 SLFC electrode characterization

The polarization curves of the anode and cathode in SLFCs provide useful information as to the limiting reactions of the fuel cell and the effect of variations in glucose and oxygen concentration. Fig. 4.2a shows the polarization curves for the Pt/Al cathode at different oxygen and glucose concentrations. Two flow meters (0.2–2 SCFH) were used to adjust the ratio of air and nitrogen flowing in the 0.1M PBS solution and the temperature was maintained at 37°C. It can be seen that at low oxygen concentrations (7% O_2 saturation) there are two distinct regions to the polarization curve, a linear ohmic region from 0 to 10 μAcm^{-2} and a transport-limited region above 10 μAcm^{-2}. In the linear ohmic region the drop in voltage is due mainly to resistance in the electrolyte while in the transport-limited region the voltage drop is due to low oxygen concentration near the electrode surface. At high oxygen concentration (21% O_2 saturation) no transport limited-region is observed under 30μAcm^{-2}. The effect of glucose on the cathode is relatively small with voltage drops of less than 20mV at current densities in the range 0 to 30μAcm^{-2} indicating that the Pt/Al alloy selectively catalyzes oxygen reduction in the presence of glucose. The electrode specific resistance in the

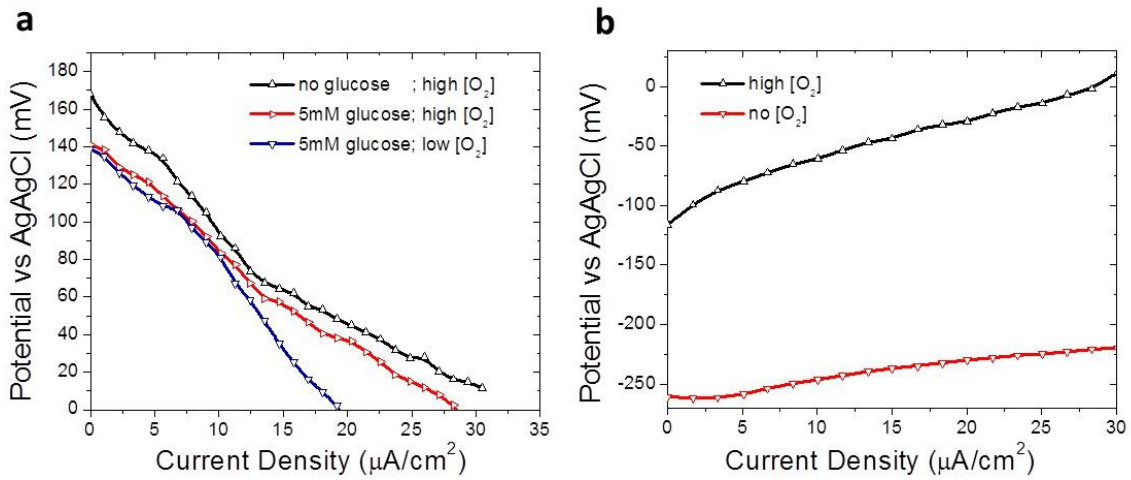

Figure 4.2 Electrode polarization curves. (a) cathode *i*-V curves showing the effect of 5mM glucose in solution and the effect of low oxygen partial pressure (7% oxygen saturation) (b) anode *i*-V curves at high (21% saturation) and low (2% oxygen saturation) oxygen partial pressure. The results represent the average of 3 measurements.

linear regime is given by $R = \Delta U/\Delta j = 6.69\ k\Omega cm^{-2}$. The cathode open circuit potential versus the Ag/AgCl reference electrode is comparable to what was previously reported by Kerzenmacher *et al*. for Raney-type Pt/Al alloys (Kerzenmacher et al., 2010a).

For the Pt/Ni anode the polarization curves in Fig. 4.2b show that the potential is significantly lowered by the presence of oxygen, however because glucose is present in high concentrations in interstitial fluid, there is no transport limited region in the 0 to $30\mu Acm^{-2}$ range. The electrode specific resistance increases from 1.31 $k\Omega cm^{-2}$ when only nitrogen flows in solution (2% O_2 saturation) to 3.21 $k\Omega cm^{-2}$ when only air flows in solution (21% O_2 saturation). The polarization curves presented in this section indicate that in a SLFC the polarization of the cell voltage is dominated by resistance at the cathode even when the oxygen partial pressure is above physiological levels. It can also be seen that a decrease in oxygen has a mixed effect on the polarization curve of the fuel cell since it decreases the resistance at the anode but creates mass transport limited effects at the cathode.

4.3.3 SLFCs as coating layers to implantable devices

SLFCs are attractive because they can be integrated directly as coating layers for implantable devices. However, as the polarization curve for the anode indicates,

the presence of oxygen can significantly reduce the performance of the anode. In addition, we observed from electrode polarization curves that for the cathode at low oxygen partial pressure there is a limiting current density above which the oxygen reduction reaction becomes transport limited. To address this, we have developed several designs that minimize these oxygen and transport limiting effects. First we look at the effect of varying the cathode to anode area ratio (denoted as $n = A_{cathode}/A_{anode}$) in order to determine the optimal configuration such that the fuel cell is not limited by oxygen transport at the cathode. From Fig. 4.3a we observe that at high oxygen partial pressures the maximum current density drawn from the fuel cell increases with increasing n. A peak power output of 1.21μWcm^{-2} is observed for SLFCs with n=3.7, a 50% increase over SLFCs with n=0.47, indicating that it's beneficial to have a larger cathode surface area. This is expected since, as mentioned in the previous section, the polarization of the cell voltage is mainly driven by resistance at the cathode. In addition, at low oxygen partial pressure we expect the advantage of a lager cathode area to be even more accentuated due to higher electrode specific resistance at the cathode in the transport-limited regime.

Using a similar approach to the above, we can also demonstrate how SLFC designs with high interface area between the electrodes can minimize mixed potential effects at the anode and improve the performance of the fuel cell. We

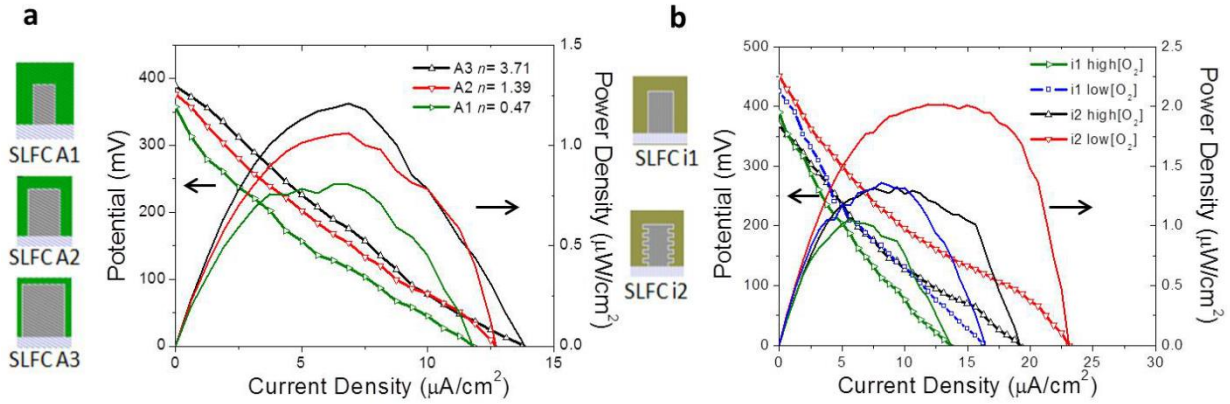

Figure 4.3 SLFC as coating layers (a) SLFCs used to test the effect n $=A_{cathode}/A_{anode}$ on fuel cell performance (here for SLFC A1 n=3.7, SLFC A2 n=1.39, SLFC A3 n=0.47) (b) interdigital electrode fuel cells used to test the effect of interface area and oxygen concentration on fuel cell performance. The results represent the average of 3 measurements.

achieve this by having an interdigital interface, or comb-like interface, between the anode and the cathode as can be seen in Fig. 4.3b. Interdigital electrodes have been demonstrated before for electrochemical sensors (Van Gerwen et al., 1998), however our approach is the first implementation for non-enzymatic glucose fuel cells. Here the electrodes are separated by 500μm and the aim of the electrode pattern is to increase the area of oxygen depletion over the anode and decrease the ohmic resistance between the electrodes. Since oxygen consumption is proportional to the current drawn from the fuel cell, the effect of oxygen depletion at the anode gets more significant when the fuel cell operates at high current densities. Fig. 4.3b shows that the interdigital designs increases the peak power output of the SLFC from 1.05 μWcm^{-2} to just over 1.32 μWcm^{-2}. The reported peak power output represents the average of 3 different experiments with sample standard deviation of ±0.09 μWcm^{-2} for the interdigital design and ±0.12 μWcm^{-2} the non-interdigital design. The experiments described above were performed at high oxygen partial pressure (21% oxygen saturation) in order to avoid any experimental errors due to the flow of nitrogen in solution which is hard to control accurately. In another experiment, we lowered the oxygen concentration by increasing the flow of nitrogen in solution (7% oxygen saturation) and observed a large increase in power output for both interdigital and non-interdigital designs. This trend is consistent with our observations from

the anode polarization curves that predict a decrease in anode potential at lower oxygen concentrations. A similar increase in fuel cell performance was observed by Sharma *et al* when the fuel cells were tested *in-vivo* at lower oxygen partial pressure (Sharma et al., 2011). As shown in Fig. 4.3b the interdigital SLFC has a peak performance of approximately 2.01μWcm^{-2} at low oxygen partial pressure, compared to 1.36μWcm^{-2} for the non-interdigital SLFC. The improvement in peak power output is more significant in the interdigital case (52.3% increase compared to 29.3%) likely due to increased oxygen depletion over the anode. As was previously reported, a change in oxygen concentration at the anode surface has greater effect on fuel cell performance at lower oxygen partial pressures (Oncescu and Erickson, 2011). The peak power changes in this experiment are therefore consistent with that observation. In addition, the reduced ionic resistance between the anode and the cathode due to the high interface area also contributes to the increased performance of the interdigital design.

4.3.4 SLFCs in stacked configuration

The greatest advantage of SLFCs over other non-enzymatic glucose fuel cells designs is that they can be integrated in very compact fuel cell units for volume sensitive implantable devices. As discussed previously, the glucose fuel cells developed so far have been intended to be used as coating layers for implantable

devices since their thickness and complicated stacked design makes them unsuitable for low volume applications. The SLFCs developed here, not only can be easily stacked, but doing so greatly increases their performance. Stacking the SLFC can reduce the amount of oxygen reaching the anode, as illustrated in Fig. 4.4a, because only a small volume of interstitial fluid is allowed to diffuse through the sides and between the fuel cell layers. Fig. 4.4b shows the effect of stacking on the overall performance of a SLFC. The gap δ between the SLFCs determines the amount of reactants that that can diffuse through the sides of the stacked fuel cell unit and over the electrodes. Using this approach some of the oxygen in solution reacts at the cathode before it diffuses to the anode allowing glucose oxidation to proceed at low oxygen concentrations as illustrated in Fig. 4.4a. As discussed previously, some of the glucose reacts at the Pt/Al cathode, however the effect on the stacked SLFC's performance is small because of the large difference in oxygen and glucose physiological concentration. In interstitial tissue, the glucose concentration is approximately 5 mmol L^{-1} while that of oxygen is less than 0.2 mmol L^{-1}. Decreasing the gap δ between the fuel cell layers can increase the peak power output of the SLFC. It can be seen in Fig. 4.4b that the increase can result in over 2 fold increase in power output per SLFC over the case where there is no stacking. For a SLFC A1 type fuel cell, a peak power

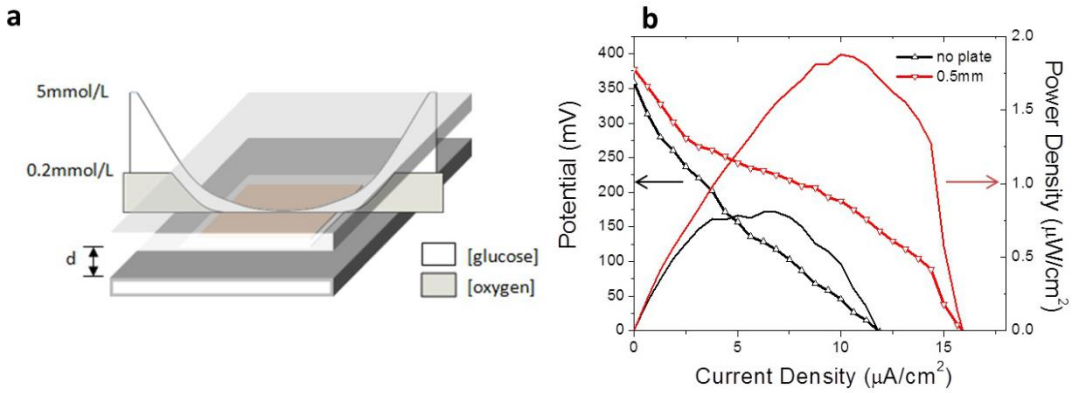

Figure 4.4 SLFC in stacked configuration (a) illustration demonstrating how confining the reactants diffusion can reduce the amount of oxygen at the anode (b) confined diffusion effect on fuel cell performance showing the increase in SLFC A1 performance when there is plate 0.5mm above the SLFC. The results represent the average of 3 measurements.

output of 1.88μW/cm² is obtained when δ is 0.5 mm. Although the fuel cell layers could potentially be stacked event closer together (δ≤0.5mm), this is not easily achievable for the current design, because of the thickness of the wires that were used as electrode connections. The experiments were performed at 37° in 0.1M PBS solution with physiological levels of glucose (5 mmol L^{-1}) and dissolved oxygen in solution (0.2 mmol L^{-1}).

4.3.5 Integrated fuel cell unit

In order to demonstrate the potential of SLFCs to be integrated in implantable devices as highly compact power sources we have assembled a fuel cell unit with stacked SLFCs connected externally in parallel. The holder was printed using a 3D printer. The assembled device in Fig. 4.5a has a volume of approximately 1cm^3 and can accommodate 12 SLFCs printed on both sides of 1cm by 1cm diced pieces of 500μm thick fused silica wafers. That represents 12cm^2 of fuel cell surface area exposed to solution. For comparison purposes an oxygen depletion design type fuel cell that we have previously developed(Oncescu and Erickson, 2011) had a thickness of 0.5cm, a total volume of 2 cm^3 and a surface area of 1cm^2 exposed to solution. The fuel cell had a power output of 2 μWcm^{-2} corresponding to a volumetric power output of roughly 1μWcm^{-3}. Fig. 4.5b shows the cell

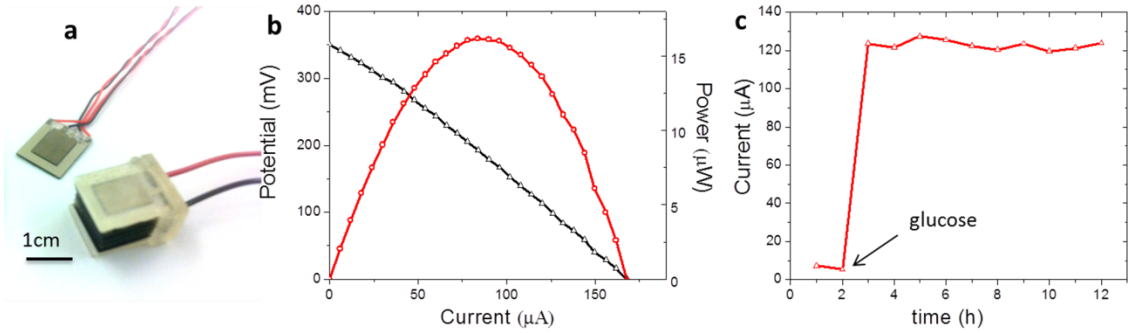

Figure 4.5 Confined Diffusion effect on performance (a) picture of one double sided SLFC along with a stack of 12SLFCs (b) performance of the 12 SLFCs stack connected in parallel (c) chronoamperometric response at 0.1V in 0.01M PBS solution for the first 2h and after the addition of 5×10^{-3}molL^{-1} glucose.

potential and power density versus current density for the stacked fuel cell unit in Fig. 4.5a. It can be seen that the peak volumetric power output is 16μWcm^{-3} roughly 16 times higher than for the depletion design type fuel cell. The sweep rate used here is 18μA h^{-1}. The performance is lower than the expected peak performance of 12 SLFCs connected in parallel, because of resistance losses in external SLFC connections.

Chronoamperometric experiments were also performed to demonstrate the long-term stability of the fuel cell unit. Fig. 4.5c shows the chronoamperometric response at 100mV over a period of 12 hours. For the first 2 hours the fuel cells was kept in 0.01M PBS solution after which 5mM glucose was added to the solution. It can be seen that a stable current output of 123μA was obtained following the addition of glucose and less than ±10% fluctuation was observed during the entire period. In addition, this stable current output at 100mV is consistent with the data presented for the polarization curve in Fig. 4.5b demonstrating that a sweep rate of 18μA h^{-1}did not lead to an overestimation of the performance

4.4 Discussion

The results presented in this chapter demonstrate the potential of SLFCs to be integrated as high-performance low-cost glucose power sources in implantable

devices. Unlike other non-enzymatic fuel cells proposed previously, the SLFCs are thin and easy to fabricate and assembled using standard semiconductor processing technology. In addition, each electrode is fabricated using 100nm evaporated platinum, which is significantly less than in other designs where 50μm thick platinum foils were used for fabricating Raney-type Pt/Zn alloys (Kerzenmacher et al., 2010b). Here, it was demonstrated that an inter-digital type SLFC can achieve up to 2.01μWcm^{-2} peak power output at physiological levels of glucose and oxygen and that a stacked fuel cell unit of 12 SLFCs can provide a volumetric power output of at least 16μWcm^{-3}. It is important to note that here the performance is measured in terms of SLFC area which includes both patterned electrodes. The state-of-the-art depletion design fuel cells quote a power output of 2 to 4.4 μWcm^{-2} per area exposed to the solution, which is just the geometrical surface area of the cathode (Kerzenmacher et al., 2008b; Oncescu and Erickson, 2011) and does not take into account the thickness of the assembled fuel cell. In depletion design fuel cells the cathode is placed on top of the anode resulting in complicated assembly which makes them unsuitable for stacking and low volume applications. This makes such fuel cells hard to compare on volumetric power output basis with the SLFCs presented in this chapter. The single layer fuel cell presented by Kloke *et al*. has a peak power output of 2.2 $\mu W\ cm^{-2}$ however it is not fabricated on a single substrate and has

not been integrated in high power density fuel cell units as is the case in this chapter (Kloke et al., 2011). The performance of the SLFCs can be improved further by developing more selective anodic catalysts (Kerzenmacher et al., 2008a) or by increasing the surface area of the electrodes in the current design. Kloke *et al.* has recently demonstrated that a Raney-type platinum zinc catalyst obtained from 50μm thick platinum foils and 30μm thick layer of zinc can have an open circuit voltage of -400mV, significantly lower than the anode we presented here (Kloke et al., 2011). In addition surface area of the electrodes can be increased by immobilizing carbon nanotubes onto the fused silica wafer before electrode patterning. Carbon nanotubes have been used for a long time to increase the area of enzymatic fuel cells (Davis et al., 1997). Some groups have developed and characterized electrodes with embedded multiwall carbon nanotubes (Prilutsky et al., 2010) but have yet to be implemented in non-enzymatic glucose fuel cell systems.

4.5 Methods

4.5.1 Fabrication

The fabrications steps for the fuel cells described here were performed at the Cornell Nanofabrication Facility. 500μm thick fused silica wafers were used due to the fact that electrode can be patterned directly on them without the need of

depositing a silicon oxide layer. The electrodes were patterned one at a time using a LOR lift-off process. First the anode was patterned using E-beam evaporation (CHA Evaporator) where 20nm of titanium was deposited in order to promote adhesion followed by 100nm of platinum and 300nm of nickel. The wafer was subsequently annealed for 2 hours in nitrogen gas at 600°C (MRL Industries Furnace). In order to avoid oxide formation when opening and closing the furnace door, the stand-by temperature of the furnace was kept bellow 300°C. In order to obtain a high surface area Raney-type surface the nickel was etched by keeping the wafers in a 1:1 solution of concentrated sulfuric acid and nitric acid for 12 h. The cathode was patterned using E-beam evaporation of 20nm of titanium followed by 100nm of platinum and 100nm aluminum. The wafer was subsequently annealed for 1 hour in nitrogen gas at 300°C followed by the etching the aluminum in 0.1M NaOH solution. The fused silica wafers were then diced (K&S 7100 Dicing Saw) into 10mm by 12mm pieces. Copper wires (30 gauge) were soldered directly onto the electrodes.

4.5.2 Cleaning and activation

After dicing the fuel cells were cleaned under oxygen plasma for 10min to remove any resist residue at the surface. Both electrodes are than subject to cyclic voltammetry in 0.5M sulfuric acid solution for 10 cycles at $50mVs^{-1}$. Following a method previously described by Kerzenmacher *et al.* the cathodes were subjected for 30min to an oxidative current density of $44\mu Acm^{-2}$ in 0.01M phosphate buffer

saline solution (Sigma P-5368 0.138M NaCl) with pH 7.4 at 7% oxygen saturation without glucose.

4.5.3 Experimental setup and conditions

The experimental setup used in this chapter has been previously described by the authors elsewhere (Oncescu and Erickson, 2011). All experiments were performed in 500mL 0.01M PBS solution (pH 7.4) at 37°C. When specified, glucose was added at physiological levels of 5 mmol L^{-1}. The solution was replaced after each experiment to ensure low contamination. Two flow meters (VWR 0.2–20 SCFM) were used to adjust the ratio of air and nitrogen (Airgas NI-200) flowing in the solution. In most experiments air was constantly being bubbled through at 0.2SCFH to ensure that the oxygen levels remained constant throughout the experiment. The measured dissolved oxygen saturation level was (21±0.5)%. Where specified 0.6SCFH nitrogen gas was mixed with the air in order to decrease the oxygen concentration in solution. The corresponding dissolved oxygen level was measured to (7±0.5)% saturation corresponding to the upper physiological oxygen saturation level (7% or about 0.06 mM) (Kerzenmacher et al., 2010b). The dissolved oxygen measurements were performed using a Dissolved Oxygen Pen (850045 Sper Scientific). The solution was stirred for 3 hours prior to performing current sweep experiments in order to improve glucose mixing in the solution, however it was not stirred during the experiments.

4.5.4 Instrumentation

A Keithley 2400 Source-meter was used to apply a current sweep across the fuel cells and a Keithley 2000 Multi-meter equipped with a scanner card was used to take the voltage measurements of individual electrode potentials versus the reference electrode. The current sweep and channel switching was remotely controlled using a LABVIEW program. All current sweeps were performed at a sweep rate of 18μA h^{-1}, starting 0μA and increasing the current by 0.5μA every 100s. A silver–silver chloride reference (Aldrich Double junction Ag/AgCl reference) electrode was used as the reference against which electrode potentials were measured.

Chapter 5

Smartphone health accessory for colorimetric detection of biomarkers in sweat and saliva[1]

5.1 Abstract

The mobile health market is rapidly expanding and portable diagnostics tools offer an opportunity to decrease costs and increase the availability of healthcare. Here we present a smartphone based accessory and method for the rapid colorimetric detection of pH in sweat and saliva. Sweat pH can be correlated to sodium concentration and sweat rate in order to indicate to users the proper time to hydrate during physical exercise and avoid the risk of muscle cramps. Salivary pH below a critical threshold is correlated with enamel decalcification, an acidic breakdown of calcium in the teeth. We conduct a number of human trials with the device on a treadmill to demonstrate the ability to monitor changes in sweat pH due to exercise and electrolyte intake and predict optimal hydration. Additionally, we perform trials to measure salivary pH over time to monitor the effects of diet on oral health risks.

---

[1]**Oncescu, V**.*, O'Dell, D.*, Erickson, D., "Smartphone based health accessory for colorimetric detection of biomarkers in sweat and saliva" *Lab-on-a-Chip* (2013 Accepted)
*These authors have contributed equally to this paper.

5.2 Introduction

The cost of healthcare in the U.S. projected to reach 30% of the GDP by 2040 (Fogel, 2009). The widespread adoption of smartphones among nearly all age and income groups presents an opportunity for the development of mobile health applications and accessories for these devices that can help reduce costs and improve the accessibility of healthcare. Over 40,000 mobile health applications (commonly referred to as "apps") are currently available and that number is expanding rapidly (Fox and Duggan, 2010). A number of consumer mobile health accessories that integrate with smartphones such as Nike FuelBand, Fitbit One, and Misfit Shine combine accelerometers, heart rate monitors, and data on oxygen consumption to give users information on physical activity and daily calorie expenditure. Despite the amazing pace of developments in mobile health technologies, however, the vast majority of devices on the market focus exclusively on these physical measurements.

A high-impact area for mobile health, that has not yet taken off commercially, is in the development of biochemical portable diagnostics tools (Martinez et al., 2010). Smartphone accessories for the detection of biomarkers in bodily fluids could greatly reduce the cost of medical testing and increase global access to healthcare. Several academic groups are currently developing smartphone platforms for biomarker detection. Recently, Coskun *et al.* have developed a testing platform that can be used at home to test foods for peanut traces and other common allergens (Coskun et al., 2013b). Several other groups are working

on smartphone-based image processing for quantifying colorimetric changes on paper-based immunoassays (Shen et al., 2012).

In this chapter, we demonstrate an integrated smartphone accessory for monitoring changes in sweat and salivary pH. In addition, numerous academic publications have also studied the relationship between pH and various physiological conditions. For example, salivary pH is an important factor on enamel decalcification (Dawes, 2003; West et al., 2008) and sweat pH can be used to indicate the risk of dehydration (Morgan et al., 2004).

The smartphone accessory presented here has an integrated design that allows noninvasive real-time analysis using disposable test strips. In this chapter, we first introduce the system and how it integrates with existing smartphones. Second, we describe the software for colorimetric detection and the method through which we ensure uniform repeatable results on different smartphones. Finally, in the results section, we show the applicability of our system to sweat and saliva biomarker detection through a series of human trials. We demonstrate that our system can be used in the context of sweat testing in order to prevent the risk of dehydration and to improve performance during physical activity and in the context of saliva testing can be used to evaluate the impact of diet changes on oral health.

5.3 Methods

5.3.1 Overview of the system

The system presented here consists of a smartphone case, application, and test strips. The case has a slot in which a test strip can be inserted for colorimetric analysis using the cellphone camera and a space to store up to 6 additional test strips. Fig. 5.1 shows a user removing a test strip from the storage space, collecting a sweat or saliva sample, and inserting the test strip in the device for analysis. The test strips incorporate 3 different elements inserted in a 3D printed support: an indicator strip, a reference strip and a flash diffuser. As an initial application presented here, we have designed the test strips in order to measure pH differences in sweat and saliva. The indicator strip consist of a 9 mm by 4 mm cutout of a pHydrion Spectral 5.0 to 9.0 plastic pH indicator strip for sweat testing and a 1.0 to 14.0 strip for saliva testing. The reference strip is made of white plastic material and is used in order to detect changes in white balance on the iPhone camera due to different light conditions or user error. The flash diffuser consists of a 2 mm thick membrane of polydimethylsiloxane(PDMS). The purpose of the flash diffuser is to reduce variations in the reading for different lighting conditions and will be explained in the calibration section of this chapter. It allows light from the smartphone's flash to diffuse and illuminate the back of the tests strip uniformly. In addition, the case is 3D printed using opaque Vera black material in order to isolate the test strip from variable external light.

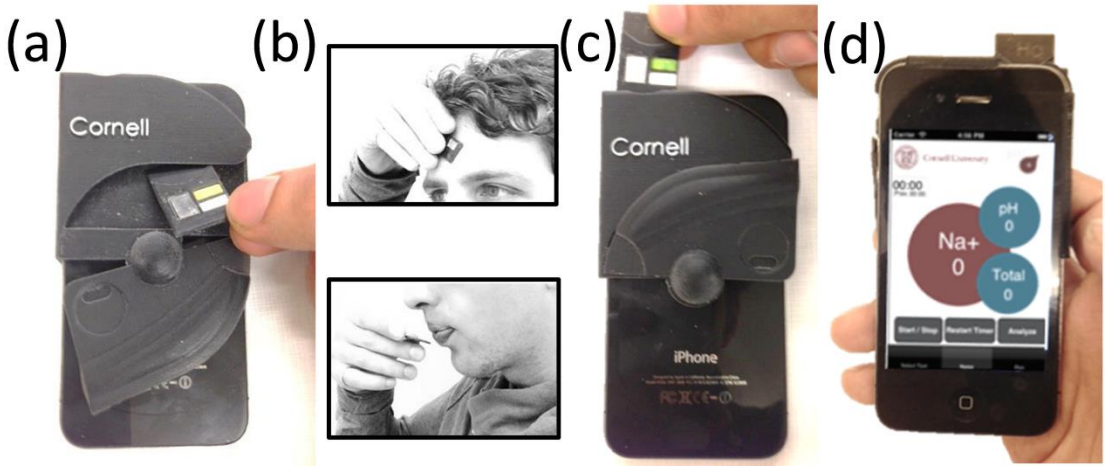

Figure 5.1 System for colorimetric quantification of biomarkers in sweat and saliva a) Picture of the device with the user removing a test strip from the back storage compartment. b) Sweat sample acquisition by application of the test strip on the forehead or saliva sample acquisition by user spitting on the test strip. c) Insertion of the test strip in the optical system for reading. d) Analysis of the pH once the test strip is inserted using the iPhone app.

5.3.2 Smartphone application

To work with the accessory, we have developed a software app to handle image acquisition and processing, and data storage and manipulation. The app shown in Fig. 5.2 works as follows. First, upon loading the app, the user selects the test strip being used from a menu of different biomarker tests available, and the app loads the appropriate calibration data and user interface. Secondly, the user inserts the disposable test strip cartridge into the hardware accessory and touches the "Analyze" function on-screen. Thirdly, the app turns on the camera flash and takes an image of the test strip. The quantitative biomarker concentration is determined from the image (see "Colorimetric quantification" section) and displayed on screen in under five seconds. If pertinent to the specific biomarker, additional post-processing is also done from the biomarker results, and these results are displayed alongside the biomarker concentration. Finally, by swiping left, a scatter plot of the results is generated to show trends over time. If desired, the data set can also be sent via email for later viewing or additional analysis.

5.3.3. Colorimetric quantification

Although the ubiquity of smartphones with high-quality integrated cameras make such devices ideal for point-of-care biomarker detection, the wide range of

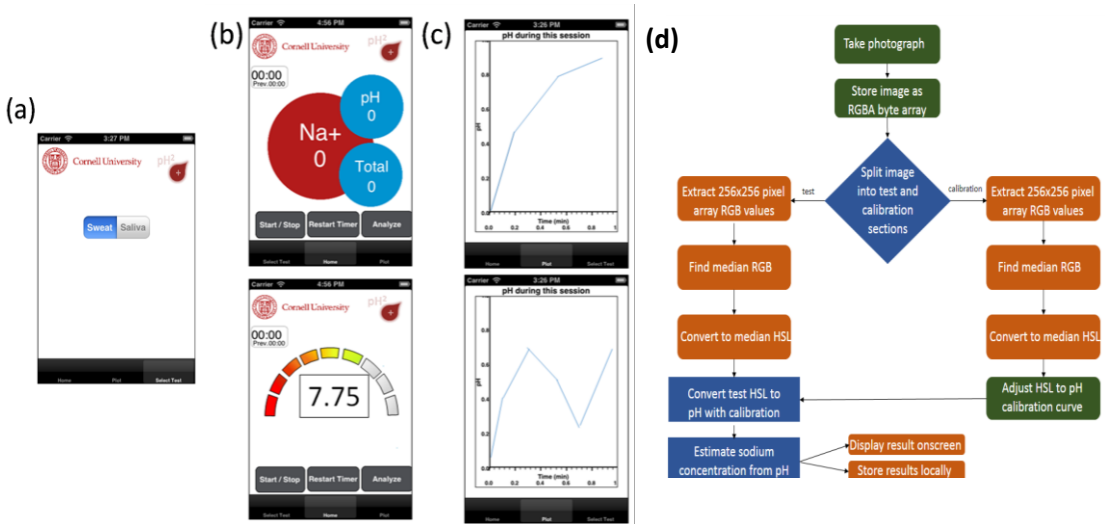

Figure 5.2 App and algorithm for quantification of biomarkers. An overview of the modular smartphone app and its operation. a) The user selects the desired test strip from a menu of pre-calibrated test options. b) The app automates the process of image acquisition and processing for the desired application. The top image shows the sweat pH and electrolyte interface; the bottom, the salivary monitoring interface. c) A plot of the data is produced to demonstrate trends over time. (d) A schematic overview of the image acquisition and processing algorithm.

variations across different devices and of test strip illumination present significant challenges to accurate colorimetric quantification. Other investigators have addressed this problem by calibrating for ambient light conditions through conversion to color spaces which are less sensitive to changes in brightness[5, 9]. On its own, this approach still requires uniform external illumination, and false colorimetric readings can be made if the phone is not placed at the proper distance from the test strip (Shen et al., 2012). One of the unique opportunities of smartphone-based colorimetric detection for portable diagnostics, however, is that image acquisition can instead be automated, so that the test strip is always held in the ideal position and imaged in the same manner, and the data is not easily affected by deviations in user protocol. Our device is isolated from ambient light with the hardware accessory and diffuses light from the smartphone camera flash for reproducible and uniform illumination, improving measurement accuracy and minimizing the potential for user error (see "Calibration" for details).

While the use of the camera flash instead of external light removes much of the variability from the image acquisition, there are additional steps which must be taken for accurate quantitative processing. Although the image from the smartphone camera is initially defined with RGB (red green blue) values, individual red, green, and blue channels do not correlate well with pH over the

range of a universal indicator strip. Nevertheless, the RGB values can be readily converted to an alternate color space that matches the color spectrum of the test strips more closely. We chose to convert to hue, which unlike RGB was found to monotonically increase with pH in our experiments over the entire range of the colorimetric test strips used. This advantage of the hue value over RGB for smartphone-based colorimetric imaging has also been recently demonstrated by Chang (Chang, 2012). In addition, recent work by Cantrell *et al.* has also found hue to be more precise than RGB values for quantitative analysis and less sensitive to variations in illumination, making it an ideal candidate for our colorimetric test strip analysis (Cantrell et al., 2010). After an initial calibration to determine the relationship between the hue and the analyte concentration for each test strip, this single hue value is sufficient to quantitatively specify the color with a high degree of accuracy.

The process of image analysis is as follows. When the "Analyze" button is pressed, the smartphone app activates the camera flash, and an image is captured and stored first as an RGBA (red green blue alpha) byte array. The alpha channel, which is a measure of transparency, is discarded as it does not vary with analyte concentration. The RGB array is split into two sections—the first, corresponding to the upper colorimetric test strip, and the second, to a lower reference region of known color value which is used to compensate for

variations between different smartphone cameras and from automated camera adjustment functions such as white balance. A 256 x 256 pixel square is selected from the center of each of these sections, and the hue value is calculated for each pixel from the RGB channels. The hue values are sorted, and the median value is chosen to minimize any remaining edge effects which are not removed by the PDMS flash diffuser. Because the color of the plastic reference section should not change between experiments if the device works correctly, the image acquisition process is restarted if the reference hue value varies from the expected calibration value by more than 5. This serves to eliminate the possibility of a user protocol error—if the test strip is inserted incorrectly and the strip is not optically isolated, the reference check will fail and the data will not be stored. If the reference check is passed, the test hue value is converted into an analyte concentration by means of a measured calibration curve and the relevant biological information is displayed on-screen immediately. A schematic of this process is given in Fig. 5.2d.

5.3.4 Calibration

The correlation between hue and pH is built into the application, allowing users to run tests without additional calibration. This is possible because the case is design in a way that minimizes the effect of external lighting as was previously

discussed. Fig. 5.3a illustrates the design of the case around the camera and flash that allows for uniform lighting of the test strip. By guiding the flash light through the PDMS diffuser on the strip and behind the test strip, we avoid the need to build in a lighting element, such as an LED, that would make the system bulkier and require power input. The strip is imaged at a distance of 2.20 mm from the smartphone's camera and the whole optical piece has a depth of 4.90 mm. The relationship between hue and pH for our test strips was established using buffer solutions and a pH electrode (VWR SympHony SB70P) for an 8 point calibration. Fig. 5.3b shows the variations in hue readings for 3 different iPhones (models 4 and 4S). The same test strip and holder were used at a given pH for all three iPhones meaning that the differences can be attributed directly to differences in the hardware of the iPhones. A third order polynomial was fitted through the data points in order to obtain a correlation between pH and hue. Fig. 5.3c shows the maximum deviation of the measured pH from the calibrated values. It was found that the variation between phones is the largest source of error, therefore defining the accuracy of the system over the range of physiologically relevant pH values to be within 0.2 pH units.

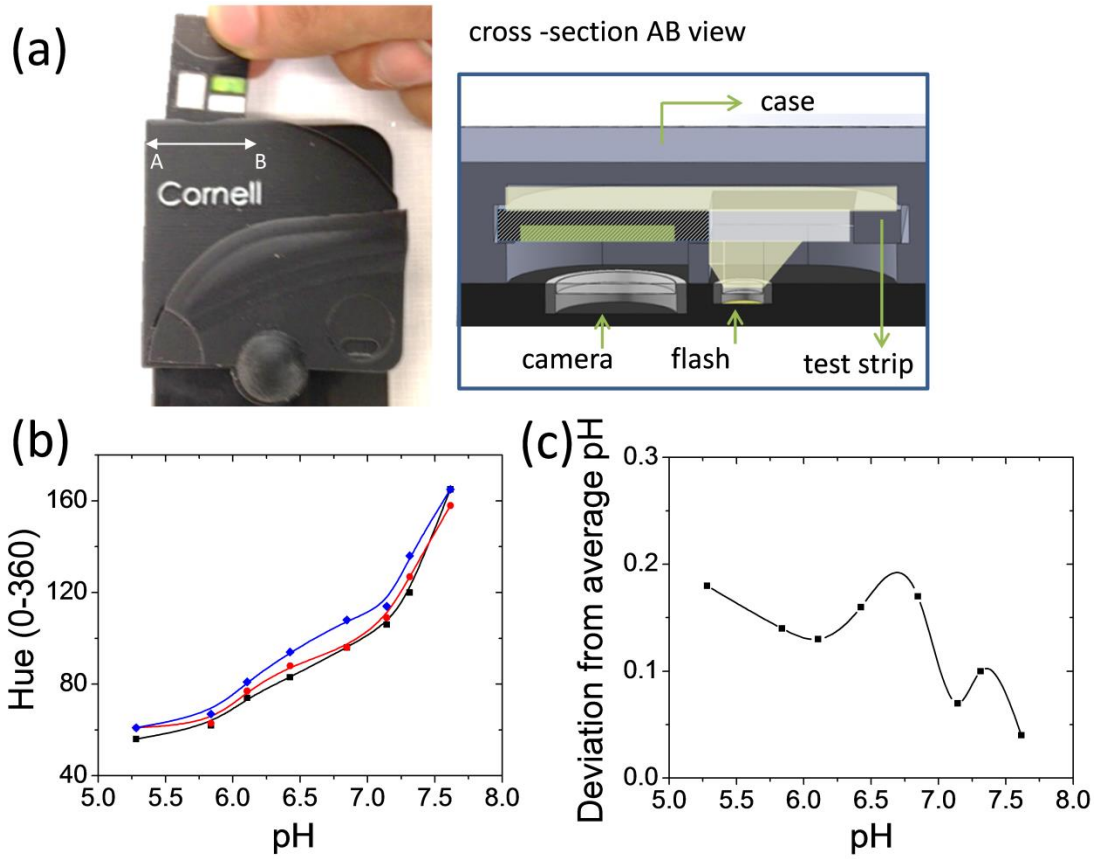

Figure 5.3 Smartphone accessory and application across different smartphones.

a) Test strip imaging with the first image showing the insertion of the test strip and the second one showing a cross sectional view of the optical system b)Hue-pH correlation for 3 different phones. c) Maximum deviations for three different iPhones from the measured calibration curve.

As explained previously, in order to further improve the accuracy of our system, we incorporate a white reference strip on our test strip. A large variation in the hue value of the white reference indicates a failed measurement, possibly from a faulty or incorrectly inserted test strip. If the application detects an abnormal hue value, it rejects the data point and signals to the user to take another reading.

Although the system shown here was designed for and prototyped on the iPhone 4 and 4s, it could easily be ported to any other smartphone platform with a CMOS camera. Even if there are systematic differences in camera function and sensitivity between smartphones from different manufacturers, these differences can be corrected by calibrating the hue-to-pH conversion function once for each smartphone model used. If the hardware accessory is re-designed to fit over the camera and properly re-calibrated, the most important metric for determining the accuracy of the device should still be the variation between several phones of the same model, as described above.

5.4 Results and Discussion

5.4.1 Sweat monitoring for hydration and electrolyte loss

It is generally well-accepted that dehydration can negatively impact performance during exercise (Murray, 2007), however over-hydrating is similarly dangerous since it can lead to hyponatremia, a disorder resulting from abnormally low sodium plasma concentrations (Murray et al., 2003; Rosner and Kirven, 2006).

Hyponatremia has resulted in deaths both in athletic competitions and on the battlefield(TP and DE, 1999), due to a disruption in the osmotic balance across the blood-brain barrier, resulting in a rapid influx of water into the brain. In addition, studies have shown the sodium concentration of sweat can be used to evaluate the risk muscle cramps in athletes (Eichner, 2007; Stofan et al., 2005). There is currently no system for accurately monitoring hydration levels or sweat sodium concentrations during exercise. However, there have been several studies showing the correlations between sweat pH and sodium concentration, as well as pH and sweat rate (Buono et al., 2007; Emrich et al., 1968; Patterson et al., 2000). Therefore, by accurately measuring changes in sweat pH during physical exercise, we can determine an optimal hydration strategy.

In a recent paper, Curto *et al* demonstrated continuous, smartphone-based sweat pH monitoring using a wearable microfluidic platform (Curto et al., 2012). A wearable colorimetric pH sensor that can be incorporated directly into clothing has some obvious benefits; there are, however, applications in which a discrete sensing system with disposable cartridges, such as the one presented here, could be more appropriate. The unique use of the diffused smartphone flash in our system allows for easy and consistent imaging, even in the absence of external light. Moreover, the image processing algorithm was designed to require minimum computational power and is performed in real-time directly on the

smartphone, without the need to transfer and process the data on an additional computer. While a robust wearable sensor is likely more cost-effective than disposable strips for a single application, the same accessory presented here could also be used to measure various additional biomarkers in sweat, saliva, or urine, which could ultimately be more cost-effective for an end user than needing separate microfluidic devices for each desired application.

In order to test the system and observe pH changes during exercise we have performed several experiments with users running on a treadmill between 30 and 60 min. The goal was to show that pH variations during exercise are significant and can indicate something about the intensity of the exercise. The participants in this study were all males between the ages of 25 and 37 who run regularly and participate in competitive racing events. Fig. 5.4a shows pH variations at 3 different run intensities for one user. It shows that at high exercise intensities, characterized by an increased sweat rate, the pH reaches less acidic levels. Fig. 5.4b shows the variations in pH between 3 users running at the same speed of 6mph for 30min. The results indicate that different users exercising in similar ways would need to exert different levels of effort. Fig. 5.4c shows the effect of cooling down by drinking 20 fl. oz. Gatorade at 40 min during 60 min runs. This is expected since sweating is the body's method to regulate its

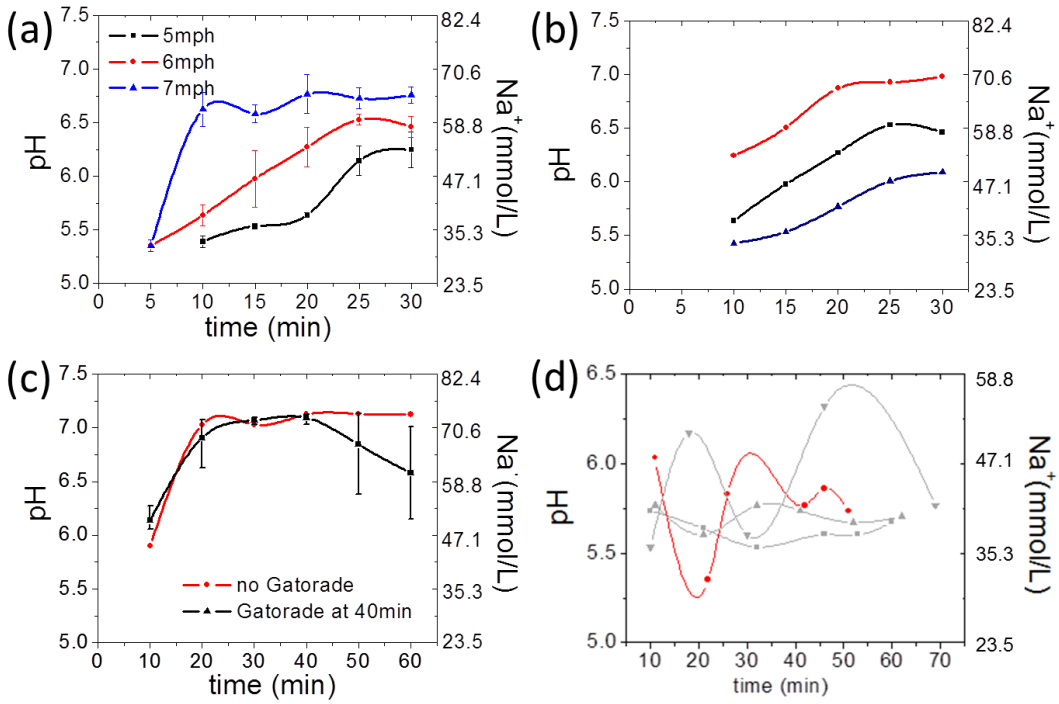

Figure 5.4 Sweat pH and sodium variations during physical exercise a) pH and sodium concentration variations for runs at different intensities b) Variations between 3 different users running at 6mph c) Effect of cooling down with intake of 20 fl oz of Gatorade 40min into the run for one user. Sodium levels are derived from ref [16] d) Hot yoga trials showing pH variations for 4 users during regular exercise. Red line show variation for a user who started hydrating at 10min and maintained constant exercise and regular hydration for the reminder of the trial

temperature (Wyss et al., 1974). Drinking cold fluids decreases the sweat rate and affects the sweat pH.

Because sweat pH has previously been correlated to the concentration of sodium (Patterson et al., 2000), the experimental measurements of pH presented here also give the approximate sodium concentration of the sweat at each stage throughout the run. The sodium concentration is shown on the right y axis in all the experiments in Fig. 5.4. It has also been found that the concentrations of the constituent electrolytes in sweat vary proportionally with sweat rate (Buono et al., 2007; Emrich et al., 1968). By combining these results, an estimate of both the sodium and water losses over time due to sweating can be obtained. Since different users respond to exercise in different ways, there can be no universal guidelines for hydration and electrolyte intake. Using this system to monitor pH and sodium concentration allows for a better estimation of the fluid and electrolyte intake needed to fully replenish losses.

Additional experiments were performed to monitor the variations in sweat pH in other athletes, such as hot yoga practitioners. Hot yoga is the practice of yoga in hot and humid conditions which allows for easy sample collection and analysis. The users involved in these test trials were all women between 21 and 49 who perform hot yoga more than once a week. The users were instructed to perform exercises at their own pace and hydrate at their will. In Fig. 5.4d we show

variation in sweat pH for the 4 users. The user highlighted in red only started hydrating at the 10min mark and maintained a constant exercise pace after, hydrating regularly before cooling off during the last 5min of the trial. The test trials which lasted up to 70 min show the expected patterns of pH variations due to hydration and cooling down periods. The maximum variations were under 1 pH unit and the changes in pH are extremely sensitive to changes in user intensity and hydration. These test trials demonstrate the advantage and applicability of discrete sweat pH measurements in non-continuous forms of athletic activity. These sudden changes in pH can be easily monitored using the system presented here and analyzed directly on a smartphone.

5.4.2 Saliva pH monitoring for preventing enamel decalcification

Another important application for pH monitoring is in preventing enamel decalcification. There have been numerous studies describing the effects of pH on oral health, more specifically on the dissolution of calcium hydroxyapatite, the main inorganic component of dental hard tissues (Gore, 1938). It is believed that enamel decalcification occurs below a certain critical pH that has previously been experimentally determined to be around 6.2 (Fosdick and Starke, 1939). More recent papers describe the critical pH as a function of calcium concentration in saliva (Anderson et al., 2008).

Here we demonstrate the potential of our system to monitor changes in salivary pH through the day. Data from one user during a typical day, from early morning (at t= 0h) until night (at t= 16h), is presented in Fig. 5.5a. Periods of food intake resulted in a rapid increase in pH and are highlighted in blue on the plot. Ultimately, the objective of salivary pH monitoring is to enable people to estimate their risk of enamel decalcification and to make suitable changes in their diet. For this purpose, estimating the amount of time the salivary pH is above a certain value is important. Fig. 5.5b gives this data for 3 different users (all males between the ages of 25 and 37) during a typical day. Figure 5.5c shows the impact of diet on saliva pH for one user. Dental research has shown that bacterial interaction with carbohydrates in the mouth results in the formation of acids(Ludwig and Bibby, 1957). The variations between users are a result of differences in diet and exercise, as well as innate metabolic differences. Changes in diet for each user, however, have a marked impact on the salivary pH over the course of the day. By monitoring the salivary pH of one user on an ordinary and carbohydrate-rich diet (Fig. 5.5c), we can see the effect of carbohydrate-induced acid formation on average salivary pH. The device thus offers the potential for personalized tracking of the effects of various lifestyle changes over time. On a typical balanced diet, the user is above the critical threshold of 6.2 pH for nearly 100% of the day, but this drops down to only half the day on a carb-rich diet,

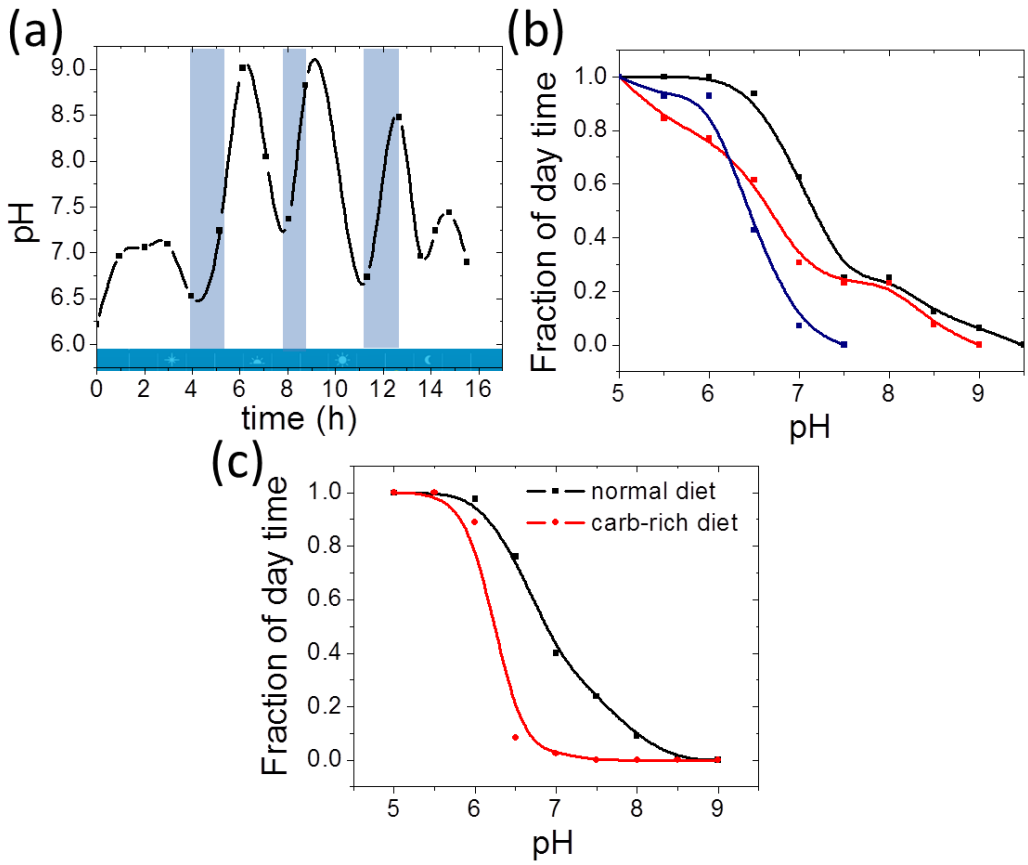

Figure 5.5 Saliva pH variations over the course of a day a) Variations in saliva pH over the course of a day for one user. The colored bars indicate periods of food intake. b) Fraction of the day above a certain pH (data for 3 users) c) Variation in pH for one user on two different diets

resulting in a substantially greater risk of enamel decalcification. These results indicate that the effect of changes in diet can be accurately measured with our device, thus allowing users to make the necessary dietary adjustments in order to improve oral health.

5.5 Conclusion

In this chaper, we have presented a smartphone accessory and app for monitoring pH in sweat and saliva. Sweat pH monitoring is important for proper hydration during physical exercise, while saliva pH monitoring can help users make changes in their diet to prevent enamel decalcification. We have shown through a series of human trials that our system can be used in the context of sweat testing in order to prevent the risk of dehydration and to improve performance during physical activity. In the context of saliva testing, it can be used to evaluate the impact of dietary changes on the risks of enamel decalcification and overall oral health.

Chapter 6

Cholesterol testing on a smartphone[1]

6.1 Abstract

Home self-diagnostic tools for blood cholesterol monitoring have been around for over a decade but their widespread adoption has been limited by the relatively high cost of acquiring a quantitative test-strip reader, complicated procedure for operating the device, and inability to easily store and process results. To address this we have developed a smartphone accessory and software application that allows for the quantification of cholesterol levels in blood. Through a series of human trials we demonstrate that the system can accurately quantify total cholesterol levels in blood within 60 sec by imaging standard test strips. In addition, we demonstrate how our accessory is optimized to improve measurement sensitivity and reproducibility across different individual smartphones. With the widespread adoption of smartphones and increasingly sophisticated image processing technology, accessories such as the one presented here will allow cholesterol monitoring to become more accurate and widespread, greatly improving preventive care for cardiovascular disease.

---

[1] **Oncescu, V**., Erickson, D. "Cholesterol testing on a smartphone" *Lab-on-a-Chip (2013 Accepted)*

6.2 Introduction

The alarming increase in premature deaths due to heart disease in the developed world has resulted in numerous efforts to make blood cholesterol measurements accessible outside the clinical setting. (Malhotra and Chaubey, 2003; Murray and Lopez, 1997) It is estimated that 60% of adults in the US have high cholesterol (over 200 mg/dl), with 37 million among them having very high cholesterol (over 250 mg/dl). (Eckert et al., 2007) Long-term studies on the effect of serum cholesterol on coronary heart disease mortality indicate that there is a 17% increase in mortality rate for every 20mg/dl increase in serum cholesterol levels above 210mg/dl. (Verschuren et al., 1995) Monitoring cholesterol levels is important because it can empower people to make lifestyle choices for preventing heart disease later in life. For some people, improving diet and increasing exercise is enough to lower overall cholesterol, but in some cases medication needs to be prescribed. Products such as Cardiochek PA (Polymer Technology Systems Inc, Indianapolis, USA) and Cholestech LDX (Hayward, USA) have been on the market for over a decade; however home cholesterol testing is still not common. (Whitehead et al., 2013) A recent study suggested that current cholesterol kit users are interested in easier ways of tracking results and that they would test more frequently if supplies were more affordable.(Mintel, 2010) The accuracy of those devices is also a major user concern and has been addressed in several publications. (Rubin et al., 2003; Shemesh et al., 2006; Stein et al., 2002)

Smartphones have the potential of addressing all these issues by eliminating the need for separate test kits. The test strips could be imaged directly on a smartphone and the processed data can be stored for tracking or sent via e-mail directly to a physician. Increasingly sophisticated camera technology on smartphones can also improve the accuracy of cholesterol monitoring. Smartphone accessories for the detection of biomarkers in bodily fluids have been the subject of extensive investigation because they have the potential of greatly decreasing the cost and increasing the availability of heath care in the world. (Ozdalga, 2012; Zhu et al., 2012) In a recent paper we have demonstrated a system for colorimetric monitoring of biomarkers in sweat and saliva. (Oncescu et al., 2013) Several academic groups are also developing smartphone platforms for biomarker detection (Coskun et al., 2013b) and smartphone-based image processing for quantifying colorimetric changes on paper-based immunoassays. (Malhotra and Chaubey, 2003; Murray and Lopez, 1997; Shen et al., 2012)

In this chapter we present and characterize our smartCARD - *smart*phone Cholesterol Application for Rapid Diagnostics – system. The system can quantify cholesterol levels from colorimetric changes due to cholesterol reacting enzymatically on a dry reagent test strip. It consists of a smartphone accessory that allows uniform and repeatable image acquisition of the test strip and an app that analyzes parameters such as hue, saturation and luminosity of the test area,

quantifies the cholesterol levels and displays the value on the screen. In the Methods section, we begin by discussing how the accessory was optimized to improve the accuracy and sensitivity of the colorimetric reaction imaging process. We then discuss the correlation between cholesterol and different image parameters such as saturation and luminosity before presenting the algorithm used to process those parameters and calculate the blood cholesterol levels. In the Results section, we present a series of human trials using the device and characterize the accuracy of the system and reproducibility of the measurements across different smartphones. We conclude by discussing how the system and the test strips can be further improved to increase test accuracy and reproducibility.

6.3 Methods

6.3.1 Smartphone accessory for colorimetric analysis

The smartCARD accessory attaches around the camera of the smartphone as shown in Fig. 6.1a. It has been designed to allow quantification of the cholesterol colorimetric reaction that occurs on a dry reagent test strip over the entire range of physiological cholesterol values. We have investigated different designs and types of lighting sources in order to increase the robustness of the system and

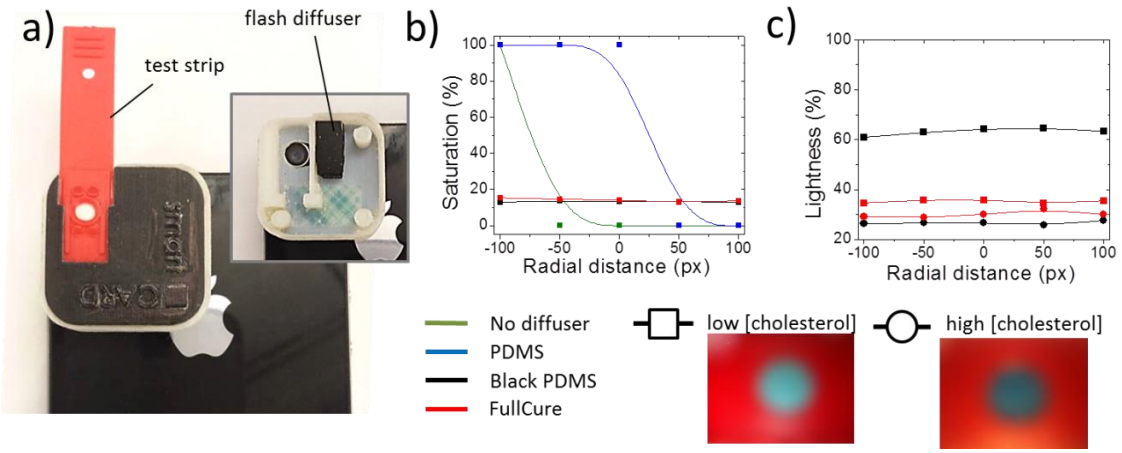

Figure 6.1 smartCARD accessory a) picture of the smartCARD accessory and the test strip used; the inset shows the inside of the accessory with the black PDMS diffuser. b) variation in saturation across a 200px area in the center of the low cholesterol (<100mg/dl) test strip for different diffusers in the smartCARD c) variation in lightness across a 200px area between the low cholesterol strip(<100mg/dl) and high cholesterol (>400mg/dl) strip for 2 different diffusers. The bottom of the figure shows the legend for different diffusers used as well as the 2 test strips used for the data

ability to deal with misalignment of the test strip. In the end, we opted to use the smartphone's flash to illuminate the strip as it provided more uniform lighting for accurately imaging the colorimetric reaction on the test strip. Typical smartphone acquired images of the colorimetric reaction, at low (<100mg/dl) and high (>400mg/dl) cholesterol concentrations are shown at the bottom of Fig. 6.1.

In order to improve the sensitivity of the system to variations in the color of the test strip and to reduce the effect of test strip misalignment into the device, we have incorporated a light diffuser over the flash as can be seen in the inset of Fig. 6.1a. The effect of integrating different diffusers in the smartCARD on the measured saturation values at different points on the detection area is shown in Fig. 6.1b. It can be seen that at low cholesterol concentrations a light diffuser is needed so that the color change can be quantifiable. When no diffuser is used or only PDMS is used the strips appears as white with either 100% or 0% saturation levels. Diffusers made of black PDMS and FullCure, an acrylic-based photopolymer material, allowed for the saturation value on the low cholesterol test strip to be quantifiable with standard error of 0.16% and 0.42% respectively across a 200px section at the center of the strip. This is important because it indicates that misalignment of the test strip will have little effect on the measured saturation value.

The sensitivity of the image acquisition system, defined as the ability to differentiate between colorimetric test strips at different cholesterol

concentrations has also been investigated. As can be seen in Fig. 6.1c the smartCARD accessory with the black PDMS diffuser has on average a 36.6% point decrease in lightness when imaging the high cholesterol test strip compared to the low cholesterol one. The effect is much lower, only 5.2%, when a FullCure diffuser is used. Consequently, black PDMS was used as the diffuser material because it not only allows for uniform illumination of the strip but also maximizes the range of colorimetric variation on the strip

The test strips used in this section are dry reagent strips manufactured by CardioChek (Polymer Technology Systems Inc, IN, USA). When the user applies a drop of blood on one side, it first goes through a series of filter papers that separate plasma from red blood cells and direct some of the plasma towards an analyze-specific reaction pad. At that point, HDL is separated from LDL and VLDL fractions and precipitated by the reaction with phosphotungstic acid. An enzymatic reaction then converts total cholesterol and HDL cholesterol to cholest-4en-3-one and hydrogen peroxide. The peroxide then reacts with disubstituted aniline to form quinoneimine dyes (Eckert et al., 2007; Shephard et al., 2007). The color change from the last reaction is then imaged inside the smartCARD accessory by the smartphone camera.

6.3.2 Correlation between cholesterol levels and colorimetric reaction

In order to quantify the colorimetric reaction and to obtain the blood cholesterol concentration value, we have developed a calibration curve linking cholesterol to

the HSL (Hue Saturation Lightness) cylindrical-coordinate representation of the RGB (Red Green Blue) color values at the center of the cholesterol test strip. The advantage of using HSL coordinates over RGB for smartphone-based colorimetric imaging has been demonstrated in several publications (Cantrell et al., 2010; Chang, 2012; Oncescu et al., 2013; Verschuren et al., 1995). Hue (H) has a piecewise definition and in the region of interest of the cholesterol colorimetric reaction can be written as a function of the red (R), green (G) and blue (B) color values:

$$H = (\text{B-R})/C + 2 \quad \text{if } M = \text{G} \qquad \text{or} \qquad H = (\text{R-G})/C + 4 \text{ if } M = \text{B} \tag{6.1}$$

In the equation above C=M-m where M= max(R,G,B) and m=min(R,G,B). In addition the lightness (L) and saturation (S) are described by the following equations:

$$L = \tfrac{1}{2}(M + m) \tag{6.2}$$

$$S = (\text{M-m}) / (1 - |2L - 1|) \tag{6.3}$$

For the calibration curve, human serum (Sigma Life Science, USA) was used and augmented using Cholesterol Lipid Concentrate (Rocky Mountain Biologicals Inc, MT USA) in order to cover the whole range of physiological cholesterol levels. At each cholesterol concentration in the relevant physiological range (140mg/dl to 400mg/dl) the test strip was first analyzed using the CardioChek portable Blood Test System and then imaged using the smartCARD system. In Fig. 6.2a we show the variations in lightness and saturation for images acquired using the smartCARD system. The cholesterol reading is first obtained using the

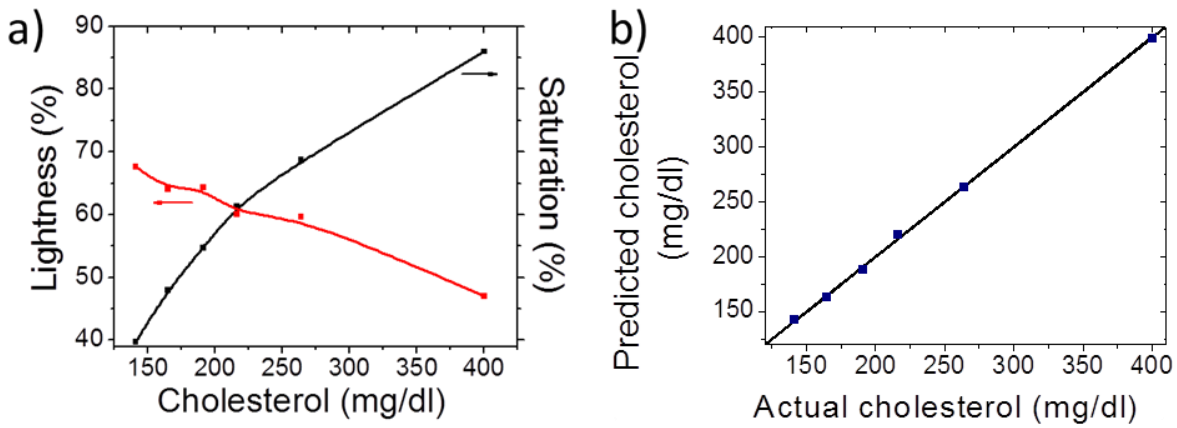

Figure 6.2 Relationship between image HSL and cholesterol levels a) variation in lightness (red) and saturation (black) vs cholesterol levels b) predicted cholesterol concentration versus actual cholesterol concentration defined by CardioCheck PA

CardioChek portable Blood Test System. The hue values show very little variation across the whole range of cholesterol values and are not shown in Fig. 6.2a. However, as we will show later in the Results section, hue values can be used to indicate if a test is successful or if it fails due to image acquisition or test strip issues. The relationship between concentration and saturation can be described by a second order polynomial.

$$[\text{Chol}] = 0.08S^2 - 4.56S + 196.84 \quad (6.4)$$

As can be seen in Fig. 6.2b this allows almost perfect matching with a maximum error of 1.8%.

6.3.3 Smartphone image acquisition and processing

Several groups have developed algorithms for test-strip colorimetric analysis on a smartphone and have demonstrated their application measuring simple colorimetric reactions such as pH (Oncescu et al., 2013; Shen et al., 2012; Whitehead et al., 2013). In those cases instantaneous reactions make it easy to image. Slow enzymatic reactions involving whole blood separation steps such as for cholesterol monitoring have the additional complication of being time dependent and more variable due to strip manufacturing variability. For such cases, Mohapatra *et al.* (Mintel, 2010; Mohapatra and Phillips, 2013) has proposed using a personal glucose meter to quantify active enzyme analytes as a way of reducing the effects of lighting conditions, focus and camera differences. Other groups have focused on improving the algorithm for image processing and

combining it with an accessory that block external lighting for the analysis of time varying reactions such as fluorescent assays (Coskun et al., 2013a; Rubin et al., 2003; Schwaebel et al., 2013; Shemesh et al., 2006; Stein et al., 2002).

Here we have developed a smartphone application for the iPhone iOS platform that in combination with the smartCARD accessory allows for image acquisition and colorimetric analysis of the cholesterol enzymatic reaction. A screenshot of the app is shown in Fig. 6.3a. When the user presses "analyze" on the app, an image of the colorimetric color changes is acquired through the iPhone camera. As shown in the Fig. 6.3b schematic, the app then executes several processing steps before the cholesterol value is displayed on the screen. First, a 100px by 100px calibration area is selected at the bottom right corner of the image. The average RGB value is computed and converted to HSL. This average HSL value is then compared to a reference value and a background shift is computed. The whole image is then is subjected to this background shift. After the background shift, a 100px by 100px area in the middle of the detection circle is then selected and the same computation as before is done to obtain the average HSL value of the test area. The algorithm then verifies if the test is valid by comparing the average hue value to the typical value of the cholesterol test, which as we will show in the Results section is constant across physiological cholesterol values ($H\sim 180$) both for serum samples and blood samples during test trials. In order to decrease fluctuations due to lighting conditions, the strip is imaged 3 times and

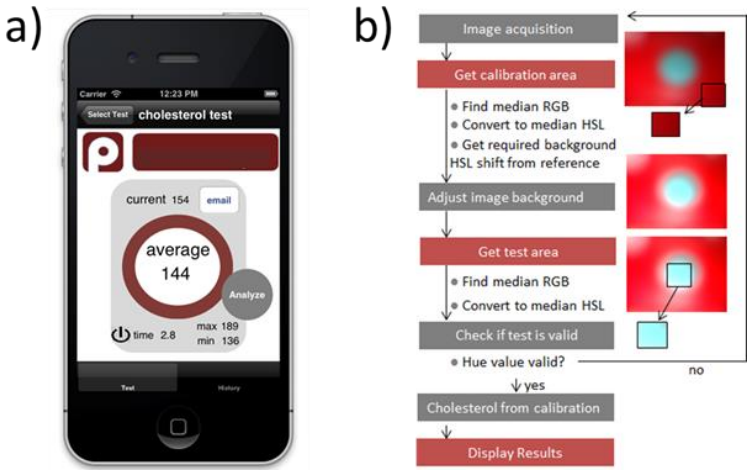

Figure 6.3 App and algorithm for cholesterol quantification a) screenshot of the app showing current cholesterol reading as well as average reading for one user) algorithm used for image processing and implemented in iOS app

the average hue value over those 3 images is taken. If the hue value falls within the range of expected hue values, than the cholesterol level is calculated using the calibration curve obtained in the previous section. The ability of identifying bad samples is a major advantage over specialized hand-held devices, such as CardioChek PA, that use reflectance photometry to quantify colorimetric reaction.

6.4 Results and discussion

6.4.1 Accuracy and reproducibility

A critical issue to consider for point-of-care testing is the accuracy of the measurement. Once the user applies a drop of blood on the strip it takes some time for the colorimetric change to occur on the other side of the strip since the blood goes through several separation steps and chemical reactions and the colorimetric change occurs gradually as can be seen at the bottom of Fig. 6.4. If the strip is imaged before the reaction has terminated then we will get a misleadingly low value for the blood cholesterol level. In order to determine the approximate time required for the reaction to occur we have monitored the color change for a serum sample with an actual concentration of 178mg/dl. As can be seen in Fig. 6.4a it takes about 60s for the colorimetric change to stabilize. The variation in predicted cholesterol levels are contained within less than 3.9% of

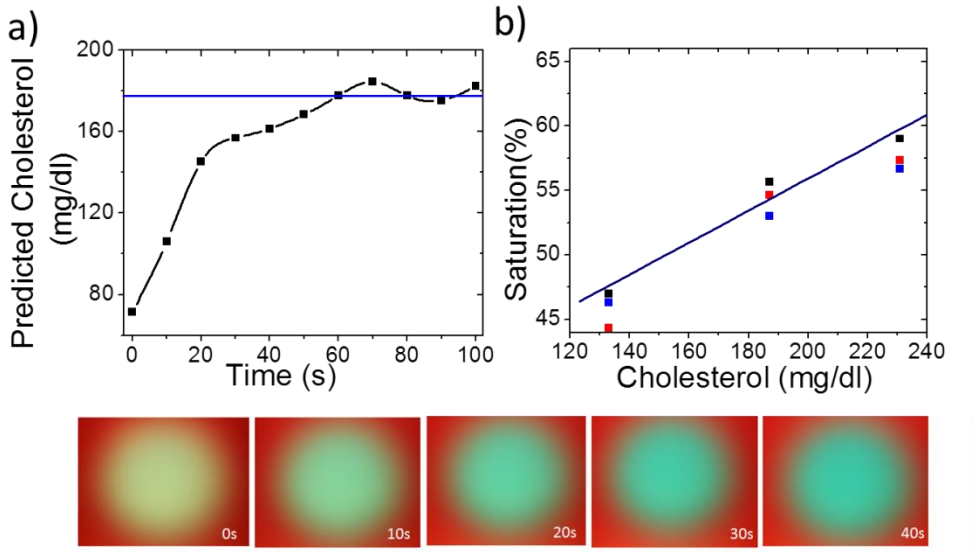

Figure 6.4 Accuracy and reproducibility a) variations in predicted cholesterol levels vs time for a test strip with the clue horizontal line representing the actual cholesterol level of 178mg/dl b) variation in readings with different 3 different iPhones. The bottom of the figure shows the imaging of the test strip during the first 40s.

the actual value after that however the value shifts up as time elapses. It is therefore important to be consistent by building in the algorithm a time frame for imaging the test strip. In addition averaging several acquired images during that time frame can helped further improve the accuracy. Therefore in next section the image acquisition is all done between 60s and 80s and the predicted cholesterol is the average of the predicted cholesterol on 3 different images. As will be shown in the next section the 3.9% inter-assay variation that was observed here for the smartCARD system is lower than what was observed for other lipid point-of-care device.

Another important feature of the smartCARD system is that it can be used on different smartphone platforms with small variability. Fig. 6.4b shows the imaging of the same test strips with 3 different smartphone cameras across a wide range of physiological cholesterol values. The maximum difference between readings is 5.8% which is significant but on the same order as the CardioChek PA system reading error. This error between phones can be minimized by designing custom strips that allow for better calibration as we showed in our previous publication.

6.4.2 Validation of smartCARD for human trials

In order to demonstrate the ability the smartCARD system for determining blood cholesterol levels we ran user experiments and compared the predicted cholesterol levels to the actual cholesterol levels as indicated by the CardioCheck

PA lipid point-of-care device. As can be seen in Fig. 6.5a from the 9 readings taken, the maximum difference between our predicted value and the CardioCheck PA reading was 5.5% in one instance with less than 3% difference for all the other readings.

For the CardioCheck PA the observed inter-assay imprecision has been recorded by Shephard *et al.* (Ozdalga, 2012; Shephard et al., 2007; Zhu et al., 2012)as 4.4% and observed bias with respect to a CDC-certified laboratory method has been recorded as 12.1%. Other studies produced similar results for lipid point-of-care devices (Carey et al., 2006; Oncescu et al., 2013; Parikh et al., 2009; Stein et al., 2002). Inter sample and comparative difference for the smartCARD system indicates that the error is lower than for such point-of-care systems.

In addition, the smartCARD algorithm can identify erroneous readings caused by misalignment of the test strip in the accessory or insufficient amount of blood on the test strip. During the human trials, two readings were discarded because the recorded hue didn't fall within the normal range of hue values (170° to 190°) as shown in Fig. 6.5b. A low hue value can indicate that the amount of blood applied on the test strip is not sufficient or that the sample was contaminated. Further investigation into the reasons why some tests fall outside the normal hue range would be useful to improve the system but is beyond the scope of this chapter.

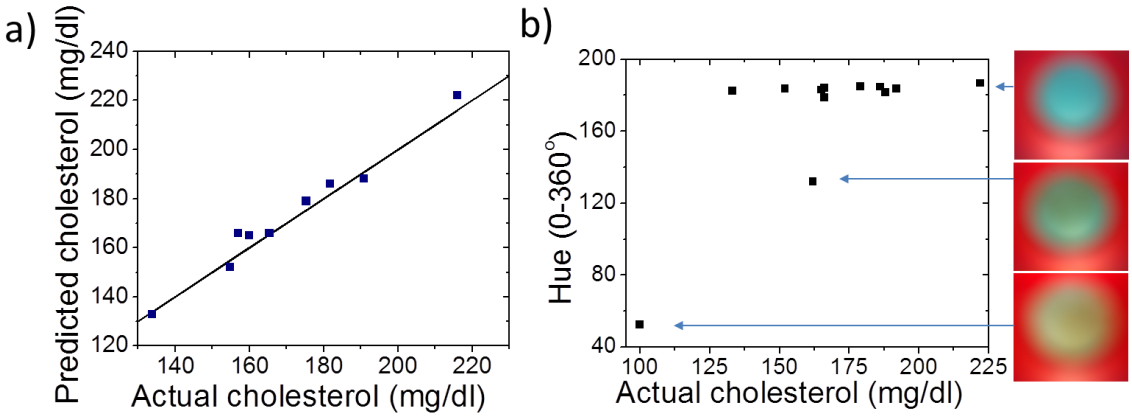

Figure 6.5 Test trials of smartCARD device and comparison to commercial device a) difference between CardioChek PA reading and smartCARD for human trails b) Hue differences for all the human test trials showing that discarded tests give hue values outside of the normal range (170-190°)

6.5 Conclusion

In this chapter we demonstrate a system that can be used to measure and track cholesterol levels directly on a smartphone. The smartCARD system is designed in a way that allows for optimal image acquisition. We showed that we can obtain cholesterol levels within 1.8% accuracy by looking at the acquired image's saturation. We also demonstrated interphone repeatability before performing user experiments and measuring blood cholesterol levels with the system we have developed. The smartCARD predicted cholesterol values for the user testing were compared to the measured value using the CardioChek PA system and found that the maximum difference between our predicted value and the CardioCheck PA reading were less than 5.5% in all cases.

Chapter 7

Conclusion and Future Work

7.1 Conclusion

In this thesis we have presented developments in two areas that have the potential of revolutionizing medical technology and point-of-care devices .

One area is that of autonomous implantable devices. Such devices are promising for conditions that require constant monitoring such as diabetes, where fluctuations in glucose levels can occur at any time, and the administration of insulin cannot wait for the user to react. In Chapter 2 we presented such a device for the prevention of late-phase hemorrhagic shock (HS). It incorporates a nanowire biosensor that allows the continuous monitoring of vasopressin in solution, an electrochemical drug delivery system that delivers vasopressin at the onset of late-phase HS to stabilize the situation, and a glucose fuel cell to power the whole device. The need for a power source to power such autonomous implantable devices is discussed extensively in Chapter 3 and 4 of this thesis. Given the high-power demand and desired length of implantation of many such autonomous devices, lithium batteries cannot continue to be the only source of energy. In Chapter 3, we propose a glucose fuel cell that can act as coating layer

to many high surface area implantable devices. In Chapter 4 we come up with an innovative glucose fuel cell that can be stacked to produce a high power density fuel cell unit. That is the fuel cell unit that was used in Chapter 2 to power the device for the prevention of late-phase HS.

The second area that is covered in this thesis is that of smartphone diagnostics. There are numerous colorimetric reactions – chemical, enzymatic, gold nanoparticle immunoassays – that can be quantified using a smartphone platform. In Chapter 5 we demonstrate the general idea by showing that we can monitor pH changes in sweat and saliva accurately and precisely across different smartphones. The system consists of a test strip, an accessory that goes around the camera of the smartphone and that ensures image uniformity and a app processes the data and displays it on the screen for the user. We show several applications where pH monitoring is useful.

In Chapter 6 we demonstrate that that the system can accurately quantify total cholesterol levels in blood within 60 sec by imaging standard test strips. Finally in Chapter 7 we present a novel colorimetric gold nanoparticle-based immunoassay for 25-hydroxyvitamin D and demonstrate that can perform a vitamin D deficiency testing with the same accurately as commercial ELISA kits.

7.2 Future Developments for Autonomous Implantable Devices

7.2.1 Autonomous implantable device for late-phase HS

Miniaturization and i*n-vivo* testing are the next steps in the development of an implantable hemoAID. The operation of the individual components of this device, or similar technologies, have been demonstrated elsewhere *in-vivo* or in serum. The vasopressin drug delivery system presented here is based on a device, by Chung *et al.*, that allows controlling the rate of drug ejection and has been later shown to operate *in-vivo* in *Manduca sexta* moths (Chung and Erickson, 2009). In that work the drug delivery devices are sealed using biocompatible wax and implanted in the moths for over 2 days demonstrating stability of vasopressin during storage and upon electrochemical ejection. Other groups have developed similar micro-electro-mechanical-systems(MEMS) for rapid delivery of vasopressin and have demonstrated biocompatibility and long term vasopressin storage without degradation (Elman et al., 2009). Some preliminary *in-vivo* studies in rabbits have been reported by H. L. Ho. Duc where a 20μL dose of 100μg/kg vasopressin solution is delivered subcutaneously and an increase in plasma vasopressin levels was observed to reach a stable concentration after about 1h (Duc, 2009). These experiments demonstrate that such drug delivery technology is suitable for implantation and that the amount of vasopressin required is not an obstacle. The hemoAID reservoir contains approximately 16μL of concentrated vasopressin solution (200μM) or approximately 1.4 IU. When the

device is loaded with a saturated solution of Arg8-vasopressin (400 IU/mg with 20 mg/ml solubility (Dawson et al., 1969)) it is able to deliver a maximum of 128 IU. This falls within the range of vasopressin levels required to temporarily maintain a late-HS patient alive as discussed previously. Multiple drug delivery reservoirs can be integrated to deliver vasopressin over a longer period of time without substantially increasing the volume of the device as was done by Chung *et al.* (Chung et al., 2012).

In the current form, the device is integrated in a $3cm^3$ packaging with the fuel cell occupying about $1cm^3$ and the circuitry being external to the device. The miniaturization of similar circuitry has been demonstrated by Gumus *et al.* for application in *in-vivo* uric acid sensing on pigeons[30]. We envision the final version of the hemoAID, with multiple vasopressin drug delivery reservoirs, on-board circuitry and coated in biocompatible wax, to be suitable for sub-cutaneous implantation (Gumus et al., 2014).

7.3 Future Developments for Smartphone Diagnostics

Because the device presented in Chapter 5 allows for reproducible colorimetric detection with minimal user error, we believe that such a system could also be extended to a wide range of biomarkers for other portable diagnostics applications.

For the cholesterol device presented in Chapter 6 it is possible to design the cholesterol test strips in such a way as to further minimize analysis fluctuations. We have demonstrated in a previous publication that by incorporating and imaging a white reference area on the test strip, we can adjust the white balance and get more reproducible results across different smartphones. (Coskun et al., 2013b; Oncescu et al., 2013) Finally, using the smartCARD system presented here it is possible to measure other commercially available colorimetric test strips for LDL, HDL cholesterol, and triglycerides.

In a paper not presented in this thesis, we have developed a system shown in Fig. 7.1 for rapid quantification of vitamin D levels on a smartphone. This is achieved through the development of: a smartphone accessory, app, and novel gold nanoparticle (AuNP) based colorimetric competitive direct-antigen immunoassay.

We demonstrate that using this system we can measure physiological levels of 25(OH)D in solution with accuracy better than 15nM and a precision of 10nM. Moreover we show that the results obtained using this system are comparable with that of commercial ELISA kits. By analyzing 3 serum samples with unknown 25(OH)D concentration we were able to determine accurately the severity of the 25(OH)D deficiency in each case. These results are promising for tackling the problems associated with vitamin D deficiency both in the developed and the developing world. This also opens the door to the quantification of numerous immunoassays directly on a smartphone.

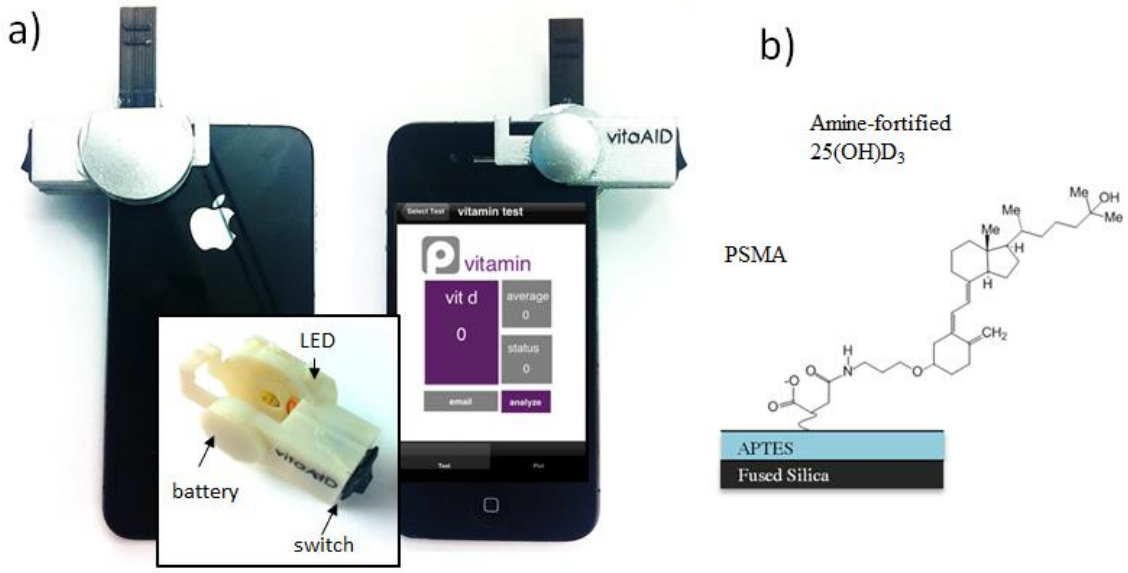

Figure 7.1 Vitamin D quantification on a smartphone a) accessory for vitamin D quantification on a iPhone with the inset showing the components of the accessory b) schematic showing surface chemistry on the test strip

Appendix 1

Single Layer Fuel Cell Microfabrication

In this section we discuss the detailed microfabrication protocol of the single-layer fuel cell (SLFC) presented in Chapter 4 of this thesis.

The fabrications steps for the fuel cells described here and shown in Fig. A1.1 were performed at the Cornell Nanofabrication Facility. 500μm thick fused silica wafers were used due to the fact that electrode can be patterned directly on them without the need of depositing a silicon oxide layer. If silicon wafers are used an oxide layer needs to be deposited using a GSI PECVD tool. The electrodes were patterned one at a time using a lift-off process. First for the anode:

- Spin S1818 at 2000rpm for 60sec
- Hot plate for 60sec at 95C
- Expose for 25sec in ABM
- Submerge wafer in toluene for 3min (keep agitating)
- Hot plate for 30sec at 95C
- Develop in 321MIF for 90sec (repeat if needed another time)

The anode was patterned using E-beam evaporation (CHA Evaporator) where 20nm of titanium was deposited in order to promote adhesion followed by

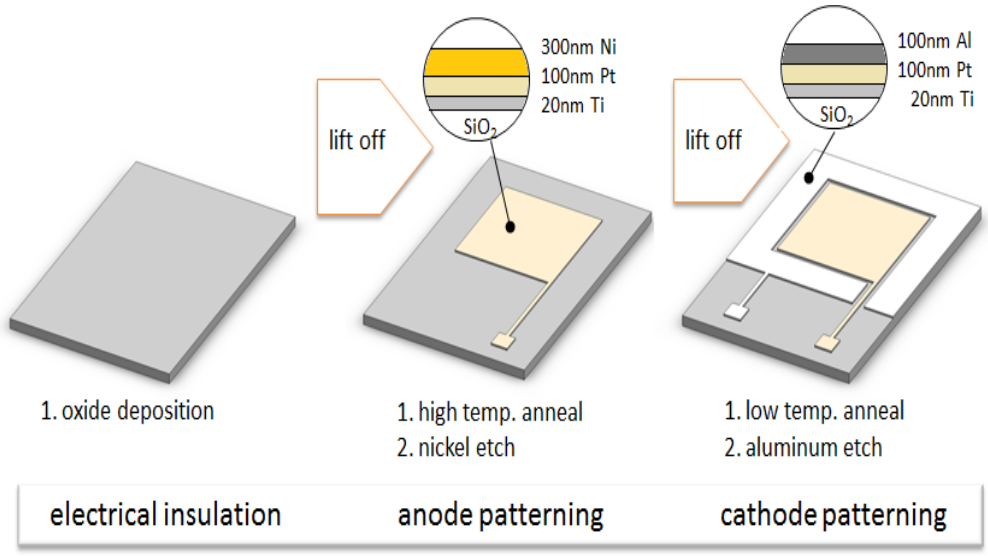

Figure A1.1 Fabrication steps for the single layer fuel cell

100nm of platinum and 300nm of nickel. The photoresist was then removed so that only the patterned anode remained on the wafer by

- Submerging wafer in 1165 for about 3h (face down with constant stirring)

The wafer was subsequently annealed for 2 hours in nitrogen gas at 600°C (MRL Industries Furnace). In order to avoid oxide formation when opening and closing the furnace door, the stand-by temperature of the furnace was kept bellow 300°C. In order to obtain a high surface area Raney-type surface the nickel was etched by keeping the wafers in a 1:1 solution of concentrated sulfuric acid and nitric acid for 12 h.

For the cathode, the following process was used:

- Spin S1818 at 2000rpm for 60sec
- Hot plate for 60sec
- Expose for 9sec in ABM
- Submerge wafer in toluene for 3min
- Hot plate for 30sec
- Develop in 321MIF for 90sec (repeat if needed another time)

The cathode was patterned using E-beam evaporation of 20nm of titanium followed by 100nm of platinum and 100nm aluminum. Then:

- Submerge wafer in 1165 for about 3h (face down with constant stilling)

The wafer was subsequently annealed for 1 hour in nitrogen gas at 300°C followed by the etching the aluminum in 0.1M NaOH solution. The fused silica wafers were then diced (K&S 7100 Dicing Saw) into 10mm by 12mm pieces. Copper wires (30 gauge) were soldered directly onto the electrodes.

Appendix 2

Vasopressin Biosensor Microfabrication

A2.1 Reagents and materials

Arginine vasopressin with with Cys-Tyr-Phe-Gln-Asn-Cys-Pro-Arg-Gly-NH2 sequence and lypressin with Cys-Tyr-Phe-Gln-Asn-Cys-Pro-Lys-Gly-NH_2 sequence were purchased from American Peptide Company Inc. Aptamer, 55-nt single-stranded DNA pool synthesized with the sequence 5'-TCACGTGCATGATAGACGGCGAAGCCGTCGAGTTGCTGTGTGCCGATGC ACGTGA, was ordered from Integrated DNA Technologies Inc. COOH-functionalized multiwall carbon nanotubes were obtained from Cheap Tubes Inc. N-hydroxysuccinimide (NHS) and Sodium dodecylsulfate (SDS) were purchased from MP Biomedicals LLC, while 1-ethyl-3-(3-dimethylaminopropyl) carbodiimide (EDC) was purchased from Geno Technology, Inc Sheep Serum was obtained from Valley Biomedical Inc. and human serum albumin (HSA) was purchased from Sigma-Aldrich Co.

A2.2 Patterning of CNTs and Gold Electrodes on Silicon Wafer

In this design CNTs were immobilized between two lithographically patterned gold electrodes with a gap of 10 μm. A gap of 10 μm was chosen for the CNT

pattern because initial experiments have demonstrated increased sensitivity with decreasing gap in the 10-50 μm range. First a 4-inch silicon wafer was cleaned and oxidized in hot piranha solution in order to generate hydroxyl groups on its surface. Microposit S1805 Photo Resist was than spin-coated on the silicon wafer surface and the CNT pattern was created using standard photolithography. The silicon wafer was then treated in Molecular Vapor Deposition Tool (MVD 100) for a 15 minutes (3-aminopropyl)trimethoxysilane (APTMS) deposition to create a amine group monolayer on its surface. Carbon nanotubes dispersed in 0.5% SDS solution (0.1 mg/mL) were pipetted on APTMS-treated CNT pattern and allowed and allowed to immobilize on the surface at room temperature for three hours. Subsequently, the wafer was oven-baked overnight at 80 °C.

The gold electrodes were patterned using a standard LOR3A lift-off process. The patterned CNTs were aligned with the gold electrode pattern and 5 nm chromium/60 nm gold were deposited on the wafer using a e-Beam Evaporator.

A2.3 Surface Modification of Patterned CNT on Silicon Wafer.

The core of the sensing device is the signal-transducible carbon nanotubes with surface modification of aptamers, which are amine-terminated fifty-five base oligonucleotides with a cyclic structure. It allows the tight binding of specific target, vasopressin molecules. Before the aptamer immobilization, a mixture of

0.4 M EDC and 0.1 M NHS in 1:1 volume ratio was pipetted on the CNT-immobilized pattern of the sensor. The mixture droplets were maintained on the pattern for 3 hours at room temperature in order to create an EDC/NHS activation layer on which aptamer can effectively be immobilized. Subsequently, the sensors were cleaned with DI H_2O wash and N_2 dry. Aptamer at 1 μM concentration was then pipetted on the EDC/NHS-modified CNTs and maintained for 24 hours at room temperature for immobilization. The aptamer-modified sensors were once again cleaned with DI H_2O wash and N_2 dry. For both NHS/EDC and aptamer modifications, 1.5 μL of solution droplet was used per sensor to cover its detection area entirely. To prevent the premature drying of the droplets, the sensors were kept in a humidified chamber.

References

Adler, A., Halkin, A., and Viskin, S. (2013). Wearable Cardioverter-Defibrillators. Circulation *127*, 854–860.

Anand, T., and Skinner, R. (2012). Arginine vasopressin: The future of pressure-support resuscitation in hemorrhagic shock. Journal of Surgical Research *178*, 321–329.

Anderson, P., Hector, M.P., and Rampersad, M.A. (2008). Critical pH in resting and stimulated whole saliva in groups of children and adults. International Journal of Paediatric Dentistry *11*, 266–273.

Arriagada, A.J., Jurkov, A.S., Neshev, E., Muench, G., Andrews, C.N., and Mintchev, M.P. (2011). Design, implementation and testing of an implantable impedance-based feedback-controlled neural gastric stimulator. Physiol. Meas. *32*, 1103–1115.

Barone, P.W., Baik, S., Heller, D.A., and Strano, M.S. (2004). Near-infrared optical sensors based on single-walled carbon nanotubes. Nat Mater *4*, 86–92.

Barton, S.C., Gallaway, J., and Atanassov, P. (2004). Enzymatic biofuel cells for implantable and microscale devices. Chemical Reviews *104*, 4867–4886.

Bullen, R.A., Arnot, T.C., Lakeman, J.B., and Walsh, F.C. (2006). Biofuel cells and

their development. Biosensors and Bioelectronics *21*, 2015–2045.

Buono, M.J., Ball, K.D., and Kolkhorst, F.W. (2007). Sodium ion concentration vs. sweat rate relationship in humans. Journal of Applied Physiology *103*, 990–994.

Bush, D.M. (2008). The U.S. Mandatory Guidelines for Federal Workplace Drug Testing Programs: Current status and future considerations. Forensic Science International *174*, 111–119.

Cantrell, K., Erenas, M.M., de Orbe-Paya, I., and Capitán-Vallvey, L.F. (2010). Use of the Hue Parameter of the Hue, Saturation, Value Color Space As a Quantitative Analytical Parameter for Bitonal Optical Sensors. Analytical Chemistry *82*, 531–542.

Carey, M., Markham, C., Gaffney, P., and Boran, G. (2006). Validation of a point of care lipid analyser using a hospital based reference laboratory. Irish Journal of Medical Science *175*, 30–35.

Cebotari, S., Tudorache, I., Schilling, T., and Haverich, A. (2010). Heart valve and myocardial tissue engineering. Herz *35*, 334–341.

Chang, B.Y. (2012). Smartphone-based chemistry instrumentation: digitization of colorimetric measurements. Bulletin of the Korean Chemical Society *33*, 549–552.

Chaudhuri, S.K., and Lovley, D.R. (2003). Electricity generation by direct oxidation of glucose in mediatorless microbial fuel cells. Nat Biotechnol *21*, 1229–1232.

Chung, A.J., and Erickson, D. (2009). Engineering insect flight metabolics using immature stage implanted microfluidics. Lab on a Chip *9*, 669–676.

Chung, A.J., Kim, D., and Erickson, D. (2008). Electrokinetic microfluidic devices for rapid, low power drug delivery in autonomous microsystems. Lab on a Chip *8*, 330–338.

Chung, A.J., Cordovez, B., Jasuja, N., Lee, D.J., Huang, X.T., and Erickson, D. (2012). Implantable microfluidic and electronic systems for insect flight manipulation. Microfluid Nanofluid *13*, 345–352.

Chung, A.J., Huh, Y.S., and Erickson, D. (2009). A robust, electrochemically driven microwell drug delivery system for controlled vasopressin release. Biomed Microdevices *11*, 861–867.

Cinquin, P., Gondran, C., Giroud, F., Mazabrard, S., Pellissier, A., Boucher, F., Alcaraz, J.-P., Gorgy, K., Lenouvel, F., Mathé, S., et al. (2010). A Glucose BioFuel Cell Implanted in Rats. PLoS ONE *5*, e10476.

Cook-Chennault, K.A., Thambi, N., and Sastry, A.M. (2008). Powering MEMS portable devices—a review of non-regenerative and regenerative power supply systems with special emphasis on piezoelectric energy harvesting systems. Smart Mater. Struct. *17*, 043001.

Cordovez, B., Chung, A.J., Mak, M., and Erickson, D. (2010). A novel polymer microneedle fabrication process for active fluidic delivery. Microfluid Nanofluid

10, 785–791.

Coskun, A.F., Nagi, R., Sadeghi, K., Phillips, S., and Ozcan, A. (2013a). Albumin testing in urine using a smart-phone. Lab on a Chip *13*, 4231.

Coskun, A.F., Wong, J., Khodadadi, D., Nagi, R., Tey, A., and Ozcan, A. (2013b). A personalized food allergen testing platform on a cellphone. Lab on a Chip *13*, 636–640.

Coyle, S., Di Francesco, F., Costanzo, D., and Salvo, P. (2010). BIOTEX—Biosensing Textiles for Personalised

Healthcare Management. IEEE Transactions of Information Technology in Biomedicine *16*, 364–370.

Curto, V.F., Fay, C., Coyle, S., Byrne, R., and O'Toole, C. (2012). Real-time sweat pH monitoring based on a wearable chemical barcode micro-fluidic platform incorporating ionic liquids. Sensors and Actuators B: Chemical *171-172*, 1327–1334.

Curto, V.F., Coyle, S., Byrne, R., Diamond, D., and Benito-Lopez, F. (2011). Real-Time Sweat Analysis: Concept and Development of an Autonomous Wearable Micro-Fluidic Platform. Procedia Engineering *25*, 1561–1564.

Davis, F., and Higson, S. (2007). Biofuel cells—Recent advances and applications. Biosensors and Bioelectronics *22*, 1224–1235.

Davis, J.J., Coles, R.J., Allen, H., and Hill, O. (1997). Protein electrochemistry at

carbon nanotube electrodes. Journal of Electroanalytical Chemistry *440*, 279–282.

Dawes, C. (2003). What is the critical pH and why does a tooth dissolve in acid? Journal-Canadian Dental Association *69*, 722–725.

Dawson, R., Elliot, D.C., Elliot, W.H., and Jones, K.M. (1969). pH, buffers and physiological media. Data for Biochemical Research … 501–502.

Drake, R.F., Kusserow, B.K., Messinger, S., and Matsuda, S. (1970). A tissue implantable fuel cell power supply. ASAIO Journal *16*, 199–205.

Duc, H.H. (2009). DSpace@MIT: Emergency delivery of Vasopressin from an implantable MEMS rapid drug delivery device.

Ebel, H., Rust, D., Tronnier, V., Böker, D., and Kunze, S. (1996). Chronic precentral stimulation in trigeminal neuropathic pain - Springer. Acta Neurochirurgica.

Eckert, G.P., Müller, W.E., and Wood, W.G. (2007). Cholesterol-lowering drugs and Alzheimer's disease. Future Lipidology *2*, 423–432.

Eichner, E.R. (2007). Blood Doping. Sports Medicine *37*, 389–391.

Elman, N.M., Ho Duc, H.L., and Cima, M.J. (2009). An implantable MEMS drug delivery device for rapid delivery in ambulatory emergency care. Biomed Microdevices *11*, 625–631.

Emrich, H.M., Stoll, E., Friolet, B., Colombo, J.P., Richterich, R., and Rossi, E. (1968). Sweat Composition in Relation to Rate of Sweating in Patients with Cystic

Fibrosis of the Pancreas. Pediatr Res *2*, 464–478.

Esquivel, J.P., Colomer-Farrarons, J., Castellarnau, M., Salleras, M., del Campo, F.J., Samitier, J., Miribel-Català, P., and Sabaté, N. (2012). Fuel cell-powered microfluidic platform for lab-on-a-chip applications: Integration into an autonomous amperometric sensing device. Lab on a Chip *12*, 4232–4235.

Farra, R., Sheppard, N.F., McCabe, L., Neer, R.M., Anderson, J.M., Santini, J.T., Cima, M.J., and Langer, R. (2012). First-in-Human Testing of a Wirelessly Controlled Drug Delivery Microchip. Science Translational Medicine *4*, 122ra21–122ra21.

Federspil, P.A., and Plinkert, P.K. (2004). Restoring Hearing with Active Hearing Implants / Wiederherstellung des Gehörs mit aktiven Hörimplantaten. Biomedizinische Technik/Biomedical Engineering *49*, 78–82.

Fogel, R.W. (2009). Forecasting the cost of U.S. Health Care in 2040. Journal of Policy Modeling *31*, 482–488.

Fojtik, M., Kim, D., Chen, G., Lin, Y.S., Fick, D., Park, J., and Seok, M. (2013). A Millimeter-Scale Energy-Autonomous Sensor System With Stacked Battery and Solar Cells

. IEEE Journal of Solid-State Circuits *48*, 801–812.

Fosdick, L.S., and Starke, A.C. (1939). Solubility of Tooth Enamel in Saliva At Various pH levels. Journal of Dental Research *18*, 417–430.

Fox, S., and Duggan, M. (2010). Mobile Health 2010. Pew Internet & American Life Project. Retrieved May 2012.

Gao, P.X., Song, J., Liu, J., and Wang, Z.L. (2007). Nanowire Piezoelectric Nanogenerators on Plastic Substrates as Flexible Power Sources for Nanodevices. Adv. Mater. *19*, 67–72.

Gore, J.T. (1938). Saliva and Enamel Decalcification: II. Saliva Separator. Journal of Dental Research *17*, 69–74.

Gumus, A., Lee, S., Karlsson, K., Gabrielson, R., Winkler, D.W., and Erickson, D. (2014). Real-time in vivo uric acid biosensor system for biophysical monitoring of birds. Analyst –.

Halámková, L., Halámek, J., Bocharova, V., Szczupak, A., Alfonta, L., and Katz, E. (2012). Implanted Biofuel Cell Operating in a Living Snail. J. Am. Chem. Soc. *134*, 5040–5043.

He, P., Oncescu, V., Lee, S., Choi, I., and Erickson, D. (2013). Label-free electrochemical monitoring of vasopressin in aptamer-based microfluidic biosensors. Analytica Chimica Acta *759*, 74–80.

Heller, A. (2004). Miniature biofuel cells - Physical Chemistry Chemical Physics. Physical Chemistry Chemical Physics *6*, 209–216.

Heller, A. (2006). Potentially implantable miniature batteries. Anal Bioanal Chem *385*, 469–473.

Hussain, F., Evans, N.D., and Sachedina, N. (2005). In vivo glucose monitoring: the clinical reality and the promise. Biosensors and Bioelectronics *20*, 1897–1902.

Jalilian, E., Onen, D., Neshev, E., and Mintchev, M.P. (2007). Implantable neural electrical stimulator for external control of gastrointestinal motility. Medical Engineering & Physics *29*, 238–252.

Jochberger, S., Morgenthaler, N.G., Mayr, V.D., Luckner, G., Wenzel, V., Ulmer, H., Schwarz, S., Hasibeder, W.R., Friesenecker, B.E., and Dunser, M.W. (2006). Copeptin and Arginine Vasopressin Concentrations in Critically Ill Patients. Journal of Clinical Endocrinology & Metabolism *91*, 4381–4386.

Joun, G.B., and Cho, B.H. (1998). An Energy Transmission System for an Artificial Heart Using Leakage Inductance Compensation of Transcutaneous Transformer

. IEE Transactions on Power Electronics *13*, 1013–1022.

Kennedy, R.T., Watson, C.J., Haskins, W.E., Powell, D.H., and Strecker, R.E. (2002). In vivo neurochemical monitoring by microdialysis and capillary separations. Current Opinion in Chemical Biology *6*, 659–665.

Kerzenmacher, S., and Sumbharaju, R. (2007). A sourface mountable glucose fuel cell for medical implants. Transducers & Eurosensors 125–128.

Kerzenmacher, S., Ducrée, J., and Zengerle, R. (2008a). Energy harvesting by implantable abiotically catalyzed glucose fuel cells. Journal of Power Sources *182*,

1–17.

Kerzenmacher, S., Ducrée, J., and Zengerle, R. (2008b). An abiotically catalyzed glucose fuel cell for powering medical implants: Reconstructed manufacturing protocol and analysis of performance. Journal of Power Sources *182*, 66–75.

Kerzenmacher, S., Kräling, U., Metz, T., and Zengerle, R. (2011). A potentially implantable glucose fuel cell with Raney-platinum film electrodes for improved hydrolytic and oxidative stability. Journal of Power Sources *196*, 1264–1272.

Kerzenmacher, S., Kräling, U., Schroeder, M., Brämer, R., Zengerle, R., and Stetten, von, F. (2010a). Raney-platinum film electrodes for potentially implantable glucose fuel cells. Part 2: Glucose-tolerant oxygen reduction cathodes. Journal of Power Sources *195*, 6524–6531.

Kerzenmacher, S., Schroeder, M., and Brämer, R. (2010b). Raney-platinum film electrodes for potentially implantable glucose fuel cells. Part 1: Nickel-free glucose oxidation anodes. Journal of Power Sources *195*, 6516–6523.

Khaligh, A., Zeng, P., and Zheng, C. (2010). Kinetic Energy Harvesting Using Piezoelectric and Electromagnetic Technologies—State of the Art. IEEE Transactions on Industrial Electronics *57*, 850–860.

Kim, J., Jia, H., and Wang, P. (2006). Challenges in biocatalysis for enzyme-based biofuel cells. Biotechnology Advances *24*, 296–308.

Kintz, P., Tracqui, A., Mangin, P., and Edel, Y. (1996). Sweat Testing in Opioid

Users with a Sweat Patch. Journal of Analytical Toxicology *20*, 393–397.

Klejdus, B., Petrlová, J., Potěšil, D., Adam, V., Mikelová, R., Vacek, J., Kizek, R., and Kubáň, V. (2004). Simultaneous determination of water- and fat-soluble vitamins in pharmaceutical preparations by high-performance liquid chromatography coupled with diode array detection. Analytica Chimica Acta *520*, 57–67.

Kloke, A., Biller, B., Kräling, U., Kerzenmacher, S., Zengerle, R., and Stetten, von, F. (2011). A Single Layer Glucose Fuel Cell Intended as Power Supplying Coating for Medical Implants. Fuel Cells *11*, 316–326.

Kokaislová, A., and Matějka, P. (2012). Surface-enhanced vibrational spectroscopy of B vitamins: what is the effect of SERS-active metals used? Anal Bioanal Chem *403*, 985–993.

Krabatsch, T., Schweiger, M., Stepanenko, A., and Drews, T. (2011). Improvements in implantable mechanical circulatory support systems : literature overview and update. Herz *36*, 622–629.

Krismer, A.C., Wenzel, V., Voelckel, W.G., Innerhofer, P., Stadlbauer, K.H., Haas, T., Pavlic, M., Sparr, H.J., Lindner, K.H., and Koenigsrainer, A. (2005). Employing vasopressin as an adjunct vasopressor in uncontrolled traumatic hemorrhagic shock. Anaesthesist *54*, 220–224.

Kruger, M.C., and Horrobin, D.F. (1997). Calcium metabolism, osteoporsis and

essential fatty acids: A review. Progress in Lipid Research *36*, 121–151.

Kurtz, S., Ochoa, J., Lau, E., Shkolnikov, Y., Pavri, B., Frisch, D., and Greenspon, A. (2010). Implantation Trends and Patient Profiles for Pacemakers and Implantable Cardioverter Defibrillators in the United States: 1993-2006. Pacing and Clinical Electrophysiology *33*, 705–711.

Latham, M.C. (1997). Human Nutrition in the Developing World - Michael C. Latham. Human Nutrition in the Developing World.

LeGrys, V.A., Yankaskas, J.R., and Quittell, L.M. (2007). Diagnostic Sweat Testing: The Cystic Fibrosis Foundation Guidelines. The Journal of Pedriatics 85–89.

Liu, K.-S. (1994). Preparation of fatty acid methyl esters for gas-chromatographic analysis of lipids in biological materials. J Am Oil Chem Soc *71*, 1179–1187.

Liu, S.S., Monti, J., Kargbo, H.M., Athar, M.W., and Parakh, K. (2013). Frontiers of Therapy for Patients With Heart Failure. The American Journal of Medicine *126*, 6–12.e6.

Logan, B.E., and Regan, J.M. (2006). Microbial fuel cells-challenges and applications. Environmental Science & Technology 5173–5180.

Ludwig, T.G., and Bibby, B.G. (1957). Further Observations Upon the Caries-Producing Potentialities of Various Foodstuffs. Journal of Dental Research *36*, 61–67.

Maehashi, K., Matsumoto, K., Takamura, Y., and Tamiya, E. (2009). Aptamer-Based Label-Free Immunosensors Using Carbon Nanotube Field-Effect Transistors. Electroanalysis *21*, 1285–1290.

Malhotra, B.D., and Chaubey, A. (2003). Biosensors for clinical diagnostics industry. Sensors and Actuators B: Chemical *91*, 117–127.

Mano, N., Mao, F., and Heller, A. (2003). Characteristics of a Miniature Compartment-less Glucose–O 2Biofuel Cell and Its Operation in a Living Plant. J. Am. Chem. Soc. *125*, 6588–6594.

Martinez, A.W., Phillips, S.T., Whitesides, G.M., and Carrilho, E. (2010). Diagnostics for the Developing World: Microfluidic Paper-Based Analytical Devices. Analytical Chemistry *82*, 3–10.

Mata-Granados, J.M., and Gómez, J.Q. (2009). Fully automatic method for the determination of fat soluble vitamins and vitamin D metabolites in serum. Clinica Chimica Acta *403*, 126–130.

Minteer, S.D., Liaw, B.Y., and Cooney, M.J. (2007). Enzyme-based biofuel cells. Current Opinion in Biotechnology *18*, 228–234.

Mintel (2010). Mintel Self-Diagnostics - US.

Mitcheson, P.D. (2010). Energy Harvesting for Human Wearable and Implantable Bio-Sensors. 32nd Annual International Conference of the IEEE EMBS 3432–3436.

Miura, H., Arai, S., Kakubari, Y., Sato, F., Matsuki, H., and Sato, T. (2006).

Improvement of the Transcutaneous Energy Transmission System Utilizing Ferrite Cored Coils for Artificial Hearts. IEEE Trans. Magn. *42*, 3578–3580.

Moehlenbrock, M.J., and Minteer, S.D. (2008). Extended lifetime biofuel cells. Chem. Soc. Rev. *37*, 1188–1196.

Mohan, V., Sandeep, S., Deepa, R., and Shah, B. (2007). Epidemiology of type 2 diabetes: Indian scenario. Indian Journal of Medical Research 217–230.

Mohapatra, H., and Phillips, S. (2013). Reagents and Assay Strategies for Quantifying Active Enzyme Analytes Using a Personal Glucose Meter. Chemical Communications *49*, 6134–6136.

Morales, D., Madigan, J., Cullinane, S., Chen, J., Heath, M., Oz, M., Oliver, J.A., and Landry, D.W. (1999). Reversal by Vasopressin of Intractable Hypotension in the Late Phase of Hemorrhagic Shock. Circulation *100*, 226–229.

Morgan, R.M., Patterson, M.J., and Nimmo, M.A. (2004). Acute effects of dehydration on sweat composition in men during prolonged exercise in the heat. Acta Physiol Scand *182*, 37–43.

Morris, D., Coyle, S., Wu, Y., Lau, K.T., and Wallace, G. (2009). Bio-sensing textile based patch with integrated optical detection system for sweat monitoring. Sensors and Actuators B: Chemical *139*, 231–236.

Murray, B. (2007). Hydration and physical performance. Journal of the American College of Nutrition *26*.

Murray, B., Stofan, J., and Eichner, E.R. (2003). Hyponatremia in athletes. Sports Science Exchange *16*, 1–6.

Murray, C.J., and Lopez, A.D. (1997). Mortality by cause for eight regions of the world: Global Burden of Disease Study. The Lancet *349*, 1269–1276.

Nagai, N. (2003). Existence of optimum space between electrodes on hydrogen production by water electrolysis. International Journal of Hydrogen Energy *28*, 35–41.

Nandi, P., Desai, D.P., and Lunte, S.M. (2010). Development of a PDMS-based microchip electrophoresis device for continuous online in vivo monitoring of microdialysis samples. Electrophoresis *31*, 1414–1422.

Oliveira, M.R., Fogaca, K.C., and Leandro-Merhi, V.A. (2009). Nutritional status and functional capacity of hospitalized elderly. Nutrition Journal *8*, 54.

Oncescu, V., and Erickson, D. (2011). A microfabricated low cost enzyme-free glucose fuel cell for powering low-power implantable devices. Journal of Power Sources *196*, 9169–9175.

Oncescu, V., and Erickson, D. (2013). High volumetric power density, non-enzymatic, glucose fuel cells. Sci. Rep. *3*, 1226.

Oncescu, V., O'Dell, D., and Erickson, D. (2013). Smartphone based health accessory for colorimetric detection of biomarkers in sweat and saliva. Lab on a Chip *13*, 3232–3238.

Ozdalga, E. (2012). The Smartphone in Medicine: A Review of Current and Potential Use Among Physicians and Students. Journal of Medical Internet Research *14*.

Parikh, P., Mochari, H., and Mosca, L. (2009). Clinical Utility of a Fingerstick Technology to Identify Individuals With Abnormal Blood Lipids and High-Sensitivity C-Reactive Protein Levels. American Journal of Health Promotion *23*, 279–282.

Patterson, M.J., Galloway, S.D.R., and Nimmo, M.A. (2000). Variations in Regional Sweat Composition in Normal Human Males. Experimental Physiology *85*, 869–875.

Prilutsky, S., Schechner, P., Bubis, E., and Makarov, V. (2010). Anodes for glucose fuel cells based on carbonized nanofibers with embedded carbon nanotubes. Electrochimica Acta *55*, 3694–3702.

Qi, Y., and McAlpine, M.C. (2010). Nanotechnology-enabled flexible and biocompatible energy harvesting. Energy & Environmental Science *3*, 1275–1285.

Rabaey, K., and Verstraete, W. (2005). Microbial fuel cells: novel biotechnology for energy generation. Trends in Biotechnology *23*, 291–298.

Rao, J.R., and Richter, G. (1974). Implantable bio-electrochemical power sources. Naturwissenschaften *61*, 200–206.

Rao, J.R., Richter, G.J., Sturm, Von, F., and Weidlich, E. (1976). The performance

of glucose electrodes and the characteristics of different biofuel cell constructions. Bioelectrochemistry and Bioenergetics *3*, 139–150.

Receveur, R.A.M., Lindemans, F.W., and Rooij, N.F. de (2007). Microsystem technologies for implantable applications. J. Micromech. Microeng. *17*, R50–R80.

Rengaraj, S., Kavanagh, P., and Leech, D. (2011). A comparison of redox polymer and enzyme co-immobilization on carbon electrodes to provide membrane-less glucose/O2 enzymatic fuel cells with improved power output and stability. Biosensors and Bioelectronics *30*, 294–299.

Ricci, F., Moscone, D., Tuta, C.S., Palleschi, G., Amine, A., Poscia, A., Valgimigli, F., and Messeri, D. (2005). Novel planar glucose biosensors for continuous monitoring use. Biosensors and Bioelectronics *20*, 1993–2000.

Ricotti, L., Assaf, T., Dario, P., and Menciassi, A. (2012). Wearable and implantable pancreas substitutes. J Artif Organs *16*, 9–22.

Rosner, M.H., and Kirven, J. (2006). Exercise-Associated Hyponatremia. Clinical Journal of the American Society of Nephrology *2*, 151–161.

Roundy, S., Wright, P.K., and Rabaey, J. (2003). A study of low level vibrations as a power source for wireless sensor nodes. Computer Communications *26*, 1131–1144.

Rubin, D.A., McMurray, R.G., and Harrell, J.S. (2003). Accuracy of three dry-chemistry methods for lipid profiling and risk factor classification. International

Journal Sports Nutrition and Exercise Metabolism *3*, 358–368.

Salam, M.T., Sawan, M., and Nguyen, D.K. (2010). Epileptic Seizure Onset Detection Prior To Clinical Manifestation. 32nd Annual International Conference of the IEEE EMBS 6210–6213.

Sandlin, Z.D., Shou, M., Shackman, J.G., and Kennedy, R.T. (2005). Microfluidic Electrophoresis Chip Coupled to Microdialysis for in Vivo Monitoring of Amino Acid Neurotransmitters. Analytical Chemistry *77*, 7702–7708.

Schmidt, C.L., and Skarstad, P.M. (2001). The future of lithium and lithium-ion batteries in implantable medical devices. Journal of Power Sources *97-98*, 742–746.

Schröder, U. (2012). From In Vitro to In Vivo-Biofuel Cells Are Maturing. Angew. Chem. Int. Ed. *51*, 7370–7372.

Schwaebel, T., Trapp, O., and Bunz, U.H.F. (2013). Digital photography for the analysis of fluorescence responses. Chemical Science *4*, 273–281.

Sharma, T., Hu, Y., Stoller, M., Feldman, M., and Ruoff, R.S. (2011). Mesoporous silica as a membrane for ultra-thin implantable direct glucose fuel cells. Lab on a Chip *11*, 2460–2465.

Shemesh, T., Rowley, K.G., Shephard, M., Piers, L.S., and O'Dea, K. (2006). Agreement between laboratory results and on-site pathology testing using Bayer DCA2000+ and Cholestech LDX point-of-care methods in remote Australian

Aboriginal communities. Clinica Chimica Acta *367*, 69–76.

Shen, L., Hagen, J.A., and Papautsky, I. (2012). Point-of-care colorimetric detection with a smartphone. Lab on a Chip *12*, 4240–4243.

Shephard, M., Mazzachi, B.C., and Shephard, A.K. (2007). Comparative performance of two point-of-care analysers for lipid testing. Clinical Laboratory *53*, 561–566.

Simopoulos, A.P. (1999). Essential fatty acids in health and chronic disease. The American Journal of Clinical Nutrition *70*, 560S–569S.

Stamatas, G.N., and Kollias, N. (2011). Detecting and Monitoring Nutrients on Skin Using Noninvasive Methods. In Nutrition and Skin, (New York, NY: Springer New York), pp. 195–208.

Stark, I. (2006). Invited Talk: Thermal Energy Harvesting with Thermo Life. (IEEE), pp. 19–22.

Stein, J.H., Carlsson, C.M., Papcke-Benson, K., Einerson, J.A., McBride, P.E., and Wiebe, D.A. (2002). Inaccuracy of Lipid Measurements with the Portable Cholestech L· D· X Analyzer in Patients with Hypercholesterolemia. Clinical Chemistry *2*, 284–290.

Stofan, J.R., Zachwieja, J.J., Horswill, C.A., and Murray, R. (2005). Sweat and sodium losses in NCAA football players: a precursor to heat cramps? International Journal of Sport Nutrition and Exercise Metabolism *15*, 641–652.

Szczupak, A., Halámek, J., and Halámková, L. (2012). Living battery – biofuel cells operating in vivo in clams. Energy & Environmental Science *5*, 8891–8895.

Tierney, S., Falch, B.M.H., Hjelme, D.R., and Stokke, B.T. (2009). Determination of Glucose Levels Using a Functionalized Hydrogel–Optical Fiber Biosensor: Toward Continuous Monitoring of Blood Glucose in Vivo. Analytical Chemistry *81*, 3630–3636.

TP, G., and DE, R. (1999). Death from hyponatremia as a result of acute water intoxication in an Army basic trainee. Mil Med *164*, 234–238.

Vaddiraju, S., Tomazos, I., Burgess, D.J., and Jain, F.C. (2010). Emerging synergy between nanotechnology and implantable biosensors: A review. Biosensors and Bioelectronics *25*, 1553–1565.

Van Gerwen, P., Laureyn, W., Laureys, W., Huyberechts, G., Op De Beeck, M., Baert, K., Suls, J., Sansen, W., Jacobs, P., Hermans, L., et al. (1998). Nanoscaled interdigitated electrode arrays for biochemical sensors. Sensors and Actuators B: Chemical *49*, 73–80.

Verschuren, M., Jacobs, D., Bloemberg, B., Kromhout, D., Menotti, A., Aravanis, C., Blackburn, H., Buzina, R., Dontas, A., Fidenza, F., et al. (1995). Serum Total Cholesterol and Long-term Coronary Heart Disease Mortality in Different CulturesTwenty-five—Year Follow-up of the Seven Countries Study. Journal of American Medical Association *274*, 131.

Vincent, C.A. (2000). Lithium batteries: a 50-year perspective, 1959–2009. Solid State Ionics *134*, 159–167.

Voelckel, W., Convertino, V., Lurie, K., Karlbauer, A., Schochl, H., Lindner, K.H., and Trimmel, H. (2010). Vasopressin for Hemorrhagic Shock Management: Revisiting the Potential Value in Civilian and Combat Casualty Care. The Journal of Trauma, Injury, Infection, and Critical Care *69*, S69–S74.

Wang, M., Slaney, T., Mabrouk, O., and Kennedy, R.T. (2010). Collection of nanoliter microdialysate fractions in plugs for off-line in vivo chemical monitoring with up to 2s temporal resolution. Journal of Neuroscience Methods *190*, 39–48.

Wang, Z.L. (2006). Piezoelectric Nanogenerators Based on Zinc Oxide Nanowire Arrays. Science *312*, 242–246.

Wei, X., and Liu, J. (2008). Power sources and electrical recharging strategies for implantable medical devices. Front. Energy Power Eng. China *2*, 1–13.

Wei, X.F., and Grill, W.M. (2009). Impedance characteristics of deep brain stimulation electrodes in vitroand in vivo. J. Neural Eng. *6*, 046008.

Wenzel, V., Raab, H., and Dünser, M.W. (2008). Arginine vasopressin: a promising rescue drug in the treatment of uncontrolled haemorrhagic shock. Best Practice & Research Clinical Anaesthesiology *22*, 299–316.

West, N.X., Hughes, J.A., and Addy, M. (2008). Erosion of dentine and enamel in

vitro by dietary acids: the effect of temperature, acid character, concentration and exposure time. Journal of Oral Rehabilitation *27*, 875–880.

Whitehead, S.J., Ford, C., and Gama, R. (2013). A combined laboratory and field evaluation of the Cholestech LDX and CardioChek PA point-of-care testing lipid and glucose analysers DOI: 10.1177/0004563213482890. Annals of Clinical Biochemistry.

Wyss, C.R., Brengelmann, G.L., Johnson, J.M., Rowell, L.B., and Niederberger, M. (1974). Control of skin blood flow, sweating, and heart rate: role of skin vs. core temperature. Journal of Applied Physiology *36*, 726–733.

Yang, Y., Wei, X.J., and Liu, J. (2007). Suitability of a thermoelectric power generator for implantable medical electronic devices. Journal of Physics D: Applied Physics *40*, 5790–5800.

Yoshida, S., Zhang, Q.Z., and Sakuyama, S. (2009). Metabolism of fatty acids and lipid hydroperoxides in human body monitoring with Fourier transform Infrared Spectroscopy. Lipids in Health and Disease *8*, 28–39.

Yuen, J.M., Shah, N.C., Walsh, J.T., Jr., Glucksberg, M.R., and Van Duyne, R.P. (2010). Transcutaneous Glucose Sensing by Surface-Enhanced Spatially Offset Raman Spectroscopy in a Rat Model. Analytical Chemistry *82*, 8382–8385.

Zafar Razzacki, S. (2004). Integrated microsystems for controlled drug delivery. Advanced Drug Delivery Reviews *56*, 185–198.

Zahn, J.D., Trebotich, D., and Liepmann, D. (2005). Microdialysis Microneedles for Continuous Medical Monitoring. Biomed Microdevices *7*, 59–69.

Zebda, A., Gondran, C., Le Goff, A., Holzinger, M., Cinquin, P., and Cosnier, S. (2011). Mediatorless high-power glucose biofuel cells based on compressed carbon nanotube-enzyme electrodes. Nat Comms *2*, 370–376.

Zhu, H., Isikman, S.O., Mudanyali, O., Greenbaum, A., and Ozcan, A. (2012). Optical imaging techniques for point-of-care diagnostics. Lab on a Chip *13*, 51–67.

Zimmermann, S., Fienbork, D., Stoeber, B., Flounders, A.W., and Liepmann, D. (2003). A microneedle-based glucose monitor: fabricated on a wafer-level using in-device enzyme immobilization. (IEEE), pp. 99–102.

Zuo, H., Stobaugh, J.F., Lunte, C.E., and Lunte, S.M. (1995). Continuous in vivo monitoring of amino acid neurotransmitters by microdialysis sampling with online derivatization and capillary electrophoresis separation. Analytical Chemistry *67*, 594–599.